

# A Two-Dimensional Coupled Model for Ice Shelf-Ocean Interaction

by

Ryan T. Walker

A dissertation submitted in partial fulfillment

of the requirements for the degree of

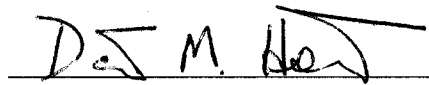
Doctor of Philosophy

Department of Mathematics

Program in Atmosphere Ocean Science

New York University

May, 2006

A handwritten signature in black ink, appearing to read "D. M. Holland", is written over a horizontal line.

David M. Holland—Advisor

UMI Number: 3222014

### INFORMATION TO USERS

The quality of this reproduction is dependent upon the quality of the copy submitted. Broken or indistinct print, colored or poor quality illustrations and photographs, print bleed-through, substandard margins, and improper alignment can adversely affect reproduction.

In the unlikely event that the author did not send a complete manuscript and there are missing pages, these will be noted. Also, if unauthorized copyright material had to be removed, a note will indicate the deletion.

**UMI<sup>®</sup>**

---

UMI Microform 3222014

Copyright 2006 by ProQuest Information and Learning Company.

All rights reserved. This microform edition is protected against unauthorized copying under Title 17, United States Code.

ProQuest Information and Learning Company  
300 North Zeeb Road  
P.O. Box 1346  
Ann Arbor, MI 48106-1346

## **Dedication**

To my family and friends, whose love and support made this possible.

## Acknowledgements

I would like to thank David Holland, who has been a steady source of good scientific and personal advice throughout this research project. His enthusiasm for science is truly contagious.

I would also like to thank Miguel Angel Morales Maqueda, without whose valuable programming tips my computer model might still be crashing.

Finally, I would like to thank Tamar Arnon and the administration of the Courant Institute, who helped me continue in the graduate program through some personally difficult times.

## Abstract

A simplified coupled model of ice shelf-ocean interaction including an evolving ice shelf is presented. This model is well suited to climate simulation, as it is computationally inexpensive and capable of handling significant changes to the shape of the sub-ice shelf cavity as the shelf profile evolves. The ocean component uses a two-dimensional vertical overturning streamfunction to describe the thermohaline circulation. In order to smoothly accommodate evolution of the shelf, the equations have been converted to a time-dependent terrain-following (sigma) vertical coordinate. The shelf component is a model for the flow of a confined ice shelf of non-uniform thickness, which consists of equations for longitudinal spreading rate and velocity. The advection of ice thickness has been modified to include separate marine and meteoric layers. The ice shelf and ocean interact thermodynamically through a three-equation formulation for basal melting and freezing.

The model is applied to Filchner Ice Shelf, Antarctica. Following a 600 year simulation, the shelf is found to have reached an equilibrium which represents a loss of approximately 10% of mass relative to its steady state when ocean interaction is not considered. Significant changes in the shelf morphology are also observed, notably an increase in basal slope near the grounding line. These changes are accompanied by shifts in the pattern of basal melting and freezing. Basal melting is found to be highly sensitive to temperature perturbations, with average melting increasing ninefold for a  $0.5^{\circ}\text{C}$  warming.

# Contents

<b>Dedication</b>	<b>ii</b>
<b>Acknowledgements</b>	<b>iii</b>
<b>Abstract</b>	<b>iv</b>
<b>List of Figures</b>	<b>ix</b>
<b>List of Tables</b>	<b>x</b>
<b>1 Background</b>	<b>1</b>
1.1 Motivation . . . . .	1
1.2 History . . . . .	3
1.2.1 Ice shelf-ocean interaction . . . . .	3
1.2.2 Tidal models . . . . .	4
1.2.3 Plume models . . . . .	4
1.2.4 Two-dimensional vertical models . . . . .	5
1.2.5 Three-dimensional models . . . . .	6
1.2.6 Coupled models . . . . .	6
1.3 Goals of this study . . . . .	7
<b>2 Model equations</b>	<b>8</b>
2.1 Ocean . . . . .	8
2.1.1 Equations in Cartesian coordinates . . . . .	8
2.1.2 Transformation to $\sigma$ -coordinates . . . . .	10
2.2 Ice shelf . . . . .	14

2.2.1	Velocity . . . . .	14
2.2.2	Advection of ice thickness . . . . .	22
2.3	Interface Thermodynamics . . . . .	23
2.4	Boundary conditions . . . . .	31
2.4.1	Vorticity equation . . . . .	31
2.4.2	Advection-diffusion equation . . . . .	32
2.4.3	Ice shelf . . . . .	35
<b>3</b>	<b>Numerical methods</b>	<b>35</b>
3.1	Ocean – Vorticity equation . . . . .	35
3.1.1	Arakawa jacobian . . . . .	35
3.1.2	Dissipation . . . . .	37
3.1.3	Density gradient . . . . .	38
3.1.4	Time differencing of the vorticity equation . . . . .	43
3.1.5	Solving for $\psi$ . . . . .	47
3.1.6	No-slip boundary condition . . . . .	48
3.2	Ocean – Tracer equation . . . . .	49
3.2.1	MPDATA . . . . .	49
3.2.2	Diffusion . . . . .	62
3.2.3	Convective adjustment . . . . .	63
3.3	Ice shelf . . . . .	64
3.3.1	Velocity . . . . .	64
3.3.2	Advection . . . . .	65
3.4	Interface . . . . .	66

<b>4 Applications</b>	<b>67</b>
4.1 Configuration . . . . .	67
4.2 Results of Control Experiment . . . . .	70
4.2.1 Initial ocean circulation . . . . .	71
4.2.2 Time evolution of the coupled system . . . . .	78
4.2.3 Final state of ice shelf . . . . .	85
4.3 Sensitivities . . . . .	89
4.3.1 Uncertainties in physical parameters . . . . .	89
4.3.2 Variation of potential temperature . . . . .	90
4.3.3 Sloping ocean floor . . . . .	92
4.3.4 Increased ice shelf velocity . . . . .	93
<b>5 Conclusions</b>	<b>103</b>
<b>References</b>	<b>107</b>



## List of Figures

1	Comparison of ice shelf drafts . . . . .	68
2	Initial ice shelf profile . . . . .	69
3	Streamfunction ( $\text{m}^2 \cdot \text{s}^{-1}$ ) after 10 years . . . . .	73
4	Horizontal velocity ( $\text{m} \cdot \text{s}^{-1}$ ) after 10 years . . . . .	74
5	Salinity (psu) after 10 years . . . . .	75
6	Potential temperature ( $^{\circ}\text{C}$ ) after 10 years . . . . .	76
7	Salinity exchange velocity ( $\text{m} \cdot \text{s}^{-1}$ ) after 10 years . . . . .	77
8	Vertical overturning streamfunction ( $\text{m}^2 \cdot \text{s}^{-1}$ ) after 600 years. . . . .	80
9	Warming of interface freezing point . . . . .	81
10	Evolution of ice shelf draft . . . . .	82
11	Evolution of melt rate . . . . .	83
12	Evolution of mixed-layer velocity . . . . .	84
13	Formation of marine ice . . . . .	86
14	Ice shelf profile at end of simulation . . . . .	87
15	Evolution of ice shelf velocity . . . . .	88
16	Variation in basal melting (after 10 years) due to temperature perturbation . . . . .	95
17	Streamfunction ( $\text{m}^2 \cdot \text{s}^{-1}$ ) after 10 years for $-0.2^{\circ}\text{C}$ temperature perturbation . . . . .	96
18	Streamfunction ( $\text{m}^2 \cdot \text{s}^{-1}$ ) after 10 years for sloping ocean floor . . . . .	97
19	Horizontal velocity ( $\text{m} \cdot \text{s}^{-1}$ ) after 10 years for sloping ocean floor . . . . .	98
20	Initial ice shelf profile for faster ice stream . . . . .	99

21	Evolution of ice shelf draft for faster ice stream . . . . .	100
22	Final ice shelf profile for faster ice stream . . . . .	101
23	Evolution of ice shelf velocity for faster ice stream . . . . .	102

## List of Tables

1	Parameters for the control experiment . . . . .	70
2	Slowing of ocean circulation . . . . .	79
3	Uncertainty in ocean circulation (after 10 years) due to variation of parameters . . . . .	89
4	Uncertainty in basal melting (after 10 years) due to variation of parameters . . . . .	90
5	Variation in ocean circulation (after 10 years) due to temperature perturbation . . . . .	91
6	Variation in basal melting (after 10 years) due to temperature perturbation . . . . .	91

# 1 Background

## 1.1 Motivation

Ice shelves, the floating extensions of glaciers which flow seaward from inland ice sheets, present questions of oceanographic, glaciological, and computational interest.

Ice shelves cover approximately 40% of the Antarctic Continental Shelf, an area of  $1.5 \times 10^6 \text{m}^2$ , effectively isolating the underlying ocean from any interaction with the atmosphere [56]. The circulation in sub-ice shelf cavities is thus markedly different from that in the open ocean, consisting largely of a thermohaline circulation forced by melting and freezing processes at the ice shelf base. This circulation is of more than local importance, since it plays a key role in the production of Antarctic Bottom Water (AABW), a driver of the global thermohaline circulation (GTHC). Sea ice formation over Antarctic coastal waters produces High Salinity Shelf Water (HSSW) through the process of brine rejection during freezing; due to its high density, HSSW sinks and enters the sub-ice shelf cavity at depth. Although this water is near the surface freezing point (approximately  $-1.9^\circ\text{C}$ ), the decrease in the freezing point of seawater with increased pressure results in HSSW being sufficiently warm to cause melting at the ice shelf base. Cooled and freshened by the incorporation of meltwater, HSSW is converted into Ice Shelf Water (ISW), which may be defined as water with potential temperature below its surface freezing point [7]. ISW exits the cavity at mid-water depths and flows downwards over the continental shelf, mixing

with Circumpolar Deep Water (CDW) to finally form AABW. The properties of AABW are thus sensitive to thermodynamic interactions between ocean and ice shelf.

Much of the glaciological interest in ice shelves has been directed towards quantifying rates of basal ablation and accretion, with an eye towards determining the ice mass balance and its sensitivity to climate change. Interest is particularly strong for regions where high basal melting may threaten the stability of ice shelves; Pine Island Glacier in the Amundsen Sea is a notable example [43]. Although the melting of ice shelves would not affect global sea level (as the shelves are already floating), the presence of ice shelves is believed to affect the flow of inland ice sheets by providing a compressive “backstress” which slows glaciers. Following the sudden collapse of the Larsen B Ice Shelf in 2002, for example, satellite-based observations indicated that glaciers flowing into the area formerly occupied by the shelf thinned rapidly and increased speed from two- to six-fold [47].

The need for numerical modeling of ice shelf-ocean interaction is particularly acute due to a lack of extensive observational data, which results from the physical inaccessibility of the areas of interest. The most readily available observations are conductivity-temperature-depth (CTD) measurements made by ships approaching ice shelf fronts during summer months; sea ice conditions tend to prevent year-round measurements even by moored instruments [56]. Furthermore, the difficulty of drilling access holes through hundreds of meters of ice makes CTD measurements inside the cavities quite sparse [56], although instru-

ments can be permanently deployed in this manner and thus gather seasonal and interannual data (*e.g.*, [35]). Airborne radio-echo sounding surveys can accurately determine the thickness profile of a shelf, and help to identify areas where marine ice has formed due to freezing at the ice shelf base [10]. Satellite-based altimetry and interferometry can also determine the thickness profile of ice shelves, while in addition measuring flow velocities [43]. However, the latter two methods provide no direct information about the sub-ice shelf circulation, leaving a significant role to be played by numerical models.

## **1.2 History**

### **1.2.1 Ice shelf-ocean interaction**

Early studies of ice shelf-ocean interaction focused on effects resulting from the pressure dependence of the freezing point of seawater. As Williams *et al.* [56] point out, 90% of ocean waters (based on salinity) have freezing points between  $-1.87$  and  $-1.92^{\circ}\text{C}$  at the surface, but at a depth of 1500 m this range becomes  $-3.01$  to  $-3.06^{\circ}\text{C}$ ; thus, even waters at the surface freezing point have the potential to melt ice at depth. Foldvik and Kvinge realized that the resulting meltwater would be “potentially supercooled” and could then, if raised, refreeze as frazil ice; they later observed this phenomenon by gathering water samples near the front of Filchner Ice Shelf [8, 9]. (Frazil ice consists of loose, randomly oriented crystals and is the first stage in the formation of both marine ice under shelves and sea ice in the open ocean.) Robin [44] discussed how ice thickness

could thus be redistributed through melting at depth and refreezing near the ice front; Lewis and Perkin [26] later referred to this mechanism as an “ice pump”. These initial studies were theoretical in nature, and did not involve numerical modeling of either ice shelf or ocean. However, Robin did suggest that, since for near-freezing waters density is primarily determined by salinity, basal melting would induce an overturning circulation driven by the positive buoyancy of the fresh meltwater.

### **1.2.2 Tidal models**

MacAyeal argued that this overturning circulation would require a supply of turbulent kinetic energy to drive vertical mixing, and proposed tides as the source of this energy [27]. In subsequent modeling studies of the Ross Ice Shelf, he showed that tides cause vertical mixing near the grounding line, which in turn drives basal melting; in addition, tides may influence the inflow of dense HSSW at the ice front [28, 29]. However, the thermohaline circulation was found to dominate the ventilation of the sub-ice shelf cavity, which has lead most recent models to focus on this circulation rather than on tidal effects.

### **1.2.3 Plume models**

Plume models are a category of reduced thermohaline models which treat meltwater as a turbulent, buoyant plume rising along the ice shelf base. In Jenkins [23], depth-integrated ordinary differential equations for conservation of mass, momentum, heat, and salt were solved along a one-dimensional contour at the

ice shelf base. Thermal driving was obtained by entraining the warmer underlying HSSW into the plume according to a velocity-dependent parameterization. Patterns of basal melting and freezing were found to depend strongly upon the shape of the ice shelf base, with the plume speed increasing in areas of steep basal slope. Jenkins and Bombosch [24] extended this model to include the formation of frazil ice, leading to increased heat and salt transfer at the ice shelf base and to more efficient conversion of supercooled water into marine ice. Recent work has focused on extension to a two-dimensional horizontal model, thus allowing Coriolis effects to be included [41].

#### **1.2.4 Two-dimensional vertical models**

Hellmer and Olbers [15] constructed a thermohaline circulation model for a two-dimensional vertical section perpendicular to the ice edge; following Robin [44], it was assumed that the circulation parallel to the ice edge was negligible. Application of the model to the Filchner Ice Shelf showed a circulation pattern similar to the predictions of plume models, with HSSW entering the cavity at depth and a thin stream of ISW ascending the ice shelf base. Further studies with this model included modification of the boundary conditions to allow channel flow, as well as application to the Ronne, Amery, Ross, and Pine Island Ice Shelves [16, 17, 18, 14]. Since the model developed in the present study is based upon this model, it will be discussed in detail in Section 2.1.1.



### 1.2.5 Three-dimensional models

The simplified models presented so far have generally omitted rotational effects, which must be investigated with a three-dimensional model. These effects were studied by Determann and Gerdes [3] and Grosfeld *et al.* [12] using primitive equation models with a terrain-following vertical coordinate in order to handle the irregularly shaped sub-ice shelf domain. Both studies found primarily barotropic flow in the cavity, which was constrained to follow contours of  $f/H$  (where  $f$  is the Coriolis parameter and  $H$  the depth of the water column). Due to the sudden change of depth at the ice front, the sub-ice shelf circulation was thus largely isolated from the open ocean, with little inflow of HSSW, resulting in weak vertical overturning and reduced melting relative to the two-dimensional Hellmer and Olbers model. Holland and Jenkins [22] adapted an isopycnic (density) coordinate model for similar studies, finding a pattern of inflow at depth and outflow along the ice shelf base which qualitatively agreed with reduced models and was not obstructed by changes in water column thickness at the ice front. A subsequent application of this model to the Ross Ice Shelf also produced active ventilation of the region near the ice front, consistent with limited observations [20]. The extent to which the sub-ice shelf cavity communicates with the open ocean thus remains an open question.

### 1.2.6 Coupled models

Recent work by Grosfeld *et al.* [11] has focused on coupling the three-dimensional general circulation model used by Determann and Gerdes [3] with a full three-

dimensional ice shelf model. The coupling follows an asynchronous approach, in which the ocean is run for several years to derive basal melting and freezing which is applied to the ice shelf on longer timescales. Formation of marine ice and shifts in basal melting patterns are consistent with the primarily barotropic flow generated by the ocean model. The scale and complexity of this model place it in a different category from the simplified process model which will be developed in this study, as we explain below.

### **1.3 Goals of this study**

Earlier models of ice shelf-ocean interaction have typically assumed the ice shelf to be in a steady state, interacting with the ocean only through thermodynamics at the interface. For present-day simulations, this is generally considered to be a reasonable assumption, since calculated melt rates suggest minimal change to the ice shelf draft during the time simulated [16]. However, the effects of basal melting and freezing over the longer timescales at which ice shelves evolve has not been extensively studied. The primary goal of this study is to consider how these processes affect the long-term mass balance of an ice shelf, including their effect upon its equilibrium shape. Investigating these questions requires simulations of both ocean and ice shelf for centuries of model time, making a computationally inexpensive reduced model an attractive option. In particular, the speed of a reduced model allows many experiments to be run in a reasonable time, so that extensive sensitivity studies become feasible. Furthermore, the physics and numerics of a reduced model can be made fairly transparent, which facilitates

analysis of physical processes and model performance. (These comments are not intended to disparage general circulation models, but only to point out that process models have different, complementary goals.) In this study, we construct a reduced process model by modifying the vertical streamfunction model of Hellmer and Olbers [15] so that it can easily be coupled with a simple model of ice shelf dynamics [40]. The new model is then applied to an idealization of the Filchner Ice Shelf, and the resulting equilibrium is studied.

## 2 Model equations

### 2.1 Ocean

#### 2.1.1 Equations in Cartesian coordinates

We begin with the standard hydrostatic, Boussinesq equations, which describe large-scale motion of an incompressible ocean:

$$\begin{aligned}
 u_t + uu_x + vv_y + ww_z - fv &= -\frac{1}{\rho_0}p_x + A_h(u_{xx} + u_{yy}) + A_v u_{zz} \\
 v_t + uv_x + vv_y + wv_z + fu &= -\frac{1}{\rho_0}p_y + A_h(v_{xx} + v_{yy}) + A_v v_{zz} \\
 0 &= -\frac{1}{\rho_0}p_z - g\rho \\
 u_x + v_y + w_z &= 0.
 \end{aligned}$$

We assume, following Robin [44] and Hellmer and Olbers [15], that the thermohaline circulation under an ice shelf is primarily two-dimensional in the  $yz$ -

plane with  $u \ll v$ . (Typically  $u \sim 10^{-2}$  m/s and  $v \sim 10^{-1}$  m/s.) Restriction to two-dimensionality forces us also to neglect Coriolis terms and  $x$ -gradients, which reduces the equations to

$$\begin{aligned} v_t + vv_y + wv_z &= -\frac{1}{\rho_0}p_y + A_h v_{yy} + A_v v_{zz} \\ 0 &= -\frac{1}{\rho_0}p_z - g\rho \\ v_y + w_z &= 0. \end{aligned}$$

We now introduce a streamfunction  $\psi$  defined by  $v = \psi_z$  and  $w = -\psi_y$ . Taking the curl of the remaining  $y$  and  $z$  momentum equations, and using the continuity equation to simplify the result, we obtain the vorticity equation:

$$\psi_{zzt} + (v\psi_{zz})_y + (w\psi_{zz})_z = \frac{g}{\rho_0}\rho_y + A_h\psi_{zzyy} + A_v\psi_{zzzz}.$$

Defining the vorticity  $\zeta$  by  $\zeta = \psi_{zz}$ , we will usually write this equation in the form

$$\zeta_t + (v\zeta)_y + (w\zeta)_z = \frac{g}{\rho_0}\rho_y + A_h\zeta_{yy} + A_v\zeta_{zz}.$$

The forcing is given by the density torque  $\frac{g}{\rho_0}\rho_y$ , which couples the momentum equations to the advection of thermodynamic tracers. The density  $\rho$  is a function of potential temperature  $\theta$ , salinity  $S$ , and pressure  $p$  given by the McDougall *et al.* equation of state [30]. (As a further simplification, we will often assume that for the relatively narrow range of seawater properties found under

ice shelves the density can be reasonably modeled by a linear equation in  $\theta$  and  $S$ .)

Tracer advection is described by the standard conservation equation

$$X_t + (vX)_y + (wX)_z = K_h X_{yy} + K_v X_{zz},$$

where  $X$  represents either  $\theta$  or  $S$ , and  $K_h$  and  $K_v$  are horizontal and vertical eddy diffusivities.

### 2.1.2 Transformation to $\sigma$ -coordinates

In order to facilitate coupling of the ocean to a one-dimensional ice shelf model, we will transform the governing equations into  $\sigma$  (terrain-following) coordinates. This will allow the ocean model to maintain a rectangular computational domain while modeling a physical domain with an irregular, time-dependent shape.

We define the new vertical coordinate by  $\sigma = \frac{z-T}{T-B}$ , where  $T$  is the depth of the ice shelf base and  $B$  is the depth of the ocean floor. It follows that  $\sigma(z = T) = 0$  at the top of the domain and  $\sigma(z = B) = -1$  at the bottom. For the coordinate transformation which follows, we assume that  $T$  is a function of time (since the ice shelf evolves during the simulation) while  $B$  is time-independent.

In the  $yz$ -plane,  $D_t = \partial_t + v\partial_y + w\partial_z$ . With  $r = y$  and  $\sigma = \frac{z-T}{T-B}$ , we have

$$\begin{aligned}
\partial_y &\rightarrow r_y \partial_r + \sigma_y \partial_\sigma + \tau_y \partial_\tau \\
&= \partial_r + \sigma_y \partial_\sigma \\
\partial_z &\rightarrow r_z \partial_r + \sigma_z \partial_\sigma + \tau_z \partial_\tau \\
&= \sigma_z \partial_\sigma \\
\partial_t &\rightarrow r_t \partial_r + \sigma_t \partial_\sigma + \tau_t \partial_\tau \\
&= \partial_\tau + \sigma_t \partial_\sigma.
\end{aligned}$$

Combining these, the material derivative is given by

$$\begin{aligned}
D_t \zeta &= \zeta_t + \sigma_t \zeta_\sigma + v(\zeta_r + \zeta_\sigma \sigma_y) + w(\zeta_\sigma \sigma_z) \\
&= \zeta_t + v\zeta_r + (\sigma_t + v\sigma_y + w\sigma_z) \zeta_\sigma \\
&= \zeta_t + v\zeta_r + \omega \zeta_\sigma.
\end{aligned}$$

Note that  $\omega = D_t \sigma$  is the “vertical” velocity on the  $(r, \sigma)$  computational grid.

Since  $v = \psi_z$  and  $w = -\psi_y$ , in the new coordinates we have  $v = \sigma_z \psi_\sigma$  and  $w = -(\psi_r + \psi_\sigma \sigma_y)$ . It follows that

$$\begin{aligned}
v\sigma_y + w\sigma_z &= \sigma_y\sigma_z\psi_\sigma - (\psi_r + \psi_\sigma\sigma_y)\sigma_z \\
&= \sigma_y\sigma_z\psi_\sigma - \psi_r\sigma_z - \sigma_y\sigma_z\psi_\sigma \\
&= -\psi_r\sigma_z
\end{aligned}$$

and then  $\omega = \sigma_t - \sigma_z\psi_r$ , which simplifies its calculation significantly.

The continuity equation  $v_y + w_z = 0$  becomes  $v_r + \sigma_y v_\sigma + \sigma_z w_\sigma = 0$ . We want to put this into flux form. From the chain rule,  $\partial_\sigma \sigma = 1 = \sigma_z z_\sigma$  and  $\partial_y z = 0 = z_r + z_\sigma \sigma_y$ , so that  $\sigma_y = -\frac{z_r}{z_\sigma}$ . Substituting this into the continuity equation and rearranging terms gives

$$\begin{aligned}
0 &= v_r - \frac{z_r}{z_\sigma} v_\sigma + \frac{1}{z_\sigma} w_\sigma \\
&= z_\sigma v_r - z_r v_\sigma + w_\sigma \\
&= (z_\sigma v)_r - (z_\sigma)_r v - z_r v_\sigma + w_\sigma \\
&= (z_\sigma v)_r + (w - z_r v)_\sigma.
\end{aligned}$$

Since  $w = D_t z = z_t + z_r v + z_\sigma \omega$ , substitution leads to

$$(z_\sigma)_t + (z_\sigma v)_r + (z_\sigma \omega)_\sigma = 0,$$

which is the flux form.

The flux form of the vorticity equation results from multiplying the flux form

of the continuity equation by  $\zeta$  and the advective form of the vorticity equation,

$$D_t \zeta = \zeta_t + v \zeta_r + \omega \zeta_\sigma = \frac{g}{\rho_0} \rho_y,$$

by  $z_\sigma$  to obtain

$$(\zeta z_\sigma)_t + (\zeta v z_\sigma)_r + (\zeta \omega z_\sigma)_\sigma = \frac{g}{\rho_0} z_\sigma \rho_y.$$

Also, the horizontal density gradient can be simplified:

$$\begin{aligned} z_\sigma \rho_y &= z_\sigma (\rho_r + \sigma_y \rho_\sigma) \\ &= z_\sigma \rho_r + z_\sigma \sigma_y \rho_\sigma \\ &= z_\sigma \rho_r - z_r \rho_\sigma \\ &= \mathcal{J}(\rho, z), \end{aligned}$$

which is called the density-jacobian form. As a further simplification, note that  $z_\sigma = T - B \equiv D$ , the total depth of the ocean.

The dissipation term has been ignored in this conversion because the model will use the dissipation term from the Princeton Ocean Model (POM) [31], which is already formulated in sigma coordinates:

$$R(\zeta) = \frac{\partial}{\partial r} \left[ D \nu_h \frac{\partial \zeta}{\partial r} \right] + \frac{\partial}{\partial \sigma} \left[ \frac{\nu_v}{D} \frac{\partial \zeta}{\partial \sigma} \right].$$

(Note that this expression has been multiplied by  $z_\sigma = D$ , so  $R(\zeta)$  is the appropriate term for equations in flux form.)



With these simplifications, we may finally write the vorticity equation as

$$(D\zeta)_t + (Dv\zeta)_r + (D\omega\zeta)_\sigma = \frac{g}{\rho_0} \mathcal{J}(\rho, z) + R(\zeta).$$

The tracer equation,  $D_t X = K_h X_{yy} + K_v X_{zz}$ , similarly becomes

$$(DX)_t + (DvX)_r + (D\omega X)_\sigma = R(X)$$

where diffusion

$$R(X) = \frac{\partial}{\partial r} \left[ D\kappa_h \frac{\partial X}{\partial r} \right] + \frac{\partial}{\partial \sigma} \left[ \frac{\kappa_v}{D} \frac{\partial X}{\partial \sigma} \right],$$

has likewise been added as in POM.

## 2.2 Ice shelf

### 2.2.1 Velocity

We will use a model proposed by Paterson [40] for one-dimensional flow of a confined ice shelf. (A confined shelf has sidewalls which exert frictional forces.)

Due to the extreme slowness of glacier flow, acceleration terms can be neglected, reducing the equations of motion to a static equilibrium between surface and body forces. The surface forces acting on a material are summarized by the stress tensor  $\tau$ , where  $\tau_{ij}$  is the force acting upon a plane normal to  $\hat{i}$  in the  $\hat{j}$  direction. When  $i \neq j$ , the component is called a shear stress; when  $i = j$ , the component is called a normal stress and is often written in the form

$\sigma_x \equiv \tau_{xx}$ . (This notation, while standard, does conflict with our notation for the ocean vertical coordinate; however, these two variables never appear together, so the meaning should be clear in context.) From this, the force acting upon a surface  $S$  with normal  $\hat{n}$  is given by  $F = -\hat{n} \cdot \tau dS$ . In order to find the net surface force on a volume enclosed by  $S$ , we apply the Gauss divergence theorem to obtain

$$F = - \int_S \hat{n} \cdot \tau dS = - \int_V \nabla \cdot \tau dV.$$

If we assume that the only external body force is gravitational, we arrive at the stress equilibrium equation

$$\nabla \cdot \bar{\tau} = -\rho \vec{g},$$

which can be written in component form as

$$\begin{aligned} \frac{\partial \sigma_x}{\partial x} + \frac{\partial \tau_{xy}}{\partial y} + \frac{\partial \tau_{xz}}{\partial z} &= 0, \\ \frac{\partial \tau_{xy}}{\partial x} + \frac{\partial \sigma_y}{\partial y} + \frac{\partial \tau_{yz}}{\partial z} &= 0, \\ \frac{\partial \tau_{xz}}{\partial x} + \frac{\partial \tau_{yz}}{\partial y} + \frac{\partial \sigma_z}{\partial z} &= -\rho g. \end{aligned}$$

In order to determine the flow of the ice shelf, we need some relation between the forces applied and the resulting velocity components. We introduce, as in

Newtonian fluid dynamics, the strain rate tensor

$$\dot{\epsilon} = \frac{1}{2} (\nabla \vec{v} + \nabla \vec{v}^T) = \frac{1}{2} \begin{pmatrix} 2\frac{\partial u}{\partial x} & \frac{\partial v}{\partial x} + \frac{\partial u}{\partial y} & \frac{\partial w}{\partial x} + \frac{\partial u}{\partial z} \\ \frac{\partial u}{\partial y} + \frac{\partial v}{\partial x} & 2\frac{\partial v}{\partial y} & \frac{\partial w}{\partial y} + \frac{\partial v}{\partial z} \\ \frac{\partial u}{\partial z} + \frac{\partial w}{\partial x} & \frac{\partial v}{\partial z} + \frac{\partial w}{\partial y} & 2\frac{\partial w}{\partial z} \end{pmatrix}.$$

It is generally assumed that the hydrostatic pressure (i.e., the mean normal stress) does not affect the stress-strain relationship. Thus it is conventional to subtract the pressure from the normal stresses and work with the stress deviators

$$\begin{aligned} s_x &= \sigma_x - \frac{1}{3}(\sigma_x + \sigma_y + \sigma_z), \\ s_y &= \sigma_y - \frac{1}{3}(\sigma_x + \sigma_y + \sigma_z), \\ s_z &= \sigma_z - \frac{1}{3}(\sigma_x + \sigma_y + \sigma_z). \end{aligned}$$

It immediately follows that  $s_x + s_y + s_z = 0$ . It is then assumed that the strain rates are proportional (though possibly nonlinearly) to the corresponding stress deviator components, i.e. that

$$\dot{\epsilon}_x = F s_x; \dot{\epsilon}_{xy} = F \tau_{xy}$$

and so forth. It also follows from this assumption and the definition of the stress deviators that  $\dot{\epsilon}_x + \dot{\epsilon}_y + \dot{\epsilon}_z = 0$ . (Note that this is equivalent to  $\frac{\partial u}{\partial x} + \frac{\partial v}{\partial y} + \frac{\partial w}{\partial z} = 0$  from the definition of strain rate; thus we have assumed that ice is incompress-

ible.) The constitutive relation is usually stated in terms of the quantities

$$\begin{aligned} 2 \|\dot{\epsilon}\|^2 &= \dot{\epsilon}_x^2 + \dot{\epsilon}_y^2 + \dot{\epsilon}_z^2 + 2 (\dot{\epsilon}_{xy}^2 + \dot{\epsilon}_{yz}^2 + \dot{\epsilon}_{zx}^2), \\ 2 \|\tau\|^2 &= s_x^2 + s_y^2 + s_z^2 + 2 (\tau_{xy}^2 + \tau_{yz}^2 + \tau_{zx}^2), \end{aligned}$$

where  $\|\dot{\epsilon}\|$  is the effective strain rate and  $\|\tau\|$  is the effective stress deviator. (Note that these quantities are the magnitudes of their respective tensors, where  $\|A\| \equiv \sqrt{\text{trace}\left(\frac{AA^T}{2}\right)}$  is a matrix norm.) The flow relation is then assumed to have the form of a power law

$$\|\dot{\epsilon}\| = A \|\tau\|^n,$$

in which  $A$  and  $n$  are to be determined empirically. It then follows from the earlier assumption of proportionality that

$$\dot{\epsilon}_x = A \|\tau\|^{n-1} s_x; \dot{\epsilon}_{xy} = A \|\tau\|^{n-1} \tau_{xy} \quad (1)$$

and so forth. For most glaciological applications, the best fit is given by  $n = 3$  and the flow relation is known as Glen's Law. Using the flow relation, we can now move from the balance of forces (the stress equilibrium equation) to an equation in terms of velocity components, and thus solve for the flow of the ice shelf.

We can now describe Paterson's model. We begin with the coordinate system. The origin is at sea level, at the grounding line and on the center-line of the

shelf. The ice thickness is  $H$  and the height of the shelf surface (above sea level) is  $h$ . For convenience in notation, we define  $s = h$  and  $b = h - H$  as the height (depth) of the surface and base of the shelf, respectively. We assume that the shelf is uniform along the transverse ( $x$ ) direction, and confined between parallel vertical sidewalls a distance  $2X$  apart. The sidewalls exert a shear stress  $\tau_{xy}$  on the shelf. (Note that the stress tensor is assumed symmetric, so  $\tau_{yx} = \tau_{xy}$ .) The flow is thus along the  $y$ -axis only.

We make three simplifying assumptions: First, the shear stress  $\tau_{xy}$ , when averaged over the length and thickness of the shelf, takes the constant value  $\tau_{xy} = \tau_0$  along the sidewalls. Usual values for  $\tau_0$  are in the range of 50 to 100 kPa. Second, we assume that the shear stress varies linearly between a maximum value of  $\tau_0$  on the sidewalls and a minimum of zero at the center-line, so that

$$\frac{\partial \tau_{xy}}{\partial x} = \frac{\tau_{xy}}{x} = \frac{\tau_0}{X}.$$

(It follows that  $\frac{\partial \tau_{xy}}{\partial y} = 0$ .) Third, we assume that the surface slope is small along  $y$  and zero along  $x$ , so that we can neglect  $\frac{\partial \tau_{yz}}{\partial y}$  and  $\tau_{xz}$ . With these simplifications, the stress equilibrium equations reduce to

$$\frac{\tau_0}{X} + \frac{\partial \sigma_y}{\partial y} + \frac{\partial \tau_{yz}}{\partial z} = 0, \quad (2)$$

$$\frac{\partial \sigma_z}{\partial z} = \rho g. \quad (3)$$

Since a free surface cannot support a tangential stress, the boundary conditions

are

$$(\sigma_z - \sigma_y)_s \frac{ds}{dy} + (\tau_{yz})_s = 0, \quad (4)$$

$$(\sigma_z - \sigma_y)_b \frac{db}{dy} + (\tau_{yz})_b = 0. \quad (5)$$

We now attempt to find the three components which remain in the stress equilibrium equations. Since the shelf is confined, it cannot expand in the  $x$  direction, so  $\dot{\epsilon}_x = 0$ . From the flow relation (1) it follows that the stress deviator component  $s_x$  is also zero, so  $s_y = -s_z = \frac{1}{2}(\sigma_y - \sigma_z)$  from the definition of the stress deviator. Also, if we vertically integrate (3) (neglecting atmospheric pressure) we find that

$$(\sigma_z)_s = 0; (\sigma_z)_b = -\rho g H.$$

We can now vertically integrate (2):

$$\int_b^s \frac{\partial \sigma_y}{\partial y} dz + (\tau_{yz})_s - (\tau_{yz})_b = -\tau_0 \frac{H}{X}.$$

The Leibniz rule for integrals gives

$$\frac{\partial}{\partial y} \int_b^s \sigma_y dz = \int_b^s \frac{\partial \sigma_y}{\partial y} dz + (\sigma_y)_s \frac{ds}{dy} - (\sigma_y)_b \frac{db}{dy}.$$

Substituting the boundary conditions (4,5) into this leads to

$$\frac{\partial}{\partial y} \int_b^s \sigma_y dz = -\tau_0 \frac{H}{X} + (\sigma_z)_s \frac{ds}{dy} - (\sigma_z)_b \frac{db}{dy},$$

and thus

$$\frac{\partial}{\partial y} \int_b^s \sigma_y dz = -\tau_0 \frac{H}{X} + \rho g H \frac{db}{dy}. \quad (6)$$

Integrating (3) vertically twice gives  $\int \sigma_z dz = -\frac{1}{2} \rho g H^2$ , so

$$\frac{\partial}{\partial y} \int_b^s \sigma_z dz = -\rho g H \frac{dH}{dy}. \quad (7)$$

Now since we have  $s_y = \frac{1}{2} (\sigma_y - \sigma_z)$ , we can subtract (6) and (7) (remembering that  $b + H = h = s$ ) to obtain

$$2 \frac{\partial}{\partial y} (H \bar{s}_y) = 2 \frac{\partial}{\partial y} \int_b^s s_y dz = -\tau_0 \frac{H}{X} + \rho g H \frac{ds}{dy},$$

where the bar indicates averaging over the ice thickness. In order to find  $H \bar{s}_y$  for any  $y$ , we integrate in  $y$  starting from the ice front, where  $y = Y$ .

$$H \bar{s}_y - (H \bar{s}_y)_Y = \frac{\rho g}{2} \int_Y^y H \frac{ds}{dy} dy - \frac{\tau_0}{2} \int_Y^y \frac{H}{X} dy.$$

We can simplify the first integral using the floating condition  $s = h = \left(1 - \frac{\rho}{\rho'}\right) H$ , where  $\rho'$  is the density of seawater. Making this substitution and integrating sim-

plifies the first term on the right to

$$\rho g \left(1 - \frac{\rho}{\rho'}\right) (H^2 - H_Y^2) / 4.$$

We can also simplify  $(H\bar{s}_y)_Y$  by considering the balance of forces at the ice front. The total horizontal force on a vertical column in the shelf must balance the total horizontal force due to hydrostatic pressure exerted upon the submerged portion of the ice front. It follows that

$$H\bar{\sigma}_y = \int_b^s \sigma_y dz = \int_b^0 \rho' g z dz = -\frac{1}{2} \rho' g (H - h)^2 = -\frac{1}{2} \rho g H (H - h),$$

where the last equality comes from the floating condition. Combining this result with the earlier results that  $\int \sigma_z dz = -\frac{1}{2} \rho g H^2$  and  $s_y = \frac{1}{2} (\sigma_y - \sigma_z)$ , we find that

$$(H\bar{s}_y)_Y = \frac{1}{4} \rho g h_Y H_Y = \frac{1}{4} \rho g \left(1 - \frac{\rho}{\rho'}\right) H_Y^2.$$

With this substitution (in addition to our earlier simplification of the right hand side), our equation finally reduces to

$$\bar{s}_y = \frac{1}{4} \rho g h - \frac{\tau_0}{2H} \int_Y^y \frac{H}{X} dy.$$

We can now return to Glen's law to find the strain rate  $\dot{\epsilon}_y$ . We have just found  $\bar{s}_y$ , and our assumption that the shelf is confined led to  $\bar{s}_z = -\bar{s}_y$  and  $\bar{s}_x = 0$ . The assumption of no transverse slope gives  $\tau_{xz} = 0$ , and we also have  $\tau_{xy} = 0$  along the center-line. Finally, it has been shown in [46] that the vertical shear is



negligible (approximately 25 mm/yr), so we have  $\tau_{zy} = 0$ . The definition of the effective stress deviator then gives

$$\|\tau\| = \sqrt{\frac{1}{2} (s_x^2 + s_y^2 + s_z^2 + 2(\tau_{xy}^2 + \tau_{yz}^2 + \tau_{zx}^2))} = \sqrt{\frac{1}{2} (s_y^2 + (-s_y)^2)} = s_y.$$

It follows from the flow relation (1) that

$$\dot{\epsilon}_y = A s_y^3.$$

Finally, since the flow is parallel to the  $y$ -axis and  $\dot{\epsilon}_y = \frac{\partial u}{\partial y}$ , we can integrate to find

$$v^I(y) = v_0^I + \int_0^y \dot{\epsilon}_y dy,$$

where  $v_0^I$  is the velocity at an arbitrary origin. For this model, since we are interested in the mass balance of the ice shelf, we will specify the ice stream velocity in order to control the input mass flux.

### 2.2.2 Advection of ice thickness

The total ice thickness is advected by the velocity field following the standard equation

$$\frac{\partial h}{\partial t} + v^I \frac{\partial h}{\partial y} = p - m,$$

where  $p$  is the precipitation rate (assumed positive) at the ice shelf surface, and  $m$  is the melt rate (negative for freezing) at the ice shelf base. Following Holland [19], the total thickness is divided into meteoric and marine ice layers. (Meteoric

ice is formed from fallen snow and thus includes all of the glacial ice input by the ice stream; marine ice is formed when seawater freezes onto the base of an ice shelf.) Following the standard assumption of no vertical shear in an ice shelf, both layers are advected at the same velocity, as determined in the preceding section. We thus have

$$\begin{aligned}\frac{\partial h_{met}}{\partial t} + v^I \frac{\partial h_{met}}{\partial y} &= p \\ \frac{\partial h_{mar}}{\partial t} + v^I \frac{\partial h_{mar}}{\partial y} &= -m.\end{aligned}$$

The only exception to the above occurs when the marine ice thickness is zero and melting is indicated; in this case, the melting is applied to the meteoric ice layer.

## 2.3 Interface Thermodynamics

The ice-ocean interface is subject to three constraints: the temperature must be at the local freezing point, and conservation of heat and salt are required in any phase change. These constraints lead to a system of three equations which may be solved for the interface temperature, salinity, and melt rate.

According to Millero [34], the freezing point of seawater is a linear function of pressure and a weakly nonlinear function of salinity. However, we will use a linearized version in order to simplify the solution of the three equation system:

$$T_B = aS_B + b + cp_B,$$

where  $T_B$ ,  $S_B$ , and  $p_B$  are the temperature, salinity, and pressure at the base of the ice shelf. The coefficients are empirical constants with the values  $a = -5.73 \times 10^{-2} \text{C/psu}$ ,  $b = 9.39 \times 10^{-2} \text{C}$ , and  $c = -7.53 \times 10^{-8} \text{C/Pa}$ .

Heat conservation at the interface requires that the (vertical) divergence of the heat flux balances the latent heat source (or sink) resulting from melting (or freezing):

$$Q_I^T - Q_M^T = Q_{latent}^T,$$

where the subscript  $I$  denotes a flux into the ice shelf and the subscript  $M$  denotes a flux upwards from the ocean mixed layer. The latent heat term is given by

$$Q_{latent}^T = -\rho_M m L_f,$$

where  $L_f = 3.34 \times 10^5 \text{J/kg}$  is the latent heat of fusion and  $\rho_M m$  is the mass of ice melted ( $m > 0$ ) or frozen ( $m < 0$ ) per unit time. Estimation of the other heat fluxes is more complicated and will be discussed below.

Salt conservation is described by a similar equation,

$$Q_I^S - Q_M^S = Q_{brine}^S,$$

where

$$Q_{brine}^S = \rho_M m (S_I - S_B)$$

is the salt flux necessary to maintain the interface salinity at  $S_B$  despite a freshwater flux of salinity  $S_I$ . Observations of marine ice indicate that brine rejection

is quite strong, resulting in salinities of 0.025 to 0.100 psu in the ice (Eicken *et al.* [6], Oerter *et al.* [37]). Since meteoric (glacial) ice is composed entirely of fresh water, we can thus take  $Q_I^S$  and  $S_I$  both to be identically zero.

In order to close the system of equations, we need to specify the remaining diffusive fluxes. We expect the fluxes to be proportional to their respective gradients, so we have

$$\begin{aligned} Q_I^T &= -\rho_I c_{pI} \kappa_I^T \left. \frac{\partial T_I}{\partial z} \right|_B \\ Q_M^T &= -\rho_M c_{pM} \kappa_M^T \left. \frac{\partial T_M}{\partial z} \right|_B \\ Q_M^S &= -\rho_M \kappa_M^S \left. \frac{\partial S_M}{\partial z} \right|_B. \end{aligned}$$

Here  $\kappa$  are diffusivities and  $c_p$  specific heat capacities. We can take  $c_p$  and  $\rho$  to be constant, so the problem is reduced to parameterizing the products of the diffusivities and gradients. We first consider the mixed layer fluxes  $Q_M^T$  and  $Q_M^S$ . ( $Q_I^T$  is a special case, since the ice shelf is solid.) In the case of a laminar boundary layer, it would be reasonable to assume that the temperature and salinity would vary linearly between the interface and mixed layer values, so we would have for example

$$Q_M^T = -\rho_M c_{pM} \kappa_M^T \frac{(T_B - T_M)}{h},$$

where  $h$  is the boundary layer thickness. Turbulence tends to enhance mixing, creating a nonlinear temperature profile and variable diffusivity. We parameterize this more complicated situation by introducing a nondimensional empirical

parameter  $Nu$ , so that

$$Q_M^T = -\rho_M c_{pM} \left( \frac{Nu \kappa_M^T}{h} \right) (T_B - T_M)$$

where the Nusselt number  $Nu$  has a value greater than one. The first bracketed quantity then has dimensions of velocity, so we define it to be the thermal exchange velocity  $\gamma_T$  and write

$$Q_M^T = -\rho_M c_{pM} \gamma_T (T_B - T_M).$$

Similarly,

$$Q_M^S = -\rho_M \gamma_S (S_B - S_M),$$

where  $\gamma_S$  is the salinity exchange velocity. Parameterizations of the exchange velocities must consider both turbulent effects in the mixed layer and diffusive effects in a thin, viscous sublayer. One such parameterization is

$$\gamma_T = \frac{u_*}{2.12 \ln \left( \frac{u_* h}{\nu} \right) + 12.5 \text{Pr}^{\frac{2}{3}} - 9}$$

and

$$\gamma_S = \frac{u_*}{2.12 \ln \left( \frac{u_* h}{\nu} \right) + 12.5 \text{Sc}^{\frac{2}{3}} - 9},$$

where the molecular Prandtl number ( $\text{Pr}$ ) is the ratio of viscosity to thermal diffusivity and the molecular Schmidt number ( $\text{Sc}$ ) is the ratio of viscosity to salinity diffusivity [21]. The kinematic viscosity of seawater is denoted by  $\nu$  and taken

as a constant. (The values used in this model are  $\text{Pr} = 13.8$ ,  $\text{Sc} = 2432$ , and  $\nu = 1.95 \times 10^{-6} \text{m}^2 \text{s}^{-1}$ .) The friction velocity  $u_*$  at the interface is defined in terms of a dimensionless drag coefficient  $c_d$  and the mixed layer velocity  $U_M$  by

$$u_*^2 = c_d U_M^2.$$

The model has the option of calculating the exchange velocities at each interface time step using the calculated ocean velocity or of taking them to be user-specified constants.

The final estimate necessary to complete the system is that of the basal temperature gradient. A full solution to this problem would require solving the heat transport equation

$$\frac{\partial T_I}{\partial t} + \vec{U}_I \cdot \nabla T_I = \kappa_I^T \nabla^2 T_I$$

over the entire shelf. While this is possible, it is outside the scope of the present simplified model, so we consider approximations. The simplest of these is to consider vertical diffusion only, and a steady state, so that

$$\frac{\partial^2 T_I}{\partial z^2} = 0.$$

The solution is then just a linear profile varying between  $T_S$  at the ice shelf surface and  $T_B$  at the base, so it follows that

$$\left. \frac{\partial T_I}{\partial z} \right|_B = \frac{(T_S - T_B)}{H_I},$$

where  $H_I$  is the ice shelf thickness. Although this was done in [15], observations suggest that actual ice shelf temperature profiles are highly nonlinear, so a more accurate approximation is desirable. If we instead assume that the ice shelf is in a steady state, but that vertical advection occurs at a velocity given by the melt rate, we obtain

$$\frac{\partial^2 T_I}{\partial z^2} + \frac{\tilde{m}}{\kappa_I^T} \frac{\partial T_I}{\partial z} = 0,$$

where  $\tilde{m} = \frac{\rho_M}{\rho_I} m$  is the melt rate, adjusted by the floating condition. Assuming exponential solutions of the form  $T_I(z) = e^{rz}$ , we arrive at the characteristic polynomial  $r^2 + \frac{\tilde{m}}{\kappa_I^T} r = 0$ , so the general solution has the form

$$T_I(z) = c_1 \exp\left(-\frac{\tilde{m}z}{\kappa_I^T}\right) + c_2.$$

With the boundary conditions  $T_I(0) = T_S$  and  $T_I(-H_I) = T_B$ , we have

$$T_I(z) = \frac{(T_S - T_B) \exp\left(\frac{-\tilde{m}z}{\kappa_I^T}\right) + T_B - T_S \exp\left(\frac{\tilde{m}H_I}{\kappa_I^T}\right)}{1 - \exp\left(\frac{\tilde{m}H_I}{\kappa_I^T}\right)}.$$

Evaluating the  $z$ -derivative at  $z = -H_I$  gives

$$\left. \frac{\partial T_I}{\partial z} \right|_B = \frac{(T_S - T_B)}{H_I} \Pi,$$

where

$$\Pi = \frac{\Upsilon}{e^\Upsilon - 1}$$

is a function of the Peclet number

$$\Upsilon = -\frac{\tilde{m}H_I}{\kappa_I^T}.$$

Note that except for the new factor of  $\Pi$ , this is identical to the solution for the diffusion-only case. Unfortunately,  $\Pi$  is undefined when  $\Upsilon = 0$  (that is, for a zero melt rate), which requires further approximation. Nøst and Foldvik [36] introduced the linearization

$$\Pi = \begin{cases} \frac{\tilde{m}H_I}{\kappa_I^T} & \text{when } \tilde{m} > 0 \\ 0 & \text{when } \tilde{m} < 0. \end{cases}$$

This linearization is used in Hellmer *et al.* [14] and in the present model. Note that since melt rate is one of the variables to be solved for, the linearization makes the problem implicit. In practice, this difficulty is avoided by allowing  $\Pi$  to depend on the melt rate calculated at the previous time step, with the assumption that the transition between melting and freezing regimes is gradual. Substituting back into earlier equation  $c_{pI}\rho_M\tilde{m}(T_B - \tilde{T}_S)$  when  $\tilde{m} > 0$  as

$$Q_I^T = \begin{cases} c_{pI}\rho_M\tilde{m}(T_B - \tilde{T}_S) & \text{when } \tilde{m} > 0 \\ 0 & \text{when } \tilde{m} < 0. \end{cases}$$



Finally, we can assemble the full three-equation formulation:

$$\begin{aligned} T_B &= aS_B + b + cp_B \\ \{c_{pI}m(T_S - T_B)\} + c_{pM}\gamma_T(T_M - T_B) &= mL_f \\ \gamma_S(S_M - S_B) &= mS_B, \end{aligned}$$

where the bracketed term appears only for the melting case. Solving for  $S_B$  (which we know must be nonnegative), we find that

$$AS_B^2 + BS_B + C = 0,$$

where

$$\begin{aligned} A &= \{ac_{pI}\gamma_S\} - ac_{pM}\gamma_T \\ B &= \{-c_{pI}\gamma_S(T_S - b - cp_B + aS_M)\} + c_{pM}\gamma_T(T_M - b - cp_B) + \gamma_X L_f \\ C &= \{c_{pI}\gamma_S S_M(T_S - b - cp_B)\} - \gamma_S L_f S_M. \end{aligned}$$

We can then solve this quadratic and back substitute to complete the solution. (The in situ temperature  $T_B$  must be converted to potential temperature  $\theta_B$  by a separate algorithm [30] before being used in the ocean interior.)

## 2.4 Boundary conditions

### 2.4.1 Vorticity equation

The model domain has one open boundary at the ice front, and three solid boundaries consisting of the ocean floor, the ice shelf base, and the vertical boundary near the grounding line. While the latter is not physically solid, it is assumed that the thin layer of heavy water at the grounding line does not communicate with the main cavity. At the solid boundaries, the condition of no normal flow is imposed by setting  $\psi \equiv 0$ , so that  $v = \frac{1}{D}\psi_\sigma = 0$  at the vertical wall and  $\omega = \sigma_t - \frac{1}{D}\psi_r = \sigma_t$  at the top and bottom of the domain. Note that at the ocean floor, this means  $\omega = 0$ , and that at the ice shelf base, the effective vertical velocity consists only of the motion of the interface itself, so there is no normal flow. A no-slip frictional boundary condition is imposed on  $v$  at the ocean floor and ice shelf base in order to reasonably simulate the bottom and top boundary layers. At the open boundary, a zero-gradient condition  $\zeta_r = 0$  is imposed on the vorticity (and thus on the streamfunction  $\psi$  as well). A related condition,  $\rho_y = 0$ , is imposed on the density in order to prevent forcing. Although these are not formally exact radiation boundary conditions, they are sufficient (in combination with the well-posed boundary conditions of the advection-diffusion equation below) to prevent any significant wave reflection at the open boundary, while still allowing free inflow and outflow.

### 2.4.2 Advection-diffusion equation

In order to solve the advection-diffusion equation

$$(Xz_\sigma)_t + (Xvz_\sigma)_r + (X\omega z_\sigma)_\sigma = \frac{\partial}{\partial r} \left[ D\kappa_h \frac{\partial X}{\partial r} \right] + \frac{\partial}{\partial \sigma} \left[ \frac{\kappa_v}{D} \frac{\partial X}{\partial \sigma} \right],$$

we require boundary values of  $X$  for the advective terms and boundary fluxes of  $X$  for the diffusive terms.

At the open (ice front) boundary, values of  $X$  are taken from an observed profile wherever inflow ( $v > 0$ ) occurs; no boundary data is required for outflow. This condition results from using an upstream-biased scheme for tracer advection; see Section 3.2.1 for details. It is assumed that no diffusion takes place through the open boundary.

At the ice shelf base, boundary values are derived from the interface thermodynamics. The diffusive fluxes are given by

$$\left. \frac{\kappa_v}{D} \frac{\partial X}{\partial \sigma} \right|_B = \gamma_X (X_B - X_M),$$

where  $X_B$  is the calculated value at the interface and  $X_M$  is the mixed layer value.

It is also important to consider the effect of meltwater advecting into the domain [25]. In previous models, where the ice shelf base was stationary, this meltwater flux could not be handled as an advective boundary condition without

creating an inconsistency in the modeled velocity field. Instead, a diffusive term

$$\frac{\partial}{\partial z} (m (S_B - S_M))$$

was added to the right hand side. If we consider forward-in-time differencing of this term, we have

$$S_M^{n+1} = S_M^n + \frac{\delta t}{\delta z} (m (S_B - S_M))$$

as the new mixed-layer salinity. Recalling that  $m$  is a velocity, we observe that  $\alpha = m\delta t/\delta z$  is the proportion of the cell now filled by meltwater. The differencing then has the form

$$S_M^{n+1} = \alpha S_B + (1 - \alpha) S_M^n,$$

which is just a weighted average of salinities, so this procedure is correct.

Unlike earlier models, the present model explicitly includes a moving ice shelf-ocean interface, so meltwater advection is handled directly rather than by a correction to the diffusive term. The situation is complicated somewhat by the horizontal advection of ice shelf thickness, which changes the ocean thickness without any thermodynamic effect. The vertical velocity at the upper boundary,  $\omega_B = \sigma_t$ , thus has thermodynamic and dynamic components, which must be handled separately. In order to avoid artificial forcing, the boundary values advected by the dynamic component must equal the mixed layer values; hence, the

ocean interior conserves salinity and potential temperature rather than salt and heat content. The thermodynamic component is just meltwater advection and thus uses the interface values  $S_B$  and  $\theta_B$ . It follows that

$$X|_{\sigma=0} = \alpha X_B + (1 - \alpha) X_M,$$

where

$$\alpha = \frac{\sigma_{melt}}{\sigma_t}$$

and

$$\sigma_{melt} = -D^{-1} \frac{\rho_I}{\rho_0} m.$$

Substituting this into the advection equation and applying forward-in-time differencing as before gives

$$X_M^{n+1} = \frac{h^n}{h^{n+1}} \left[ X_M^n + \frac{\delta t \sigma_t}{\delta \sigma} (\alpha X_B + (1 - \alpha) X_M^n) \right]$$

at the top of the ocean. In  $\sigma$ -coordinate space, the proportion of the cell filled by incoming water is  $\beta = \delta t \sigma_t / \delta \sigma$ , and we observe from this that  $h^{n+1} = (1 + \beta) h^n$ .

It then follows that

$$\begin{aligned} X^{n+1} &= \frac{1}{1 + \beta} [(1 + (1 - \alpha) \beta) X_M^n + \alpha \beta X_B] \\ &= \left( 1 - \frac{\alpha \beta}{1 + \beta} \right) X_M^n + \frac{\alpha \beta}{1 + \beta} X_B \\ &= (1 + \epsilon) X_M^n + \epsilon X_B, \end{aligned}$$

which is again a weighted average of the tracer. This method is thus equivalent to the diffusive term of earlier models, with slightly greater accuracy since the changing volume of the cell is taken into account.

It is assumed that no advection or diffusion occurs at the ocean floor or grounding line.

### 2.4.3 Ice shelf

Since the ice shelf model is one-dimensional (and the flow is unidirectional), the only boundary conditions necessary are values for the ice stream velocity  $v_0^I$  and the ice stream flux  $v_0^I H_0$ , where  $H_0$  is the assumed thickness of the shelf at the grounding line. At the ice front, ice thickness is allowed to advect freely out of the domain.

## 3 Numerical methods

### 3.1 Ocean – Vorticity equation

#### 3.1.1 Arakawa jacobian

In cartesian coordinates, the advective terms of the vorticity equation have the form  $v\zeta_y + w\zeta_z = \psi_z\zeta_y - \psi_y\zeta_z \equiv \mathcal{J}(\zeta, \psi)$ . In order to apply the well known Arakawa scheme to these terms, we need to express these terms in jacobian form for sigma coordinates:

$$\begin{aligned}
\mathcal{J}_{yz}(\zeta, \psi) &= \psi_z \zeta_y - \psi_y \zeta_z \\
&= (\psi_\sigma \sigma_z)(\zeta_r + \sigma_y \zeta_\sigma) + (-\psi_r - \psi_\sigma \sigma_y)(\zeta_\sigma \sigma_z) \\
&= \sigma_z(\zeta_r \psi_\sigma - \psi_r \zeta_\sigma) \\
&= \frac{1}{D} \mathcal{J}_{r\sigma}(\zeta, \psi).
\end{aligned}$$

(Note that  $\sigma_z = \frac{1}{D}$  is the jacobian  $\frac{\partial(r,\sigma)}{\partial(y,z)}$  of the coordinate transformation, so this is in agreement with the normal rules for transforming jacobians.)

Assuming equality of mixed partial derivatives, the jacobian can be written three ways:

$$\begin{aligned}
\mathcal{J}_1 &= \zeta_r \psi_\sigma - \zeta_\sigma \psi_r, \\
\mathcal{J}_2 &= (\psi \zeta_r)_\sigma - (\psi \zeta_\sigma)_r, \\
\mathcal{J}_3 &= (\zeta \psi_\sigma)_r - (\zeta \psi_r)_\sigma.
\end{aligned}$$

Using second-order centered differencing, there are three corresponding discretizations:

$$\begin{aligned}
\mathbb{J}_1 &= \Delta_r \zeta \Delta_\sigma \psi - \Delta_\sigma \zeta \Delta_r \psi, \\
\mathbb{J}_2 &= \Delta_\sigma (\psi \Delta_r \zeta) - \Delta_r (\psi \Delta_\sigma \zeta), \\
\mathbb{J}_3 &= \Delta_r (\zeta \Delta_\sigma \psi) - \Delta_\sigma (\zeta \Delta_r \psi),
\end{aligned}$$

where  $\Delta_r A \equiv (A_{i+1,j} - A_{i-1,j}) / 2\delta r$  and similarly for  $\Delta_\sigma$ . Arakawa [1] showed that various linear combinations of these discrete jacobians conserve mean square vorticity and energy; the combination

$$\mathbb{J}_7 = \frac{1}{3} (\mathbb{J}_1 + \mathbb{J}_2 + \mathbb{J}_3)$$

conserves both and is generally known as the Arakawa jacobian. This model uses the Arakawa jacobian, so that

$$J_{i,j} = \frac{1}{D_{i,j}} \mathbb{J}_7 (\zeta_{i,j}, \psi_{i,j})$$

is the discretization of the vorticity advection terms.

### 3.1.2 Dissipation

The POM dissipation term,

$$R(\zeta) = \frac{\partial}{\partial r} \left[ D\nu_h \frac{\partial \zeta}{\partial r} \right] + \frac{\partial}{\partial \sigma} \left[ \frac{\nu_v}{D} \frac{\partial \zeta}{\partial \sigma} \right],$$

when discretized by centered differencing on the Arakawa C-grid has the form

$$\begin{aligned} R_{i,j} = & \frac{\nu_h}{\delta r^2} [D_{i+1/2,j} (\zeta_{i+1,j} - \zeta_{i,j}) - D_{i-1/2,j} (\zeta_{i,j} - \zeta_{i-1,j})] \\ & + \frac{\nu_v}{\delta \sigma^2 D_{i,j}} [\zeta_{i,j+1} - 2\zeta_{i,j} + \zeta_{i,j-1}]. \end{aligned}$$



### 3.1.3 Density gradient

The horizontal density gradient is discretized by applying second-order centered differencing to its density-Jacobian form  $\rho_y = z_\sigma \rho_r - z_r \rho_\sigma$ . Since the density gradient is needed in the vorticity equation, and we are working on the Arakawa C-grid, the computation involves the four density points surrounding  $\zeta(i, j)$  and their (physical) depths. For brevity, we define  $\rho_1 = \rho(i-1, j-1)$ ,  $\rho_2 = \rho(i-1, j)$ ,  $\rho_3 = \rho(i, j)$ ,  $\rho_4 = \rho(i, j-1)$ , and similarly for  $z$ . Then

$$\begin{aligned} \rho_y &= z_\sigma \rho_r - z_r \rho_\sigma \\ &\approx \frac{(z_2 + z_3) - (z_1 + z_4)}{2d\sigma} \cdot \frac{(\rho_3 + \rho_4) - (\rho_2 + \rho_1)}{2dr} \\ &\quad - \frac{(\rho_2 + \rho_3) - (\rho_1 + \rho_4)}{2d\sigma} \cdot \frac{(z_3 + z_4) - (z_2 + z_1)}{2dr} \\ &= -\frac{1}{4drd\sigma} [(\rho_1 + \rho_2 - \rho_3 - \rho_4)(z_2 - z_1 + z_4 - z_3) \\ &\quad - (\rho_2 - \rho_1 + \rho_4 - \rho_3)(z_1 + z_2 - z_3 - z_4)]. \end{aligned}$$

Note that two key properties of the continuous Jacobian are retained: the discretization is antisymmetric in  $\rho$  and  $z$ , and is identically zero when  $\rho$  and  $z$  are linearly dependent. This discretization can be further simplified into the “diagonal” form

$$\rho_y \approx \frac{1}{2drd\sigma} [(z_3 - z_1)(\rho_4 - \rho_2) - (\rho_3 - \rho_1)(z_4 - z_2)]$$

due to cancellations when the preceding form is multiplied out.

The truncation error of this discretization is best evaluated by considering the horizontal derivative of a function  $b(z)$ , so that the error consists of all nonzero terms. (The following analysis expands upon Song [54].) For brevity, we define the operators

$$\begin{aligned}\delta_r b &= b_{i+1} - b_i, \\ \delta_\sigma b &= b_{j+1} - b_j, \\ \bar{b}^r &= \frac{1}{2} (b_i + b_{i+1}), \\ \bar{b}^\sigma &= \frac{1}{2} (b_j + b_{j+1}).\end{aligned}$$

In this notation, the density jacobian takes the form

$$\mathcal{J}(b, z) = \frac{1}{dr d\sigma} (\delta_\sigma \bar{z}^r \delta_r \bar{b}^\sigma - \delta_r \bar{z}^\sigma \delta_\sigma \bar{b}^r).$$

Combining Song's notation with our previous numbering of points, we have

$$\begin{aligned}\delta_r \bar{b}^\sigma &= \frac{1}{2} (b_3 + b_4 - b_1 - b_2), \\ \delta_\sigma \bar{b}^r &= \frac{1}{2} (b_2 + b_3 - b_1 - b_4),\end{aligned}$$

and similarly for  $z$ . Taylor expansion of  $b(z)$  around  $\bar{z} = \frac{1}{4} (z_1 + z_2 + z_3 + z_4)$  gives

$$b(z) = b(\bar{z}) + b_z(\bar{z})(z - \bar{z}) + \frac{1}{2} b_{zz}(\bar{z})(z - \bar{z})^2 + O[(z - \bar{z})^3],$$

which we then substitute into the discretization. We then find that

$$\begin{aligned}
\delta_r \bar{b}^\sigma &= \frac{1}{2} b_z (z_3 + z_4 - z_1 - z_2) \\
&\quad + \frac{1}{4} b_{zz} ((z_3 - \bar{z})^2 + (z_4 - \bar{z})^2 - (z_1 - \bar{z})^2 - (z_2 - \bar{z})^2) \\
&= \frac{1}{2} b_z (\delta_r \bar{z}^\sigma) + \frac{1}{8} b_{zz} ((z_3 - z_4)^2 - (z_2 - z_1)^2) \\
&= \frac{1}{2} b_z (\delta_r \bar{z}^\sigma) + \frac{1}{8} b_{zz} \delta_r [(\delta_\sigma z)^2],
\end{aligned}$$

and similarly that

$$\begin{aligned}
\delta_\sigma \bar{b}^r &= \frac{1}{2} b_z (z_3 + z_2 - z_1 - z_4) \\
&\quad + \frac{1}{4} b_{zz} ((z_3 - \bar{z})^2 + (z_2 - \bar{z})^2 - (z_1 - \bar{z})^2 - (z_4 - \bar{z})^2) \\
&= \frac{1}{2} b_z (\delta_\sigma \bar{z}^r) + \frac{1}{8} b_{zz} ((z_3 - z_2)^2 - (z_4 - z_1)^2) \\
&= \frac{1}{2} b_z (\delta_\sigma \bar{z}^r) + \frac{1}{8} b_{zz} \delta_\sigma [(\delta_r z)^2].
\end{aligned}$$

It follows that

$$\begin{aligned}
E(\mathcal{J}) &= \frac{1}{drd\sigma} (\delta_\sigma \bar{z}^r \delta_r \bar{b}^\sigma - \delta_r \bar{z}^\sigma \delta_\sigma \bar{b}^r) \\
&= \frac{1}{drd\sigma} \left( \delta_\sigma \bar{z}^r \left( \frac{1}{2} b_z (\delta_r \bar{z}^\sigma) + \frac{1}{8} b_{zz} \delta_r [(\delta_\sigma z)^2] \right) \right. \\
&\quad \left. - \delta_r \bar{z}^\sigma \left( \frac{1}{2} b_z (\delta_\sigma \bar{z}^r) + \frac{1}{8} b_{zz} \delta_\sigma [(\delta_r z)^2] \right) \right) \\
&= \frac{1}{8drd\sigma} b_{zz} (\delta_\sigma \bar{z}^r \delta_r [(\delta_\sigma z)^2] - \delta_r \bar{z}^\sigma \delta_\sigma [(\delta_r z)^2]) \\
&= \frac{1}{8drd\sigma} b_{zz} (\delta_\sigma \bar{z}^r (2\delta_\sigma \bar{z}^r \delta_r \delta_\sigma z) - \delta_r \bar{z}^\sigma (2\delta_r \bar{z}^\sigma \delta_\sigma \delta_r z)) \\
&= \frac{1}{4drd\sigma} b_{zz} \delta_{r\sigma} z [(\delta_\sigma \bar{z}^r)^2 - (\delta_r \bar{z}^\sigma)^2],
\end{aligned}$$

which is Song's result. In the simplifying case that  $\sigma = \frac{z}{H}$ , we find that

$$\begin{aligned}\delta_\sigma \bar{z}^r &= H d\sigma, \\ \delta_r \bar{z}^\sigma &= \sigma \delta_r H, \\ \frac{\delta_{r\sigma} z}{dr d\sigma} &= H_r,\end{aligned}$$

so

$$E(\mathcal{J}) = \frac{H^2}{4} \frac{\delta_r H}{dr} \frac{\partial^2 b}{\partial z^2} \left\{ d\sigma^2 - \sigma^2 \left( \frac{\delta_r H}{H} \right)^2 \right\}$$

to leading order. It is important to note that the density jacobian form of the horizontal density gradient arises from the flux form of the vorticity equation, in which all terms have been multiplied by  $\frac{\partial z}{\partial \sigma} = H$ ; thus the actual error in the horizontal density gradient is only

$$E(\rho_y) = \frac{H}{4} \frac{\delta_r H}{dr} \frac{\partial^2 b}{\partial z^2} \left\{ d\sigma^2 - \sigma^2 \left( \frac{\delta_r H}{H} \right)^2 \right\},$$

which agrees with [33]. In this model, the sigma coordinate is defined by  $\sigma = \frac{z-T}{H}$ , so we have

$$\begin{aligned}\delta_\sigma \bar{z}^r &= d\sigma H, \\ \delta_r \bar{z}^\sigma &= \sigma \delta_r H + \delta_r T, \\ \frac{\delta_{r\sigma} z}{dr d\sigma} &= H_r,\end{aligned}$$

and the error in the horizontal density gradient is

$$E(\rho_y) = \frac{H}{4} \frac{\delta_r H}{dr} \frac{\partial^2 b}{\partial z^2} \left\{ d\sigma^2 - \left( \frac{\sigma \delta_r H + \delta_r T}{H} \right)^2 \right\},$$

which is only slightly different. Haney [13] alleges that for “hydrostatically inconsistent” grids which do not satisfy

$$\left| \frac{\sigma \delta_r H}{d\sigma H} \right| < 1,$$

the scheme is nonconvergent, since for fixed  $\left| \frac{\delta_r H}{H} \right|$  the error increases as  $\left| \frac{d\sigma}{\sigma} \right| \rightarrow 0$ . Furthermore, this condition corresponds to  $\bar{z}$  lying (vertically) outside the rectangle  $(z_1, z_2, z_3, z_4)$ , and thus to extrapolation of  $\rho$  instead of interpolation. However, Mellor [33] points out that the error does decrease as  $d\sigma \rightarrow 0$  and  $dr \rightarrow 0$  (and thus  $\delta_r H \rightarrow 0$ ), so that the density jacobian is in fact convergent. The condition

$$\left| \frac{\sigma \delta_r H}{d\sigma H} \right| = 1$$

actually results in an error minimum, as can be seen from the expression for  $E(\mathcal{J})$ . Thus, parameter values which slightly violate the “hydrostatic consistency” condition will not be significantly worse than values which narrowly meet the condition; however, the problem of extrapolation makes large violations unwise [54].

It is also a common practice (as in [31]) to subtract a reference density  $\bar{\rho}(z)$  prior to calculating  $\rho_y$ . Provided that  $\bar{\rho}$  is a function of  $z$  only, this will have no

effect on the analytical result; however, it is believed that this practice reduces the truncation error.

#### 3.1.4 Time differencing of the vorticity equation

As all of the spatial differencing methods used in the vorticity equation are second order accurate, it is desirable to use a time-stepping scheme which is also at least second order. The main issue in selecting such a method for this model is that the vorticity and advection equations are coupled through the horizontal density gradient. We first consider implicit methods. Writing the vorticity equation as  $\zeta_t = F$ , where  $F$  is the total forcing, we note that any expression for  $F^{n+1}$  must involve  $\rho^{n+1}$ . However,  $\rho^{n+1}$  can only be found by solving the advection-diffusion equation twice (for  $S$  and  $\theta$ ) and then applying the equation of state, which generally is nonlinear. Furthermore, an accurate solution of the tracer advection equation requires the velocity field at time level  $n + \frac{1}{2}$ , which leaves us with a fully implicit problem even if the nonlinear vorticity advection term is dropped. Thus, even in the simplifying case of a linearized equation of state, implicit time stepping will be extremely complicated and likely prohibitively expensive. Multistage (e.g., Runge-Kutta) explicit methods present a similar problem, since  $F$  must be estimated at one or more intermediate times, and we must solve for  $\rho^{n+\alpha}$  at considerable expense at each stage in order to have even a first order accurate estimate. This problem can be avoided altogether by choosing a multistep scheme which uses only information from past time levels.

This model employs the third-order Adams-Bashforth scheme (which will

sometimes be abbreviated as AB3). Adams-Bashforth schemes are always explicit, and have the general form

$$\zeta^{n+1} = \zeta^n + dt \sum_{i=0}^{k-1} \beta_i F^{n-i},$$

where  $k$  is the order of the scheme and the  $\beta_i$  are coefficients to be determined by Taylor expansion. The error expression for AB3 thus has the form

$$E = \frac{1}{dt} [\zeta^{n+1} - \zeta^n] - \beta_0 F^n - \beta_1 F^{n-1} - \beta_2 F^{n-2},$$

and Taylor expansion at  $t = t_n$  (remembering that  $F = \zeta'$ ) gives

$$\begin{aligned} E = & (1 - \beta_0 - \beta_1 - \beta_2) F(t_n) \\ & + \left( \frac{1}{2} + \beta_1 + 2\beta_2 \right) dt F'(t_n) \\ & + \left( \frac{1}{6} - \frac{1}{2}\beta_1 - 2\beta_2 \right) dt^2 F''(t_n) \\ & + \left( \frac{1}{24} + \frac{1}{6}\beta_1 + \frac{4}{3}\beta_2 \right) dt^3 F'''(t_n). \end{aligned}$$

Third-order accuracy then requires that

$$\begin{aligned} 1 - \beta_0 - \beta_1 - \beta_2 &= 0 \\ \frac{1}{2} + \beta_1 + 2\beta_2 &= 0 \\ \frac{1}{6} - \frac{1}{2}\beta_1 - 2\beta_2 &= 0, \end{aligned}$$

which has the solution  $\beta_0 = \frac{23}{12}$ ,  $\beta_1 = -\frac{16}{12}$ ,  $\beta_2 = \frac{5}{12}$ . The third order Adams-Bashforth scheme is therefore

$$\zeta^{n+1} = \zeta^n + \frac{dt}{12} (23F^n - 16F^{n-1} + 5F^{n-2}).$$

It is generally useful in evaluating a time-stepping method to consider its performance in solving the oscillation equation

$$\frac{d\psi}{dt} = i\omega\psi,$$

where  $\psi$  is an arbitrary function, which is a simple prototype for non-dissipative wave phenomena. (The oscillation equation arises, for example, by considering the Fourier modes of the constant velocity advection equation  $\psi_t + c\psi_x = 0$ .) As the exact solution  $\psi(t) = \psi_0 e^{i\omega t}$  is known, we can analyze the performance of a numerical scheme by examining the (complex valued) numerical amplification factor

$$A = \frac{\psi^{n+1}}{\psi^n}$$

relative to the exact amplification factor

$$A_e = \frac{\psi(t_{n+1})}{\psi(t_n)} = e^{i\omega dt}.$$

We first write the numerical amplification factor as  $A = |A| e^{i\theta}$ , where  $|A| = \{\Re(A)^2 + \Im(A)^2\}^{\frac{1}{2}}$  and  $\theta = \arctan \left[ \frac{\Im(A)}{\Re(A)} \right]$ . It then follows that the relative amplification error is just  $|A|$ , while the relative phase error can be defined as



$$R = \frac{\theta}{\omega dt}.$$

Applying the AB3 method to the oscillation equation (noting that  $A$  is a constant) leads to the cubic equation

$$A^3 - \left(1 + \frac{23}{12}i\omega dt\right) A^2 + \frac{4}{3}i\omega dt A - \frac{5}{12}i\omega dt = 0.$$

Due to the presence of the parameter  $\omega dt$ , this equation does not have a useful analytic solution. Numerical solution for many values of  $\omega dt$  [5] shows that AB3 dampens the physical mode and both computational modes. In the limit of  $\omega dt \ll 1$  (i.e., for well-resolved waves), the computational modes are strongly damped and the relative amplification error of the physical mode is

$$|A|_P = 1 - \frac{3}{8}(\omega dt)^4 + O[(\omega dt)^6].$$

This slight damping ensures stability, and is a particularly desirable behavior for long-term integration of a forced system. In the same limit, the relative phase error is

$$R_P = 1 + \frac{289}{720}(\omega dt)^4 + O[(\omega dt)^6].$$

The slight acceleration produced by AB3 is a significantly smaller phase error than those produced by second-order methods.

For realistic applications, it is also desirable to consider the behavior of a

scheme for dissipative processes, which have as a prototype the friction equation

$$\frac{d\psi}{dt} = -\kappa\psi,$$

where  $\kappa$  is a nonnegative real constant. Since the exact solution is exponential decay, stable numerical solutions will have  $|A| < 1$  with  $A$  real. Analysis similar to the previous treatment of the oscillation equation shows that AB3 produces stable, non-oscillatory solutions whenever  $\kappa dt < 0.545$  [5]. Taken together, the two analyses indicate that AB3 is a reasonable choice for time-stepping of forced advection-diffusion equations such as the vorticity equation of this model.

### 3.1.5 Solving for $\psi$

In order to obtain the streamfunction  $\psi$ , we must solve  $\zeta = D^{-2}\psi_{\sigma\sigma}$  with the boundary condition that  $\psi = 0$  at the top and bottom of the ocean domain. Since only  $\sigma$  derivatives are involved, this can be done separately for each column of grid cells, noting that  $D$  is of course constant within a column (at any given time). Applying standard second-order centered differencing, we have

$$\psi_{\sigma\sigma} \approx \frac{\psi_{j+1} - 2\psi_j + \psi_{j-1}}{d\sigma^2},$$

so the problem can be written in matrix form as

$$\vec{\zeta}_i = (D_i d\sigma)^{-2} \begin{bmatrix} -2 & 1 & & & \\ & 1 & -2 & 1 & \\ & & \ddots & & \\ & & & 1 & -2 & 1 \\ & & & & 1 & -2 \end{bmatrix} \vec{\psi}_i.$$

This is a simple tridiagonal system of equations, so we apply a standard tridiagonal solver as described in [42].

### 3.1.6 No-slip boundary condition

In order to enforce the no-slip condition  $v = 0$  at the top (and bottom) of the domain, we must take an indirect approach since the Arakawa C-grid has no horizontal velocity points lying on these boundaries. We do this by setting up a boundary condition on  $\zeta$  which implies the desired boundary condition on  $v$ . Using the same second-order centered difference approximation as above, we have

$$\zeta_T = D^{-2} \psi_{\sigma\sigma}(\sigma = 0) = \frac{\psi(-\delta\sigma) - 2\psi(0) + \psi(\delta\sigma)}{d\sigma^2}$$

at the top of the domain. Recalling that  $-1 \leq \sigma \leq 0$ , we observe that  $\psi(\delta\sigma)$  is outside the domain. However,  $v = D^{-1} \psi_\sigma$  and the no-slip condition imply that  $\psi_\sigma(0) = 0$ , and since  $\psi_\sigma(0) \approx \frac{1}{2\delta\sigma} (\psi(\delta\sigma) - \psi(-\delta\sigma))$ , we find that  $\psi(\delta\sigma) \approx$

$\psi(-\delta\sigma)$ . Combined with  $\psi(0) = 0$ , this leads to

$$\zeta_T = D^{-2} \frac{2\psi(-\delta\sigma)}{\delta\sigma^2} + O(\delta\sigma)$$

as the desired boundary condition (and similarly for the bottom). Note that the boundary values of  $\zeta$  play no role in solving for  $\psi$ , so this formula is explicit. Although the approach is indirect, setting the boundary values of  $\zeta$  in this manner is sufficient to allow the dissipation operator to produce viscous boundary layers, which is the physically correct behavior.

## 3.2 Ocean – Tracer equation

### 3.2.1 MPDATA

MPDATA (multidimensional positive definite advective transport algorithm) is a numerical scheme originally designed by Smolarkiewicz [49] to handle the transport of thermodynamic tracers in atmospheric circulation models. The method has since been extended to handle advection-diffusion equations in generalized coordinates, as well as a variety of other situations [53]. MPDATA is an iterative improvement of the upstream (donor cell) scheme, from which it inherits the property of positive definiteness (more generally, sign preservation). This is a particularly desirable property when, as in this model, the advected tracers are dynamically active through their effect on the density gradient; without a positive definite scheme, spurious overshoots and undershoots in the advected variables can lead to instability [4]. Since MPDATA is somewhat complex, it

will be described in stages.

**One-dimensional constant velocity advection** In order to explain MPDATA, we begin by considering the one-dimensional advection equation

$$\frac{\partial \phi}{\partial t} = -\frac{\partial}{\partial x} (u\phi),$$

where the velocity  $u(x, t)$  may vary in space and time. The standard upstream (donor cell) method for this equation may be written as

$$\phi_i^{n+1} = \phi_i^n - \frac{\delta t}{\delta x} [F(\phi_i^n, \phi_{i+1}^n, u_{i+1/2}) - F(\phi_{i-1}^n, \phi_i^n, u_{i-1/2})],$$

where

$$F(\phi_L, \phi_R, u) = \left[ \left( \frac{u + |u|}{2} \right) \phi_L + \left( \frac{u - |u|}{2} \right) \phi_R \right]$$

defines the tracer flux through each boundary of cell  $i$ . Examination of  $F$  shows that the method is appropriately named, since regardless of the sign of  $u$  the flux always uses the value of  $\phi$  from the upstream direction.

While this behavior is physically correct, it does not result in a particularly accurate scheme. Taking second-order Taylor expansions about  $\phi_i^n$  (assuming  $u$  constant for simplicity) and substituting into the upstream formula leads to

$$\phi_t + \frac{\partial}{\partial x} (u\phi) = \frac{\partial}{\partial x} \left( |u| \frac{\delta x}{2} \phi_x \right) - \frac{\delta t}{2} \phi_{tt} + O(\delta x^2) + O(\delta t^2),$$

so the method is only first-order accurate in time and space. Using the original

equation, we observe that  $\phi_{tt} = u^2 \phi_{xx}$ , so the upstream method is a second-order approximation to the modified equation

$$\phi_t + (u\phi)_x = (K\phi_x)_x,$$

where

$$K = \frac{|u| \delta x - u^2 \delta t}{2}$$

is the numerical diffusivity.

In order to obtain a higher order method, this term must be compensated; for example, a Lax-Wendroff method would subtract a centered difference approximation. The basic idea of MPDATA schemes is to compensate using an upstream approximation of the error term. By defining

$$\tilde{u} = \begin{cases} \frac{K}{\phi} \phi_x & \text{if } \phi > 0, \\ 0 & \text{if } \phi = 0, \end{cases}$$

as an “antidiffusive” pseudovelocity, the error term takes the form of an advective flux,

$$E = \frac{\partial}{\partial x} (\tilde{u}\phi),$$

which is suitable for upstream differencing. If we denote the result of the first upstream step by  $\phi^*$ , the antidiffusive correction may be written as

$$\phi_i^{n+1} = \phi_i^* - \frac{\delta t}{\delta x} [F(\phi_i^*, \phi_{i+1}^*, \tilde{u}_{i+1/2}) - F(\phi_{i-1}^*, \phi_i^*, \tilde{u}_{i-1/2})],$$

which is just another upstream step using the antidiffusive velocity

$$\tilde{u}_{i+1/2} = \frac{|u_{i+1/2}| \delta x - u_{i+1/2}^2 \delta t}{\phi_i^* + \phi_{i+1}^* + \epsilon} \left( \frac{\phi_{i+1}^* - \phi_i^*}{\delta x} \right),$$

where  $\epsilon$  is a small positive number inserted to prevent division by zero. (Note that the factor of  $\phi^*$  in the denominator is represented by a centered value, which introduces a small nonlinearity that helps preserve positivity [49].) This process may be repeated as many times as desired to further reduce the error, although Smolarkiewicz [49] reports that beyond three corrections the improvement in the solution is negligible.

The proof of second-order accuracy for MPDATA is rather complex; see Smolarkiewicz [49] for the general case. For simplicity, we assume that  $u = c > 0$  is constant and that

$$\tilde{c}_{i+1/2} = \frac{|c| \delta x - c^2 \delta t}{2\phi_i^*} \left( \frac{\phi_{i+1}^* - \phi_i^*}{\delta x} \right) = \frac{K}{\phi_i^*} \left( \frac{\phi_{i+1}^* - \phi_i^*}{\delta x} \right)$$

is the antidiffusive velocity. Note that  $K > 0$  follows from  $c > 0$  when the Courant-Friedrichs-Levy condition  $c \frac{\delta t}{\delta x} < 1$  is satisfied; we will also assume that  $\phi_x^* > 0$  so that  $\tilde{c}$  is positive as well. Under these conditions, we have

$$\begin{aligned} \phi_i^* &= \phi_i^n - c \frac{\delta t}{\delta x} (\phi_i^n - \phi_{i-1}^n), \\ \phi_i^{n+1} &= \phi_i^* - \frac{\delta t}{\delta x} (\tilde{c}_{i+1/2} \phi_i^* - \tilde{c}_{i-1/2} \phi_{i-1}^*). \end{aligned}$$

Substituting for  $\phi^*$  and  $\tilde{c}$  leads to

$$\begin{aligned}\phi_i^{n+1} = & \phi_i^n - c \frac{\delta t}{\delta x} (\phi_i^n - \phi_{i-1}^n) \\ & - \frac{K \delta t}{\delta x^2} (\phi_{i+1}^n - 2\phi_i^n + \phi_{i-1}^n) \\ & - \frac{cK \delta t^2}{\delta x^3} (\phi_{i+1}^n - 3\phi_i^n + 3\phi_{i-1}^n - \phi_{i-2}^n).\end{aligned}$$

By taking Taylor expansions, we eventually arrive at

$$\begin{aligned}\phi_t + c\phi_x = & -\frac{\delta t}{2}\phi_{tt} + c\frac{\delta x}{2}\phi_{xx} + c\frac{\delta x^2}{6}\phi_{xxx} \\ & - K\phi_{xx} - K\frac{\delta x^2}{12}\phi_{4x} + cK\delta t\phi_{xxx}.\end{aligned}$$

Since from the original equation we have  $\phi_{tt} = c^2\phi_{xx}$ , the first two terms on the right simplify to  $+K\phi_{xx}$ , so the first-order diffusive error is cancelled and we have

$$\phi_t + c\phi_x = \left(c\frac{\delta x^2}{6} + cK\delta t\right)\phi_{xxx} - K\frac{\delta x^2}{12}\phi_{4x}$$

as the modified equation. Recalling that  $K = (c\delta x - c^2\delta t)/2$ , we finally observe that all remaining error terms are at least second order, which completes the proof.

**Two-dimensional constant velocity advection** Generalizing the upstream method to two dimensions is fairly straightforward, with the only complication resulting from cross derivative terms. With the flux function  $F$  defined as before, the



method may be written as

$$\begin{aligned}\phi_{i,j}^{n+1} = & \phi_{i,j}^n - \frac{\delta t}{\delta x} [F(\phi_{i,j}^n, \phi_{i+1,j}^n, u_{i+1/2,j}) - F(\phi_{i-1,j}^n, \phi_{i,j}^n, u_{i-1/2,j})] \\ & - \frac{\delta t}{\delta y} [F(\phi_{i,j}^n, \phi_{i,j+1}^n, v_{i,j+1/2}) - F(\phi_{i,j-1}^n, \phi_{i,j}^n, v_{i,j-1/2})].\end{aligned}$$

Taylor expansion (temporarily assuming  $u$  and  $v$  constant) leads to the modified equation

$$\phi_t + (u\phi)_x + (v\phi)_y = -\frac{\delta t}{2}\phi_{tt} + \frac{\partial}{\partial x} \left( |u| \frac{\delta x}{2} \phi_x \right) + \frac{\partial}{\partial y} \left( |v| \frac{\delta y}{2} \phi_y \right),$$

which may be written as

$$\begin{aligned}\phi_t + (u\phi)_x + (v\phi)_y = & \frac{\partial}{\partial x} \left\{ \left( \frac{|u|\delta x - u^2\delta t}{2} \right) \phi_x - \frac{uv\delta t}{2} \phi_y \right\} \\ & + \frac{\partial}{\partial y} \left\{ \left( \frac{|v|\delta y - v^2\delta t}{2} \right) \phi_y - \frac{uv\delta t}{2} \phi_x \right\},\end{aligned}$$

since  $\phi_{tt} = (u^2\phi_x + uv\phi_y)_x + (v^2\phi_y + uv\phi_x)_y$  from the original equation. As before, we have first-order errors taking the form of numerical diffusion along each coordinate axis; in addition, the cross derivative term produces diffusion along characteristics which tends to deform the solution [4]. In rewriting the error terms as antidiffusive fluxes, we have

$$\phi_t + (u\phi)_x + (v\phi)_y = (\tilde{u}\phi)_x + (\tilde{v}\phi)_y,$$

where

$$\begin{aligned}\tilde{u} &= \left( \frac{|u| \delta x - u^2 \delta t}{2} \right) \frac{1}{\phi} \frac{\partial \phi}{\partial x} - \frac{\delta t u v}{2} \frac{1}{\phi} \frac{\partial \phi}{\partial y}, \\ \tilde{v} &= \left( \frac{|v| \delta y - v^2 \delta t}{2} \right) \frac{1}{\phi} \frac{\partial \phi}{\partial y} - \frac{\delta t u v}{2} \frac{1}{\phi} \frac{\partial \phi}{\partial x}.\end{aligned}$$

Before discretizing, it is useful to rewrite the antidiffusive velocities as

$$\begin{aligned}\tilde{u} &= \left( |u| - u^2 \frac{\delta t}{\delta x} \right) A - uv \frac{\delta t}{\delta y} B, \\ \tilde{v} &= \left( |v| - v^2 \frac{\delta t}{\delta y} \right) B - uv \frac{\delta t}{\delta x} A,\end{aligned}$$

where

$$\begin{aligned}A &= \frac{\delta x}{2\phi} \frac{\partial \phi}{\partial x}, \\ B &= \frac{\delta y}{2\phi} \frac{\partial \phi}{\partial y}.\end{aligned}$$

$A$  and  $B$  are evaluated at the appropriate cell edges; for example, at the right edge of a cell

$$\begin{aligned}A_{i+1/2,j} &= \frac{\phi_{i+1,j}^* - \phi_{i,j}^*}{\phi_{i+1,j}^* + \phi_{i,j}^*}, \\ B_{i+1/2,j} &= \frac{1}{2} \frac{\phi_{i+1,j+1}^* + \phi_{i,j+1}^* - \phi_{i+1,j-1}^* - \phi_{i,j-1}^*}{\phi_{i+1,j+1}^* + \phi_{i,j+1}^* + \phi_{i+1,j-1}^* + \phi_{i,j-1}^*},\end{aligned}$$

where as before  $\phi^*$  denotes the solution from the initial upstream step. The equation for the second-order correction step is then

$$\begin{aligned}\phi_{i,j}^{n+1} = & \phi_{i,j}^* - \frac{\delta t}{\delta x} [F(\phi_{i,j}^*, \phi_{i+1,j}^*, \tilde{u}_{i+1/2,j}) - F(\phi_{i-1,j}^*, \phi_{i,j}^*, \tilde{u}_{i-1/2,j})] \\ & - \frac{\delta t}{\delta y} [F(\phi_{i,j}^*, \phi_{i,j+1}^*, \tilde{v}_{i,j+1/2}) - F(\phi_{i,j-1}^*, \phi_{i,j}^*, \tilde{v}_{i,j-1/2})],\end{aligned}$$

and the process may be iterated if desired to further reduce the magnitude of the third-order error.

**Nondivergent velocity field** If we now assume that  $u = u(x, y)$  and  $v = v(x, y)$ , the original equation leads to

$$\begin{aligned}\phi_{tt} = & (u^2\phi_x + uv\phi_y + u(u_x + v_y)\phi)_x \\ & + (v^2\phi_y + uv\phi_x + v(u_x + v_y)\phi)_y.\end{aligned}$$

A lengthier Taylor expansion of both  $\vec{v}$  and  $\phi$  leads to the same modified equation as before, except for the additional error term

$$-\frac{\delta t}{2} \left\{ \frac{\partial}{\partial x} [u(u_x + v_y)\phi] + \frac{\partial}{\partial y} [v(u_x + v_y)\phi] \right\}$$

on the right hand side. Since this term vanishes when  $u_x + v_y = 0$ , it follows that the method described above is valid (and second-order accurate) for any nondivergent, time-independent velocity field.

**Time-dependent velocity field** When  $u = u(x, y, t)$  and  $v = v(x, y, t)$ , the original equation gives

$$\begin{aligned}\phi_{tt} = & \left( u^2 \phi_x + uv \phi_y + u(u_x + v_y) \phi - u_t \phi \right)_x \\ & + \left( v^2 \phi_y + uv \phi_x + v(u_x + v_y) \phi - v_t \phi \right)_y,\end{aligned}$$

leading to the additional error term

$$\frac{\delta t}{2} \left\{ \frac{\partial}{\partial x} \left( \frac{\partial u}{\partial t} \phi \right) + \frac{\partial}{\partial y} \left( \frac{\partial v}{\partial t} \phi \right) \right\}$$

on the right hand side of the modified equation. This first-order term must be compensated in order to maintain second-order accuracy in time; however, it cannot easily be incorporated into the antidiffusive correction because it is unclear how the time derivative of the velocity should be estimated.

Fortunately, there is a fairly simple solution. If we assume that the time discretization takes the form

$$\frac{\phi^{n+1} - \phi^n}{\delta t} = - \left( u^{n+1/2} \phi^n \right)_x - \left( v^{n+1/2} \phi^n \right)_y,$$

then second-order Taylor expansion in both time and space

$$u_{i+1/2}^{n+1/2} = u_i^n + \frac{\delta t}{2} u_t + \frac{\delta x}{2} u_x + \frac{\delta t^2}{4} u_{tt} + \frac{\delta x^2}{4} u_{xx} + \frac{\delta x \delta t}{4} u_{xt}$$

leads to additional terms

$$-\frac{\delta t}{2} \left\{ \frac{\partial}{\partial x} \left( \frac{\partial u}{\partial t} \phi \right) + \frac{\partial}{\partial y} \left( \frac{\partial v}{\partial t} \phi \right) \right\} + O(\delta t^2)$$

on the right hand side of the modified equation. It follows that taking the velocity field at the  $n + 1/2$  time level is sufficient for second-order accurate solutions of the time-dependent advection equation, provided that  $\bar{v}^{n+1/2}$  is itself estimated with at least second-order accuracy [50]. In practice, this model alternates solving the coupled vorticity and advection equations, so  $\bar{v}^{n+1}$  will be available at each advective step and  $\bar{v}^{n+1/2}$  can easily be found by interpolation.

**Nonhomogeneous transport** Since the equation for tracer transport in this model is an advection-diffusion equation, it is necessary to examine how MP-DATA must be modified to accurately handle forcing terms [51]. We will consider the nonhomogeneous advection equation

$$\frac{\partial \phi}{\partial t} + \nabla \cdot (\vec{v} \phi) = R,$$

where  $R$  combines all forcing and/or source terms, assuming a discretization in time of the form

$$\frac{\phi^{n+1} - \phi^n}{\delta t} + \nabla \cdot (\bar{v}^{n+1/2} \phi^n) = R^{n+1/2}.$$

Taking a second-order Taylor expansion about  $t = n\delta t$  gives

$$\frac{\partial \phi}{\partial t} + \frac{\delta t}{2} \frac{\partial^2 \phi}{\partial t^2} + \nabla \cdot \left[ \left( \vec{v} + \frac{\delta t}{2} \frac{\partial \vec{v}}{\partial t} \right) \phi \right] = R + \frac{\delta t}{2} \frac{\partial R}{\partial t} + O(\delta t^2)$$

as the continuous equation satisfied by this discretization. Differentiating the original equation (assuming a nondivergent velocity field) shows that

$$\frac{\partial^2 \phi}{\partial t^2} = \frac{\partial R}{\partial t} + \nabla \cdot \left[ (\vec{v} \cdot \nabla \phi) \vec{v} - \frac{\partial \vec{v}}{\partial t} \phi - \vec{v} R \right],$$

so the modified equation can be rewritten as

$$\frac{\partial \phi}{\partial t} + \nabla \cdot (\vec{v} \phi) = R - \frac{\delta t}{2} \nabla \cdot [(\vec{v} \cdot \nabla \phi) \vec{v}] + \frac{\delta t}{2} \nabla \cdot (\vec{v} R) + O(\delta t^2).$$

(Note that choosing the  $n + 1/2$  time level for  $\vec{v}$  and  $R$  causes all terms involving their time derivatives to cancel.) The first, forcing-independent error term is already compensated by standard MPDATA, so the problem reduces to canceling the  $\nabla \cdot (\vec{v} R)$  term in order to obtain a second-order method. Consistent with our general approach, we compensate by subtracting an upstream approximation of this term from the right hand side, which is equivalent to advecting the auxiliary field  $\phi + 0.5\delta t R^n$  instead of  $\phi$ . If we also assume that  $R^{n+1/2} = 0.5(R^n + R^{n+1})$  to second order, this method can be written as

$$\phi^{n+1} = \text{MPDATA}(\phi^n + 0.5\delta t R^n, \vec{v}^{n+1/2}) + 0.5\delta t R^{n+1}.$$

Finally, Smolarkiewicz [53] notes that for high Reynolds number geophysical flows in which  $R$  represents the diffusion operator,  $R^n$  and  $R^{n+1}$  are essentially equal, removing the need for a predictor step.

**Generalized coordinates** We finally show how MPDATA can be applied to a generalized advection-diffusion equation

$$(G\phi)_t + \nabla \cdot (\vec{v}G\phi) = GR,$$

where  $G$  is the jacobian of the transformation from cartesian coordinates to the new system  $\{x_i\}$ , and  $\vec{v}$  denotes the velocity  $\{\dot{x}_i\}$  in the new coordinates. Note that the model's tracer equation is of this form, with  $G = D$ ,  $\vec{v} = (v, \omega)$ , and  $R = R(\phi)$ , the Mellor-Blumberg diffusion operator. Since  $D$  varies slowly with time, we must slightly modify the approach of Smolarkiewicz and Margolin [52], who assume that the jacobian is a function of the spatial variables only. We will assume a time discretization of the form

$$\frac{(G\phi)^{n+1} - (G\phi)^n}{\delta t} + \nabla \cdot (\vec{v}^{n+1/2} G^n \phi^n) = G^{n+1/2} R^{n+1/2}$$

and Taylor expand around  $t = n\delta t$ . Since we have

$$(G\phi)_{tt} = \nabla \cdot [-\vec{v}_t G\phi + \vec{v} \nabla \cdot (\vec{v} G\phi) - \vec{v} G R] + (GR)_t$$

from the original equation, we arrive at the modified equation

$$(G\phi)_t + \nabla \cdot (\vec{v}G\phi) = GR - \frac{\delta t}{2} \nabla \cdot [(\vec{v} \cdot \nabla (G\phi)) \vec{v}] + \frac{\delta t}{2} \nabla \cdot (\vec{v}GR) + O(\delta t^2),$$

where we have again assumed a nondivergent velocity field. This is identical to the modified equation for advection-diffusion in cartesian coordinates, except for the extra jacobian factor. The problem thus reduces to insuring that these jacobian factors are evaluated at the correct locations on the (Arakawa C) discrete grid; in order to be consistent with the flux form of the equation, the factor of  $G$  in the flux divergence term should be evaluated at velocity points (cell edges), and the factors of  $G$  in the time derivative and forcing terms should be evaluated at tracer points (cell centers). The  $k$ th upstream iteration then takes the form

$$\begin{aligned} \phi_{i,j}^{(k)} = & \frac{G_{i,j}^n}{G_{i,j}^{n+1}} \left\{ \phi_{i,j}^{(k-1)} \right. \\ & - \frac{1}{G_{i,j}^n} \frac{\delta t}{\delta x} \left[ F\left(\phi_{i,j}^{(k-1)}, \phi_{i+1,j}^{(k-1)}, U_{i+1/2,j}^{(k)}\right) - F\left(\phi_{i-1,j}^{(k-1)}, \phi_{i,j}^{(k-1)}, U_{i-1/2,j}^{(k)}\right) \right] \\ & \left. - \frac{1}{G_{i,j}^n} \frac{\delta t}{\delta y} \left[ F\left(\phi_{i,j}^{(k-1)}, \phi_{i,j+1}^{(k-1)}, V_{i,j+1/2}^{(k)}\right) - F\left(\phi_{i,j-1}^{(k-1)}, \phi_{i,j}^{(k-1)}, V_{i,j-1/2}^{(k)}\right) \right] \right\}, \end{aligned}$$

where  $\phi^0 \equiv \phi^n$ ,  $\phi^{kmax} \equiv \phi^{n+1}$ , and the flux function  $F$  is defined as before.

The initial velocities ( $U^1, V^1$ ) incorporate the jacobian factor, so that  $U_{i+1/2,j}^1 \equiv G_{i+1/2,j}^n u_{i+1/2,j}^{n+1/2}$ ,  $V_{i,j+1/2}^1 \equiv G_{i,j+1/2}^n v_{i,j+1/2}^{n+1/2}$ , and so forth. The pseudovelocities



are defined as before; for example, on the right edge of a cell,

$$U_{i+1/2,j}^k = \left( \left| U_{i+1/2,j}^{k-1} \right| - \frac{\left( U_{i+1/2,j}^{k-1} \right)^2}{0.5 \left( G_{i,j}^n + G_{i+1,j}^n \right)} \right) A_{i+1/2,j}^k - \frac{U_{i+1/2,j}^{k-1} \bar{V}_{i+1/2,j}^{k-1}}{\left( G_{i,j}^n + G_{i+1,j}^n \right)} B_{i+1/2,j}^k,$$

where

$$\begin{aligned} A_{i+1/2,j}^k &= \frac{\phi_{i+1,j}^{k-1} - \phi_{i,j}^{k-1}}{\phi_{i+1,j}^{k-1} + \phi_{i,j}^{k-1}}, \\ B_{i+1/2,j}^k &= \frac{\phi_{i+1,j+1}^{k-1} + \phi_{i,j+1}^{k-1} - \phi_{i+1,j-1}^{k-1} - \phi_{i,j-1}^{k-1}}{\phi_{i+1,j+1}^{k-1} + \phi_{i,j+1}^{k-1} + \phi_{i+1,j-1}^{k-1} + \phi_{i,j-1}^{k-1}}, \end{aligned}$$

and

$$\bar{V}_{i+1/2,j}^{k-1} \equiv \frac{1}{4} \left( V_{i+1,j+1/2}^{k-1} + V_{i,j+1/2}^{k-1} + V_{i+1,j-1/2}^{k-1} + V_{i,j-1/2}^{k-1} \right).$$

Finally, the forcing-dependent error term is compensated as before, leaving us with

$$\phi^{n+1} = \text{MPDATA} \left( \phi^n + 0.5\delta t R^n, \bar{v}^{n+1/2}, G \right) + 0.5\delta t R^{n+1}$$

as the method used to solve the tracer advection-diffusion equation in this model.

### 3.2.2 Diffusion

The POM diffusion term,

$$R(X) = \frac{\partial}{\partial r} \left[ D \kappa_h \frac{\partial X}{\partial r} \right] + \frac{\partial}{\partial \sigma} \left[ \frac{\kappa_v}{D} \frac{\partial X}{\partial \sigma} \right],$$

when discretized by centered differencing on the Arakawa C-grid has the form

$$R_{i,j} = \frac{\kappa_h}{\delta r^2} [D_{i+1/2,j} (X_{i+1,j} - X_{i,j}) - D_{i-1/2,j} (X_{i,j} - X_{i-1,j})] \\ + \frac{\kappa_v}{\delta \sigma^2 D_{i,j}} [X_{i,j+1} - 2X_{i,j} + X_{i,j-1}].$$

### 3.2.3 Convective adjustment

Hydrostatic ocean models require some parameterization of vertical convection in order to remove static instabilities from the water column. (Static instability occurs whenever dense water lies above lighter water.) Convective adjustment schemes search for these instabilities and remove them by mixing vertically adjacent grid boxes. While this is theoretically very simple, an efficient algorithm is required to remove all instabilities with a minimum number of passes through the water column (and thus a minimum number of potentially expensive evaluations of the equation of state). Early convective adjustment schemes such as Cox [2], which mixed only two unstable adjacent levels at a time, fell short of this goal by requiring many iterations to even approximate complete mixing.

This model uses an algorithm due to Rahmstorf, which is also used by the Modular Ocean Model (MOM) [39]. While the logical structure of the Rahmstorf algorithm is more complicated than that of earlier iterative methods, it achieves complete adjustment efficiently by mixing multiple unstable levels in one pass without unnecessarily recalculating densities in the stable part of the water column. The algorithm can be summarized as follows:

1. Compute the density of each box in the water column. (Adjacent boxes

must be referenced to the same pressure in order to correctly determine static stability.)

2. Compare all adjacent pairs of boxes to find instabilities.
3. Mix the uppermost unstable pair. (If no unstable pair exists, the algorithm ends.)
4. If the box below is less dense than the mixture, incorporate it into the mixture as well. Repeat until no longer true.
5. It is possible that the box above the new mixed region is now unstable. If it is, incorporate it into the mixture and go to (3). Otherwise, search downwards from the bottom of the mixed region until an unstable pair is found, and then go to (3). (If the bottom of the ocean is reached without finding an unstable pair, the algorithm ends.)

It is important to note that mixing two grid boxes is carried out by averaging their salinities and temperatures, and then calculating the density of the mixture; densities are never mixed directly.

### **3.3 Ice shelf**

#### **3.3.1 Velocity**

The velocity of the ice shelf is given by

$$v^I(y) = v_0^I + \int_0^y \dot{\epsilon}_y dy,$$

where

$$\dot{\epsilon}_y = A\bar{s}_y^3$$

and

$$\bar{s}_y = \frac{1}{4}\rho gh - \frac{\tau_0}{2H} \int_Y^y \frac{H}{X} dy.$$

In order to match the Arakawa C-grid used for the ocean, the ice shelf variables are staggered so that velocity points are aligned with ocean  $v$  points and thickness points are aligned with ocean tracer points. Since this is a one-dimensional array, both integrals (for  $\bar{s}_y$  and  $v^I$ ) are evaluated by straightforward trapezoidal integration. Note that this is a time-independent “steady-state” calculation, which is updated on a fairly long (user-specified) timescale.

### 3.3.2 Advection

The advection of meteoric and marine ice thicknesses is given by

$$\begin{aligned} \frac{\partial h_{met}}{\partial t} + v^I \frac{\partial h_{met}}{\partial y} &= p, \\ \frac{\partial h_{mar}}{\partial t} + v^I \frac{\partial h_{mar}}{\partial y} &= -m. \end{aligned}$$

Ice thickness is updated at each ocean timestep in order to smoothly apply changes to the ocean depth resulting from basal melting and/or freezing. Since these equations are just one-dimensional tracer advection, they can be solved by

the upstream method (with source terms  $p\delta t$ ,  $-m\delta t$  added); the extremely slow ice shelf velocity ( $O(1 \text{ km/a})$ ) and short timestep ( $O(1 \text{ hr})$ ) make higher order methods unnecessary.

### 3.4 Interface

As previously described, the fairly involved formulation of the interface thermodynamics reduces to solving a quadratic equation. Due to the ill-conditioning of the standard quadratic formula, we use an approach described by [42].

Solutions to the quadratic equation  $ax^2 + bx + c = 0$  are given by the familiar quadratic formula

$$x = \frac{-b \pm \sqrt{b^2 - 4ac}}{2a}$$

and also by the less-known formula

$$x = \frac{2c}{-b \pm \sqrt{b^2 - 4ac}}.$$

In either case, when  $a$  or  $c$  is small,  $\sqrt{b^2 - 4ac} \approx b$ , so that one root involves subtraction of nearly identical terms and thus is potentially inaccurate. If instead we set

$$q = -\frac{1}{2} \left[ b + \text{sgn}(b) \sqrt{b^2 - 4ac} \right],$$

then  $x_1 = q/a$  and  $x_2 = c/q$  are the two roots. This method is algebraically equivalent to the usual formula, but avoids subtraction of nearly identical terms and is thus stable.

## 4 Applications

### 4.1 Configuration

The standard configuration of the model is based upon the idealized Filchner Ice Shelf domain of Hellmer and Olbers [15]. In that study, the ice shelf base had a constant slope of 1/1000, with a draft of 330 m at the ice front, increasing to 930 m across the 600 km length of the domain. Because the present model simulates a flowing ice shelf, however, this profile is less than ideal for our purposes. While we will run the model until the ice shelf reaches equilibrium, any initial condition which could not have been produced by the shelf component may take centuries to advect out of the domain, delaying equilibrium and obscuring the effect of ocean thermodynamics. We instead will use an equilibrium state of the ice shelf component which is reasonably close to the linear profile of the original model. (As the ice shelf component is one-dimensional, it can be run to equilibrium in less than twenty seconds of computer time when there is no interaction with the ocean component.) We find that an ice stream velocity of  $u_0 = 0.5$  km/yr and thickness of  $H_0 = 1060$  m produce a reasonable initial state when a sidewall stress of  $\tau_0 = 90$  kPa is assumed (Figure 1). Since marine ice is by definition formed only by interaction with the ocean, the shelf is initially assumed to consist entirely of meteoric ice. The initial ice shelf profile is shown in Figure 2; the shelf is light blue, the ocean a darker blue, the sea floor brown, and the sky black.

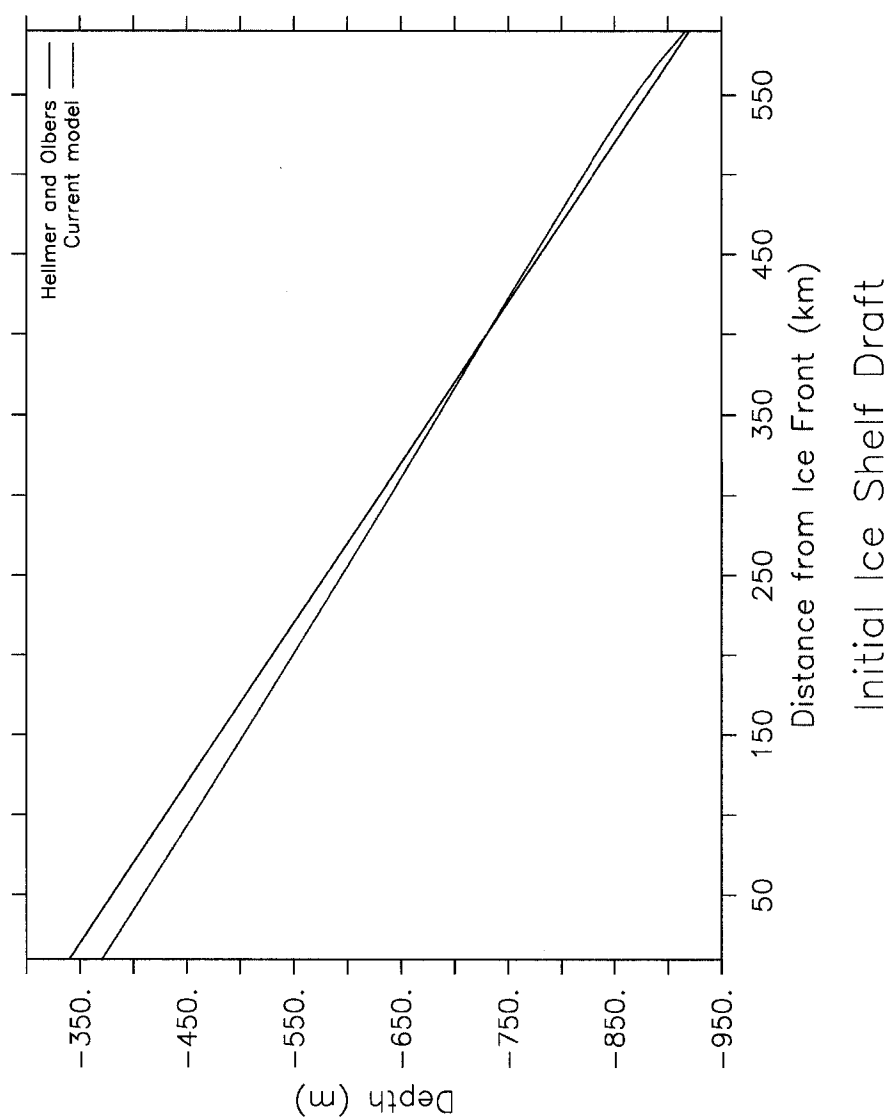
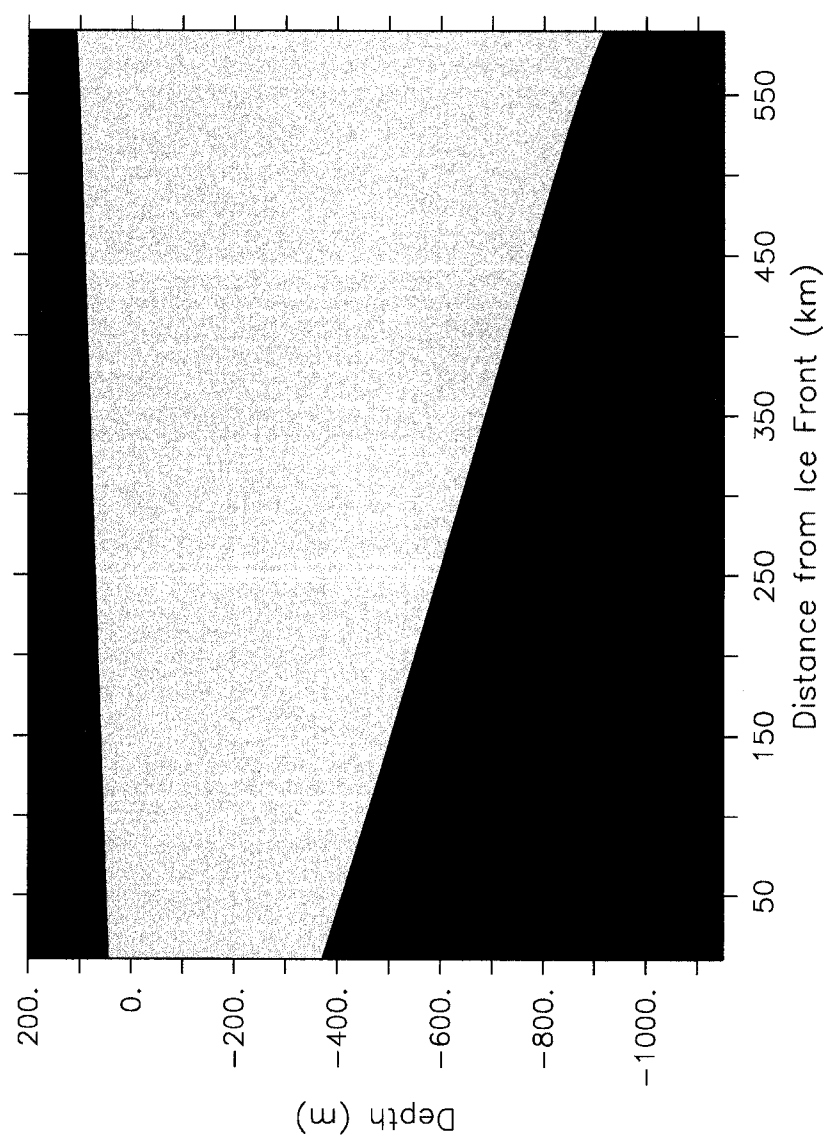


Figure 1: Comparison of ice shelf drafts



Ice Shelf Profile

Figure 2: Initial ice shelf profile



Symbol	Name	Value	Units
$\delta t$	time step	1800	s
$\delta r$	horizontal grid spacing	20	km
$\delta \sigma$	vertical grid spacing	0.05	none
$\nu_h$	horizontal viscosity	1000	$\text{m}^2\text{s}^{-1}$
$\nu_v$	vertical viscosity	$2 \times 10^{-3}$	$\text{m}^2\text{s}^{-1}$
$\kappa_h$	horizontal diffusivity	10	$\text{m}^2\text{s}^{-1}$
$\kappa_v$	vertical diffusivity	$1 \times 10^{-4}$	$\text{m}^2\text{s}^{-1}$
$u_0$	ice stream velocity	0.5	$\text{km} \cdot \text{yr}^{-1}$
$H_0$	ice stream thickness	1060	m
$\tau_0$	ice shelf sidewall stress	90	kPa
$a$	precipitation rate	10	$\text{cm} \cdot \text{yr}^{-1}$

Table 1: Parameters for the control experiment

The bathymetry is a flat ocean floor at a depth of 1100 m. The ocean is forced by salinity and temperature restoring at the open (ice front) boundary, using CTD data from Station 292 interpolated onto the  $\sigma$ -levels [45]. (In order to maintain accuracy as the depth of the ice front changes, the restoring data is re-interpolated on the ice shelf timescale of one year.) Exchange velocities are calculated dynamically from the velocity of the uppermost layer of the ocean. Model parameters for this experiment are summarized in Table 1.

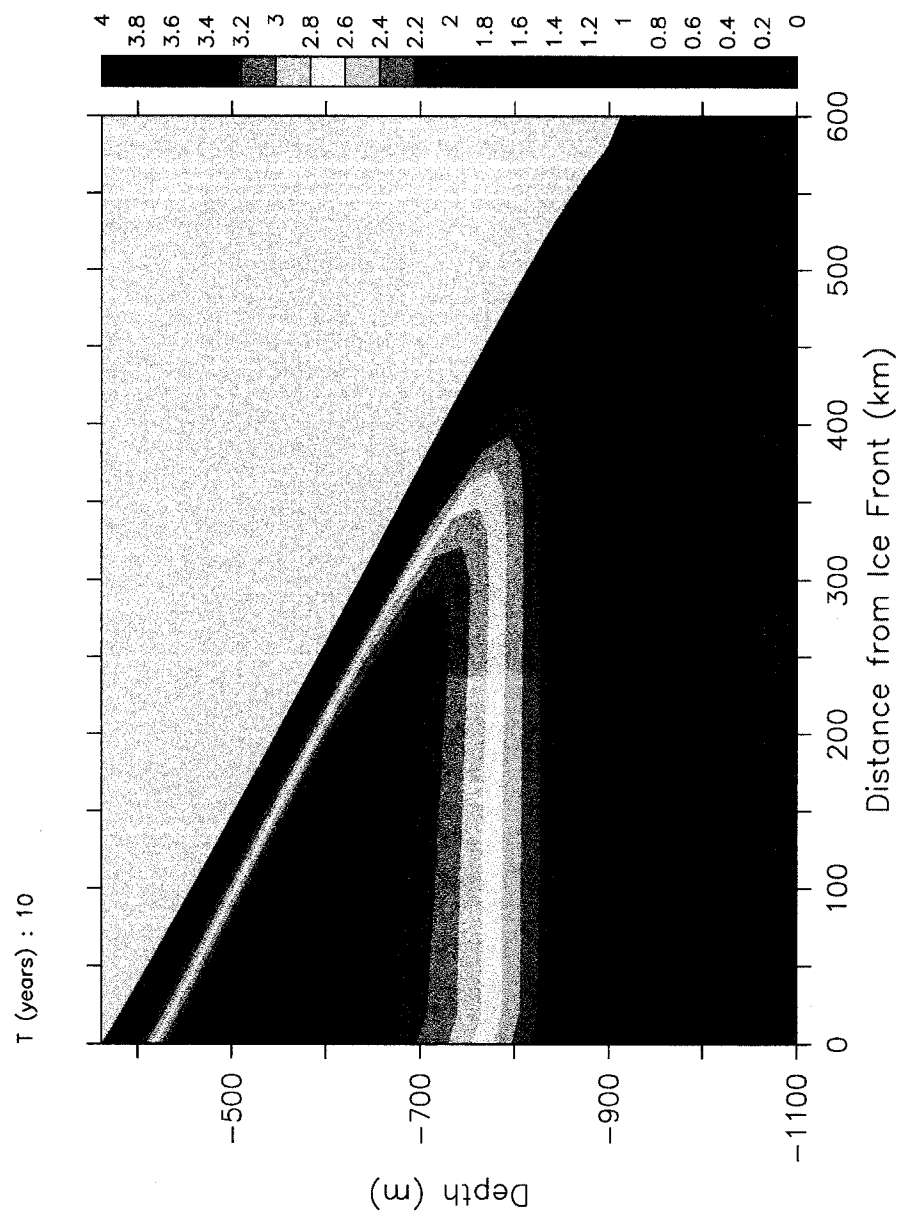
## 4.2 Results of Control Experiment

The model is run until the ice shelf reaches a steady state. For the control experiment, this occurs when the total ice shelf mass has been found to change by less than 0.5% between model years 500 and 600, with thickness changing by no more than 0.82% at any point during that time.

#### 4.2.1 Initial ocean circulation

As in the earlier Hellmer and Olbers model, the ocean reaches an essentially steady state after less than 10 years of integration. (The ice shelf thickness changes by less than 1% during this short period, so the effect of coupling is negligible.) The circulation consists primarily of a large gyre (counterclockwise in the figures) in which HSSW enters near the bottom of the cavity and a plume of ISW exits the cavity at a depth of approximately 500 m (Figure 3). This plume reaches a peak speed of nearly 7 cm/s, while the remainder of the circulation is much slower (Figure 4; note that negative velocities are directed out of the cavity). The meltwater signature is apparent in both salinity and potential temperature plots (Figures 5 and 6). In particular, while the incoming HSSW has potential temperature  $-1.94^{\circ}\text{C}$ , the plume has potential temperatures as low as  $-2.23^{\circ}\text{C}$ ; temperatures as low as  $-2.36^{\circ}\text{C}$  occur inside the cavity. In contrast with the earlier model, the peak melt rate of 0.96 m/yr occurs 530 km from the ice front (70 km from the grounding line); Hellmer and Olbers reported a peak melt rate of 1.5 m/yr near the grounding line [15]. This difference is primarily due to the use of velocity-dependent turbulent exchange velocities in this model. Over most of the domain, the calculated salinity exchange velocity is much higher than the relatively low constant value of  $5.05 \times 10^{-7} \text{ m/s}$  used in the earlier model; however, near the grounding line, where the circulation is slow, it falls below this constant (Figure 7; note that the thermal exchange velocity has the same pattern). Since the melt rate is directly proportional to the salinity exchange velocity, the result is decreased melting near the grounding line. Near

the ice front, where conditions favor marine ice formation, the higher salinity exchange velocity results in strongly increased freezing rates (a maximum of 0.29 m/yr, versus a maximum of 0.1 m/yr in [15]).



### Streamfunction

Figure 3: Streamfunction ( $\text{m}^2 \cdot \text{s}^{-1}$ ) after 10 years

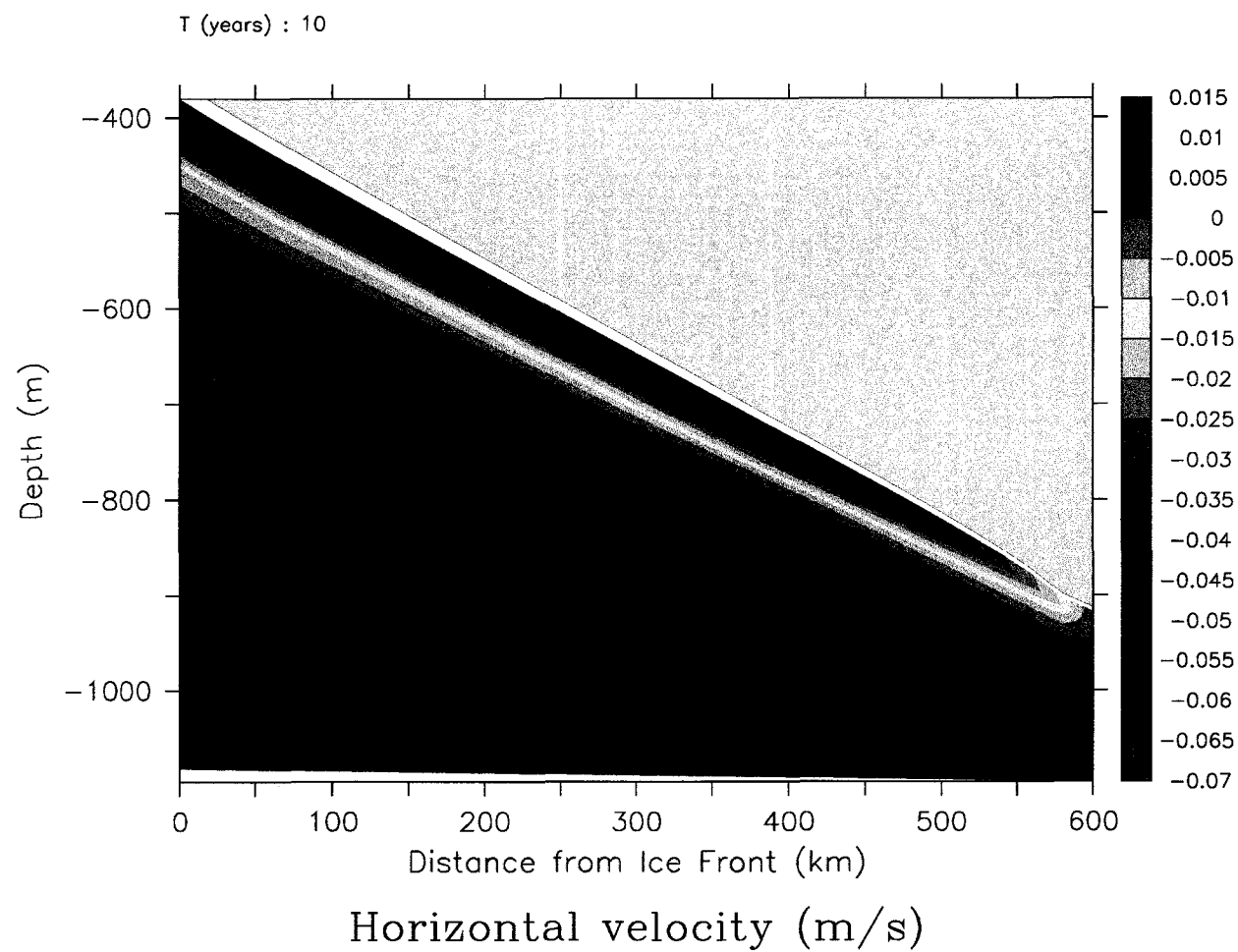
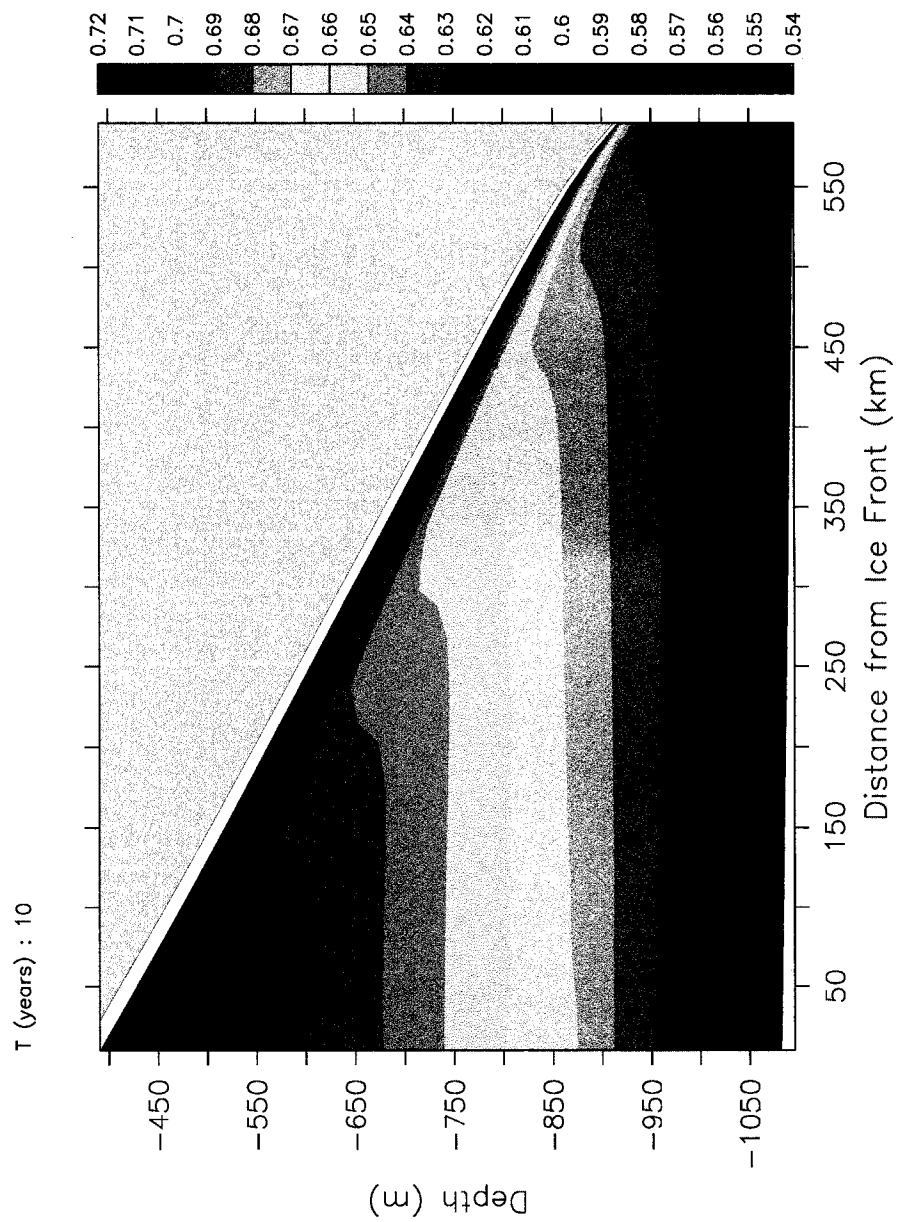
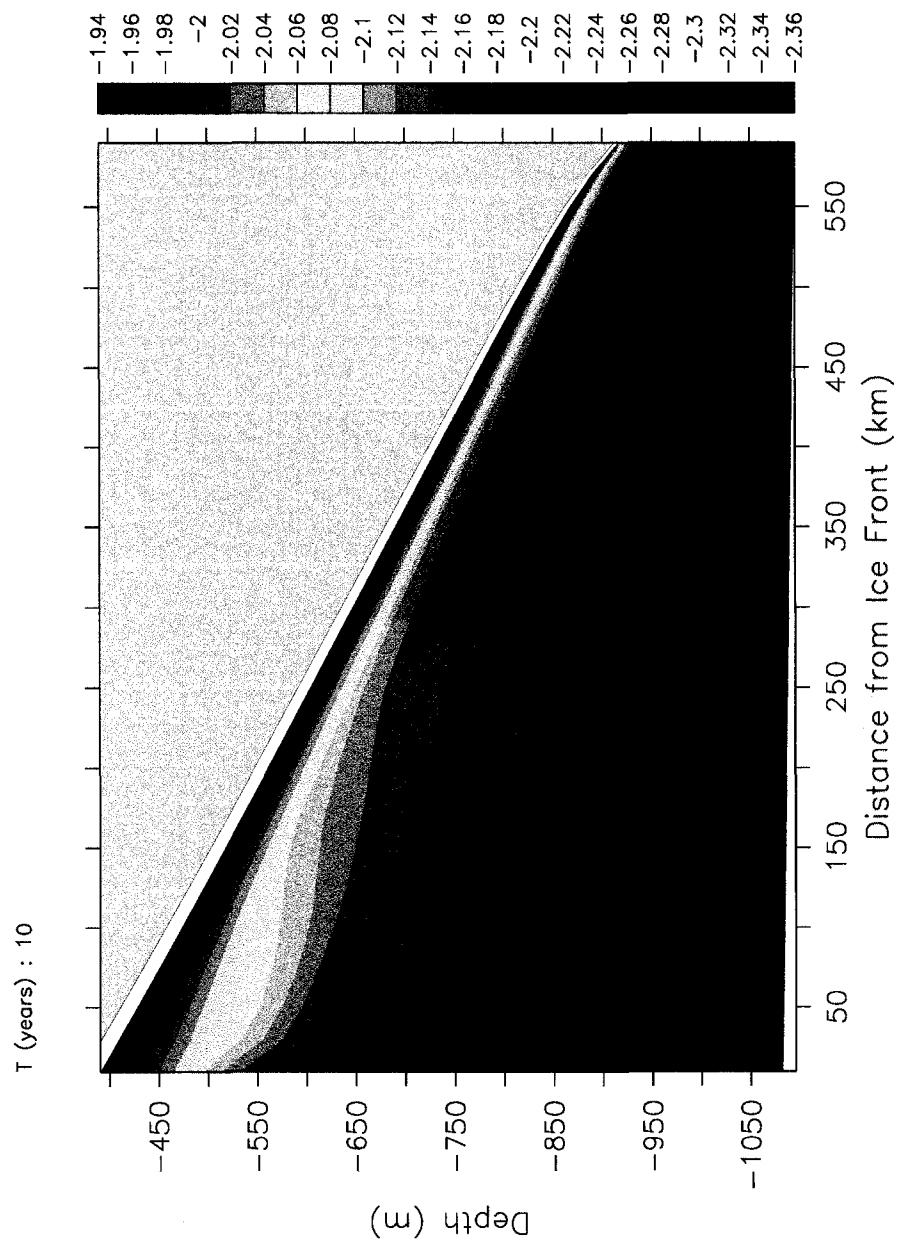


Figure 4: Horizontal velocity ( $\text{m} \cdot \text{s}^{-1}$ ) after 10 years



Salinity – 34.0 psu

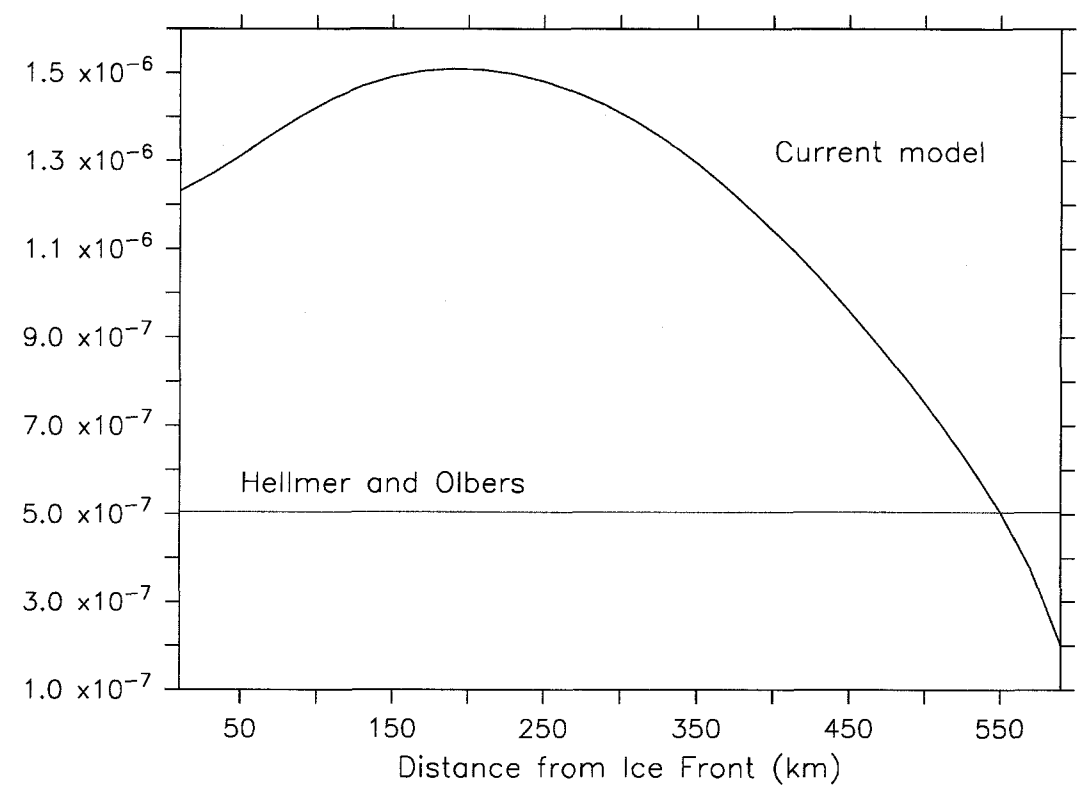
Figure 5: Salinity (psu) after 10 years



## Potential Temperature

Figure 6: Potential temperature (°C) after 10 years

77



Salinity Exchange Velocity

Figure 7: Salinity exchange velocity (m · s<sup>-1</sup>) after 10 years



#### 4.2.2 Time evolution of the coupled system

Due to the coupling with the ice shelf, the initial steady state ocean circulation slowly evolves as the cavity shape responds to melting and freezing processes. The overall pattern of the circulation changes very little throughout the simulation (Figure 8); the main effect is a mild decrease in its intensity (Table 2) as the combined effects of meltwater and reduced depth result in a warmer freezing point at the shelf base (Figure 9), lessening the thermodynamical forcing. The base of the shelf shallows and flattens throughout most of the domain, but steepens considerably near the grounding line (Figure 10). The most significant effect of this change in shape is a shift in the pattern of basal melting (Figure 11). Since the ISW plume is gravitationally driven by the density gradient, a steeper basal slope allows meltwater to rise more rapidly, as seen in Figure 12. The increased ocean velocity beneath the steepest sections of the shelf leads to increased melting in these areas, which further increases the basal slope in a positive feedback which persists until finally balanced by horizontal advection of ice thickness. This agrees with earlier studies, which found that increasing the basal slope of the shelf near the grounding line led to locally increased melt rate and plume velocity, but had little effect on the overall ocean circulation [17, 23]. The transition from melting to freezing occurs 140 km from the ice front throughout the entire simulation; however, the magnitude of the melt rate varies considerably. Between kilometers 150 and 530, melting decreases with time, falling by as much as 0.39 m/yr at kilometer 470 by year 600. Likely as a result, freezing near the ice front drops slightly, from 0.29 m/yr to 0.24 m/yr. Meanwhile, melt-

Time (years)	Max $\psi$ ( $\text{m}^2\text{s}^{-1}$ )	Max $ v $ ( $\text{cm} \cdot \text{s}^{-1}$ )
10	3.820	6.86
100	3.755	6.34
200	3.666	6.09
300	3.616	5.95
600	3.610	5.81

Table 2: Slowing of ocean circulation

ing increases strongly near the grounding line, rising by as much as 1.29 m/yr at kilometer 570 to reach a maximum of 2.17 m/yr by the end of the simulation. This result is affected by the no-normal-flow boundary condition imposed on the ocean at the grounding line, which reduces horizontal velocity in the mixed layer under the shelf, thus decreasing the turbulent exchange velocities, and in turn the melt rate.

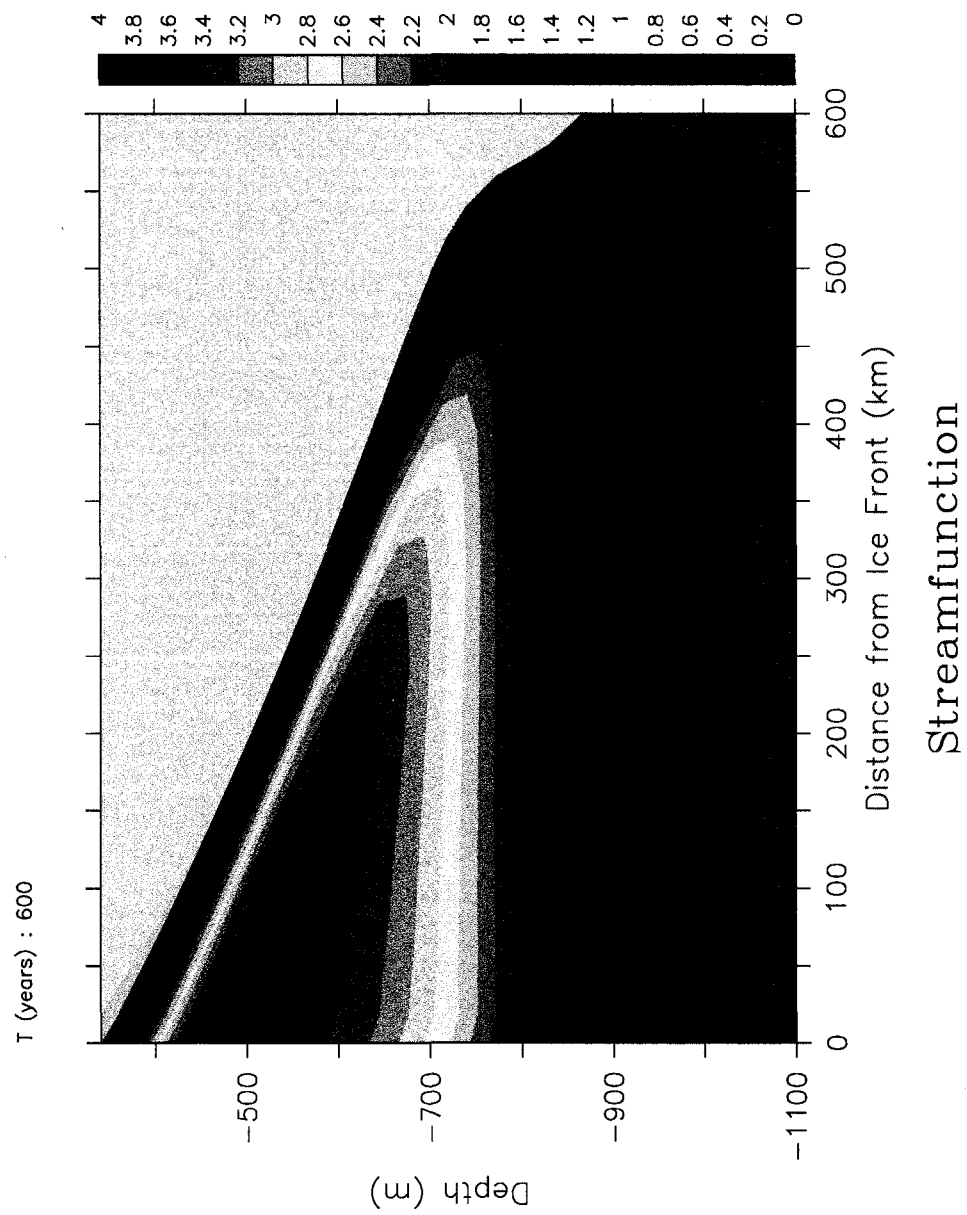
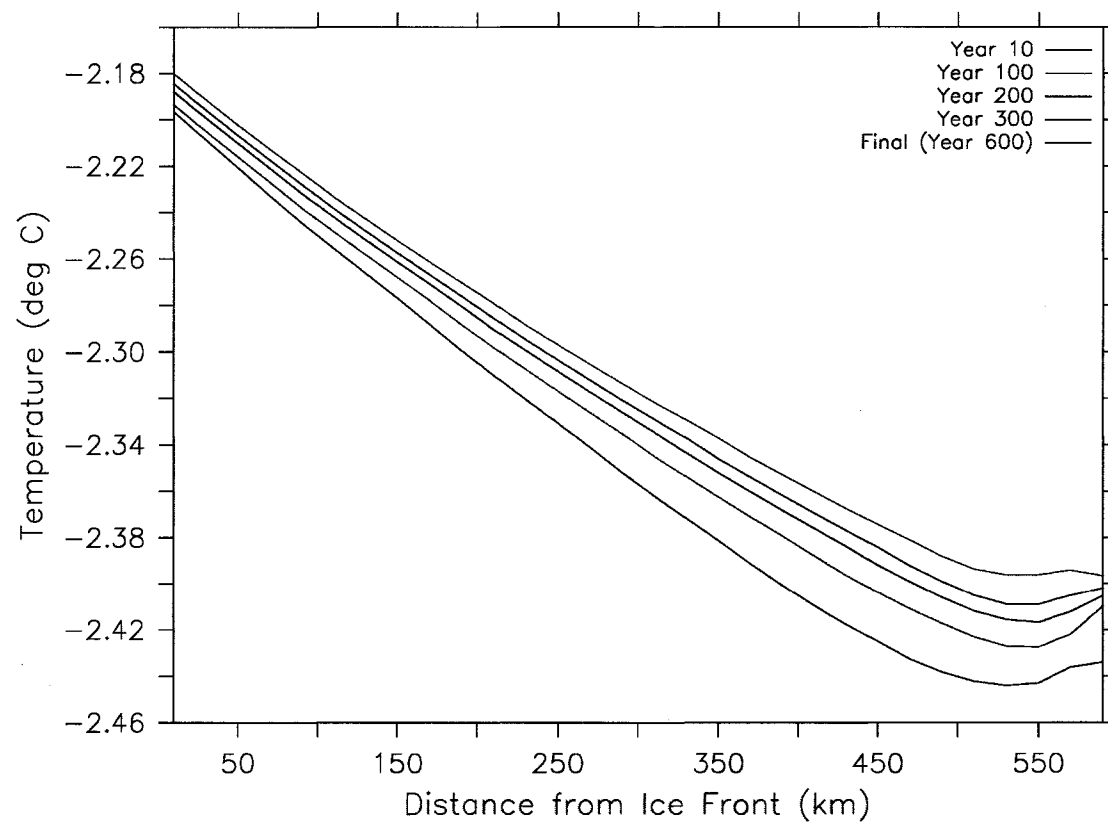


Figure 8: Vertical overturning streamfunction ( $\text{m}^2 \cdot \text{s}^{-1}$ ) after 600 years.



Freezing Point at Interface

Figure 9: Warming of interface freezing point

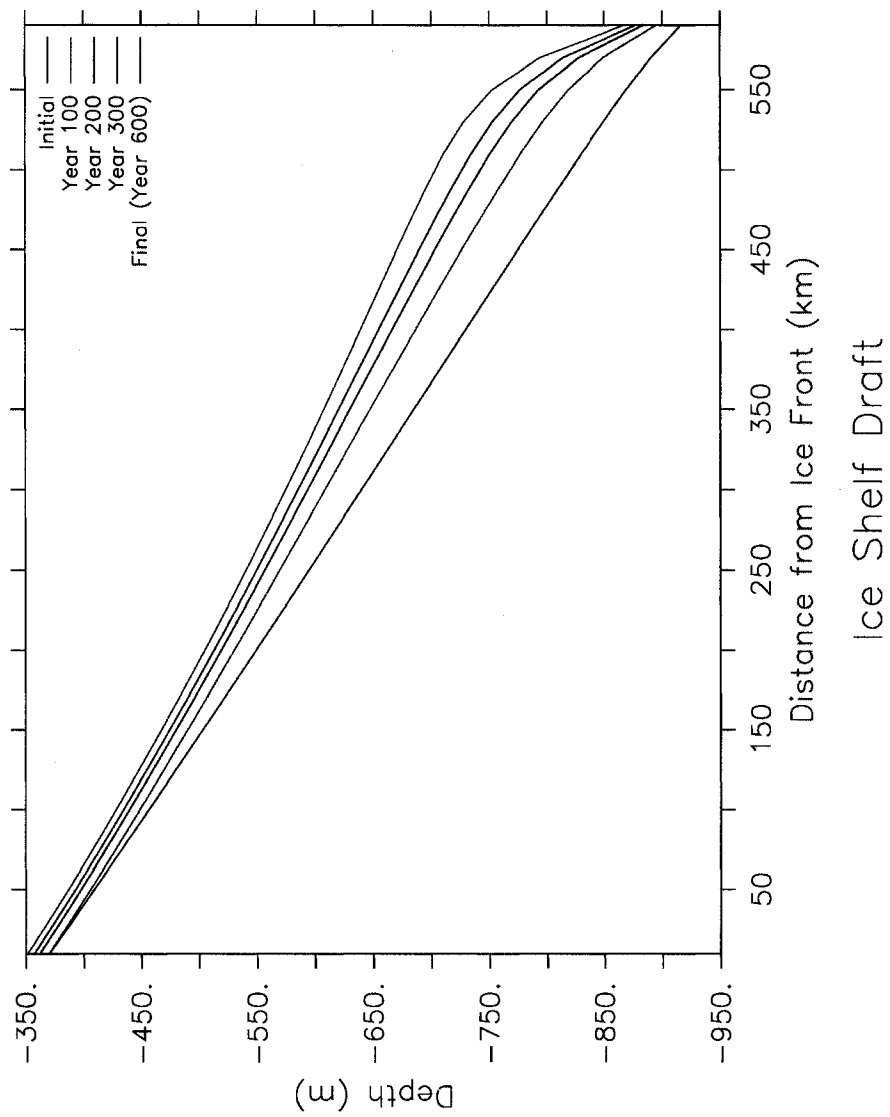
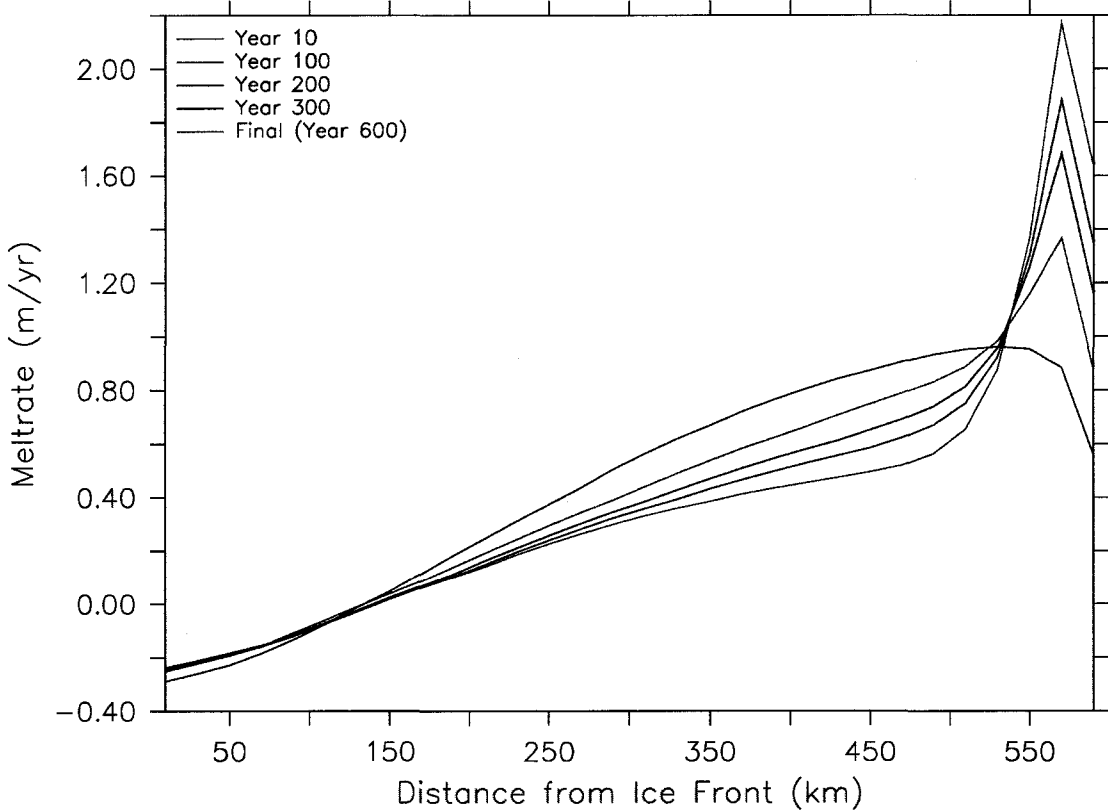


Figure 10: Evolution of ice shelf draft



Meltrate

Figure 11: Evolution of melt rate

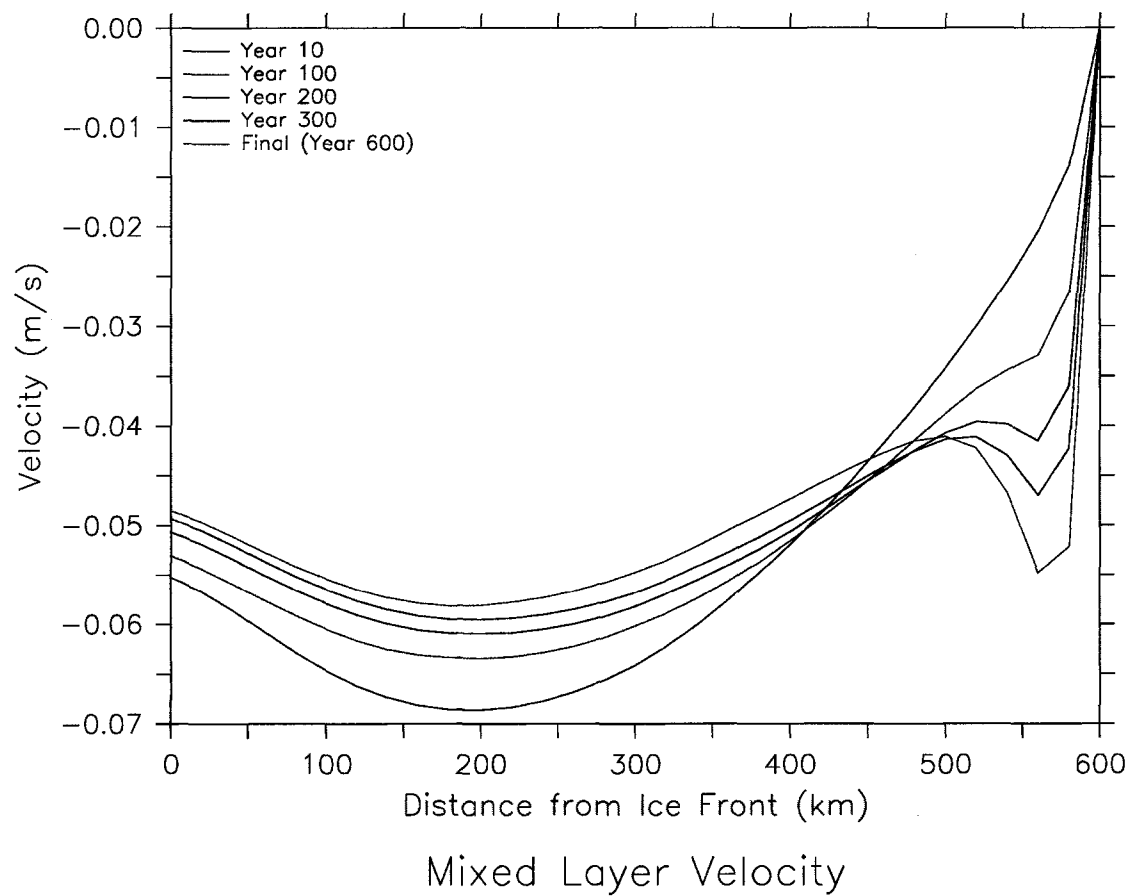


Figure 12: Evolution of mixed-layer velocity

### 4.2.3 Final state of ice shelf

Over the course of the simulation, the ice shelf comes into a new equilibrium, with advection of meteoric ice balanced against ocean-driven melting and freezing at its base. In the process, 10.3% of the initial mass of the shelf is lost. The majority of this loss comes early in the simulation, with 4.5% of the initial mass lost in the first 100 years, and a total of 6.9% lost in the first 200 years. Marine ice thickness peaks at 20.5 m just inside the ice front, with the majority forming within the first 200 years (Figure 13). Significant changes to the basal slope also occur. The initial shelf profile was close to the linear profile with slope  $1 \times 10^{-3}$  used in [15], with a slope varying between  $9 \times 10^{-4}$  and  $1.3 \times 10^{-3}$ . The final profile flattens throughout the majority of the domain, with slopes as low as  $6.3 \times 10^{-4}$ , but steepens sharply near the grounding line, reaching a peak slope of  $3.6 \times 10^{-3}$ . This profile is shown in Figure 14; note that the grey area near the ice front is marine ice. The consequences for shelf-ocean interaction of this change in shape have been previously discussed; however, there is also an effect on the flow of the ice shelf itself (Figure 15), since this flow is driven gravitationally by the horizontal thickness gradient. The steepening near the grounding line is outweighed by flattening in the rest of the domain, causing the velocity at the ice front to drop from 1.44 km/yr to 0.97 km/yr by the end of the simulation. This behavior is qualitatively correct according to the ice shelf model, which has a constant ice stream velocity imposed as a boundary condition; it remains to be seen whether the loss of ice shelf mass would accelerate the ice stream in a more comprehensive model or in nature.



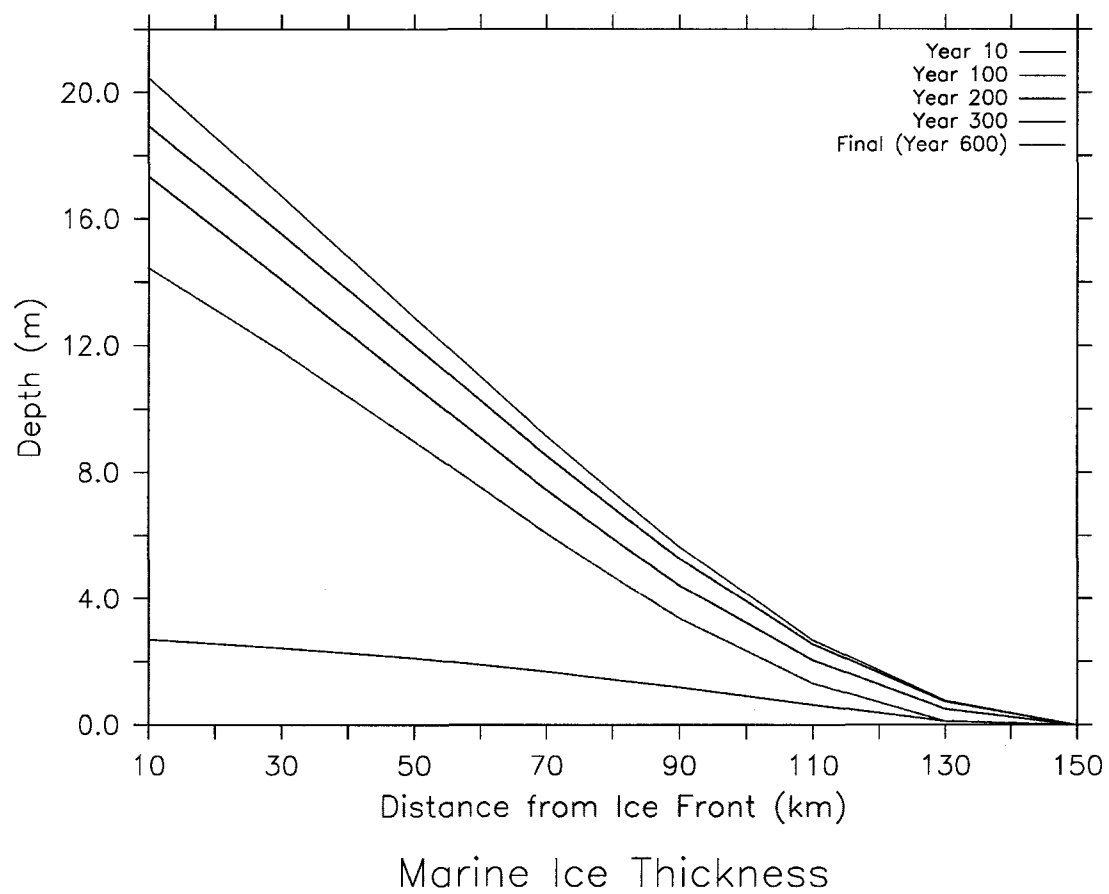
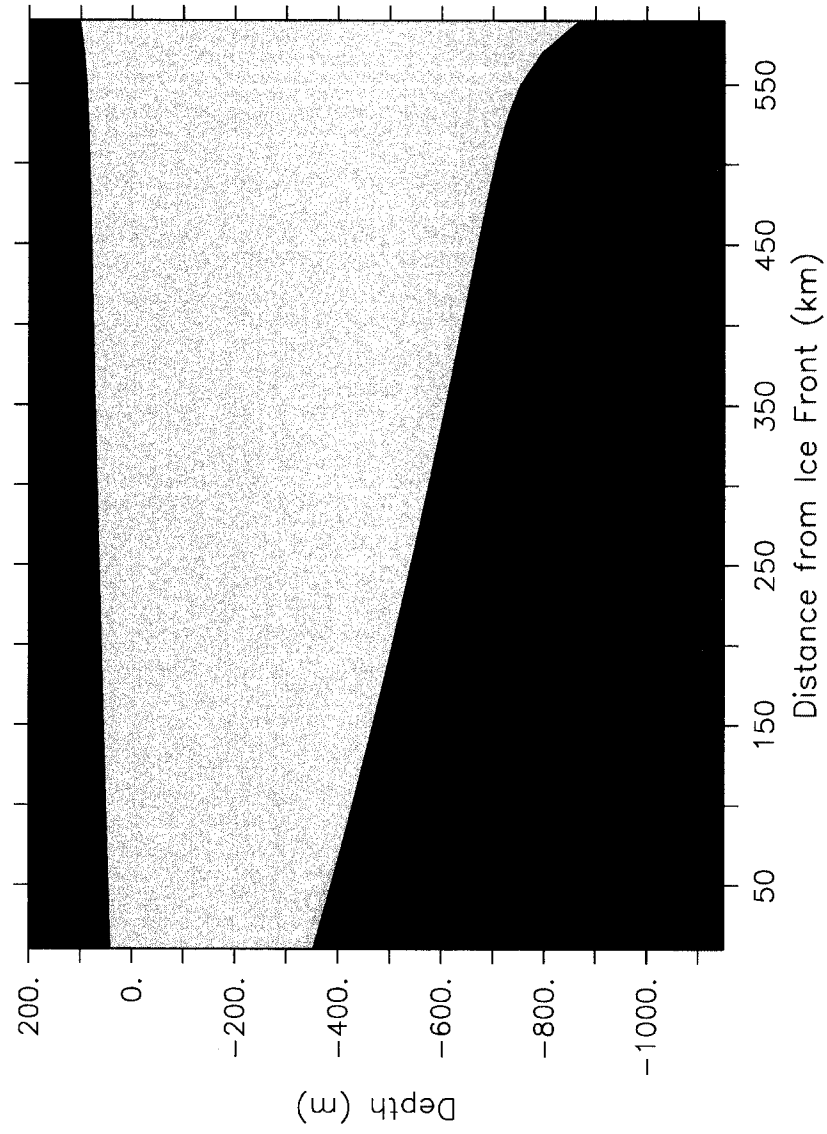


Figure 13: Formation of marine ice



Ice Shelf Profile

Figure 14: Ice shelf profile at end of simulation

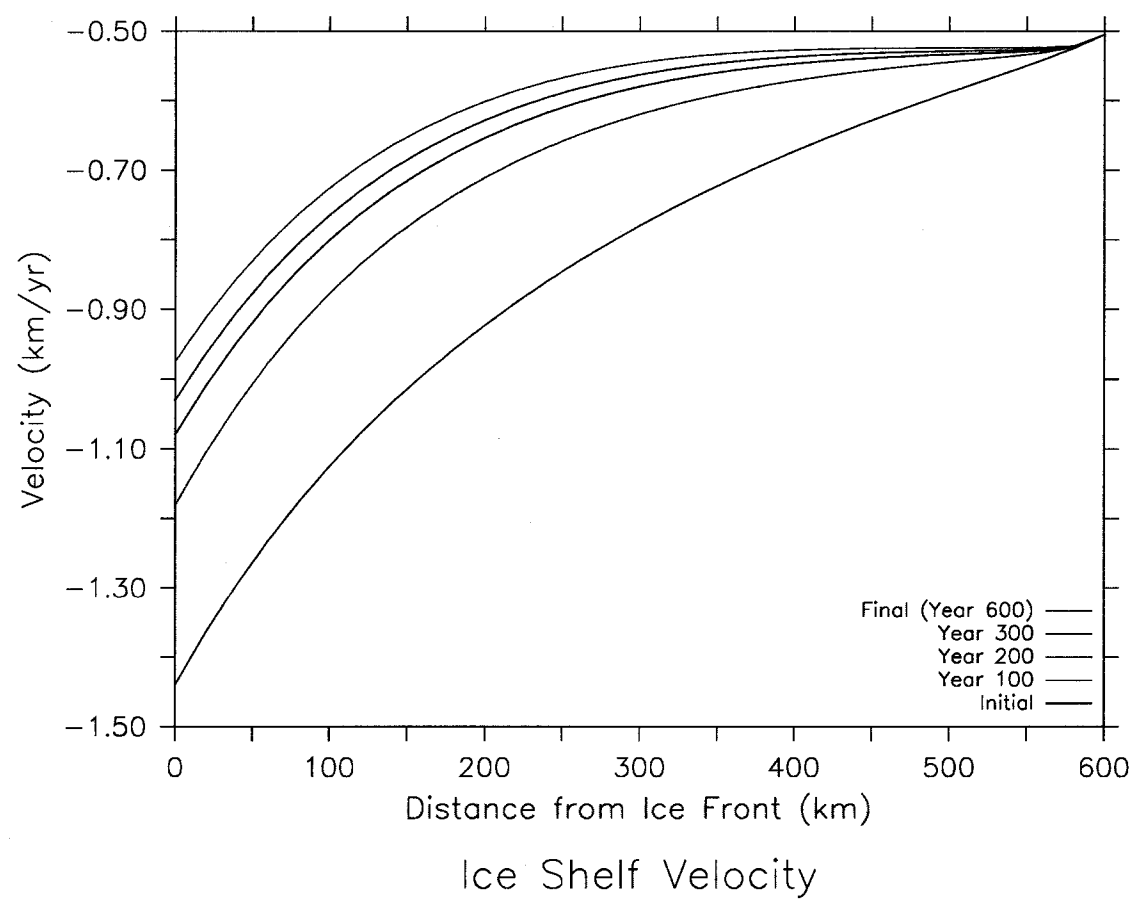


Figure 15: Evolution of ice shelf velocity

Parameter	Max $\psi$ ( $\text{m}^2\text{s}^{-1}$ )	Max $ v $ ( $\text{cm} \cdot \text{s}^{-1}$ )
$\nu_v = 1 \times 10^{-3}$	6.348	13.55
$\nu_v = 3 \times 10^{-3}$	2.921	4.62
$\kappa_v = 5 \times 10^{-5}$	3.090	6.71
$\kappa_v = 2 \times 10^{-4}$	4.844	6.89

Table 3: Uncertainty in ocean circulation (after 10 years) due to variation of parameters

### 4.3 Sensitivities

#### 4.3.1 Uncertainties in physical parameters

Of the physical parameters affecting the behavior of the model, the two most important are the vertical viscosity  $\nu_v$  and the vertical diffusivity  $\kappa_v$ . Unfortunately, due to a lack of velocity measurements for sub-ice shelf meltwater plumes, the proper values of these parameters remain uncertain. In this study, values consistent with most previous estimates have been used, but it remains necessary to examine the effects of varying these values. The results of doing so are summarized in Tables 3 and 4. Comparisons are made after ten years of integration since the ocean tends to reach an initial nearly steady state by this time (Section 4.2.1), and the overall circulation changes relatively little thereafter (Section 4.2.2).

The vertical viscosities considered here lie at the high end of the usual range; this is necessary due to the indirect manner in which the no-slip boundary condition at the shelf base is implemented (Section 3.1.6). Since the vertical diffusivity measures the strength of vertical mixing, we find that increasing  $\kappa_v$  produces stronger overturning circulation, as should be expected. The effects summarized

Parameter	Avg melt (m/yr)	Max melt (m/yr)	Min melt (m/yr)
$\nu_v = 1 \times 10^{-3}$	0.72	1.68	-0.62
$\nu_v = 3 \times 10^{-3}$	0.34	0.71	-0.18
$\kappa_v = 5 \times 10^{-5}$	0.36	0.86	-0.32
$\kappa_v = 2 \times 10^{-4}$	0.55	1.11	-0.24

Table 4: Uncertainty in basal melting (after 10 years) due to variation of parameters

in Table 4 result from the use of velocity-dependent turbulent exchange coefficients, which increase both melting and freezing when the ocean circulation intensifies.

#### 4.3.2 Variation of potential temperature

In order to investigate scenarios involving climate change (or even seasonal variation), it is necessary to examine the effects of perturbing the potential density profile imposed at the ice front. (All other model parameters remain as in Table 1.) The results are summarized in Tables 5 and 6.

As would be expected, the intensity of both the ocean circulation and of the basal melting increase with temperature. The magnitude of this increase is perhaps slightly surprising, considering that the maximum plume velocity more than triples and the average melt rate increases ninefold with a temperature increase of only half a degree Celsius. A plot of the variation in basal melting (Figure 16) makes it clear that this increase is more than linear. Further observations are necessary in order to determine whether this sensitivity is physically realistic. The effects of reducing temperature are less dramatic quantitatively,

Perturbation	Max $\psi$ ( $\text{m}^2\text{s}^{-1}$ )	Max $ v $ ( $\text{cm} \cdot \text{s}^{-1}$ )
$\theta - 0.4^\circ\text{C}$	0.779	1.42
$\theta - 0.3^\circ\text{C}$	1.220	1.97
$\theta - 0.2^\circ\text{C}$	1.597	2.73
$\theta - 0.1^\circ\text{C}$	2.541	4.48
Control	3.820	6.86
$\theta + 0.1^\circ\text{C}$	5.254	9.72
$\theta + 0.2^\circ\text{C}$	6.729	12.81
$\theta + 0.3^\circ\text{C}$	8.409	16.16
$\theta + 0.4^\circ\text{C}$	10.31	19.64
$\theta + 0.5^\circ\text{C}$	12.22	22.96

Table 5: Variation in ocean circulation (after 10 years) due to temperature perturbation

Perturbation	Average melt (m/yr)	Max melt (m/yr)	Min melt (m/yr)
$\theta - 0.4^\circ\text{C}$	0.006	0.18	-0.19
$\theta - 0.3^\circ\text{C}$	0.04	0.26	-0.10
$\theta - 0.2^\circ\text{C}$	0.11	0.40	-0.08
$\theta - 0.1^\circ\text{C}$	0.23	0.65	-0.17
Control	0.43	0.96	-0.29
$\theta + 0.1^\circ\text{C}$	0.76	1.33	-0.27
$\theta + 0.2^\circ\text{C}$	1.20	1.78	-0.11
$\theta + 0.3^\circ\text{C}$	1.76	2.32	0.16
$\theta + 0.4^\circ\text{C}$	2.45	3.04	0.47
$\theta + 0.5^\circ\text{C}$	3.26	4.01	0.74

Table 6: Variation in basal melting (after 10 years) due to temperature perturbation

but produce a qualitatively different circulation regime (Figure 17). With less melting, the ISW plume is weaker, and tends to separate from the ice shelf base before exiting the cavity at the ice front. When this occurs, water near the surface is drawn into the cavity, cools through contact with the shelf, increases in salinity due to brine rejection from basal freezing, and sinks before exiting the cavity just above the ISW plume. The weakened circulation reduces the thermal exchange velocity, resulting in less basal freezing than would be expected due to the colder temperatures. Because this circulation depends strongly on local salinity fluxes near the ice front, it is less stable than patterns which are dominated by a strong plume, and may well be subject to seasonal temperature cycles, which will be investigated in future experiments.

#### **4.3.3 Sloping ocean floor**

To investigate the effects of bathymetry, the domain is modified so that the ocean floor slopes downwards (with a constant slope of  $5 \times 10^{-4}$ ) from the original depth of 1100 m at the ice front to a new depth of 1400 m near the grounding line. The temperature and salinity profile from Station 292 is imposed at the ice front. However, in order to avoid unphysical results when extrapolating, initial conditions for all tracer points below 1100 m are set to the 1100 m values. (Note that this varies somewhat from the sloping floor experiment in [15], which reduces ocean depth at the ice front and shifts the observational data upwards.) The resulting flow after ten years is shown in Figure 18. As might be expected, the circulation intensifies when the inflowing HSSW is given a slope to descend

(Figure 19). The maximum streamfunction value is  $5.487 \text{ m}^2\text{s}^{-1}$ , with a corresponding maximum horizontal velocity of  $10.2 \text{ cm} \cdot \text{s}^{-1}$ . The average melt rate increases to  $0.66 \text{ m/yr}$ , with maximum melting of  $2.32 \text{ m/yr}$  and maximum freezing of  $0.47 \text{ m/yr}$ . Bathymetry will be further investigated in future experiments simulating particular ice shelves (such as Pine Island) which are known to have irregularly shaped cavities.

#### **4.3.4 Increased ice shelf velocity**

Changes to any of the parameters governing the flow of the ice shelf affect the final equilibrium, and thus their impact can only be investigated by making a full model run. Since surges in the flow of ice streams are a possible consequence of a warming climate, we consider an experiment in which the ice stream velocity is increased to  $1 \text{ km/yr}$ . In order to isolate the effects of interaction with the ocean, the initial configuration of the shelf is determined by running the ice shelf component to steady state (as in Section 4.1). This initial profile is shown in Figure 20. The model is run until the shelf reaches equilibrium, which is considered to have occurred after the total ice mass changes by only  $0.3\%$  between years 200 and 250, with thickness changing by no more than  $0.4\%$  at any point during that time. (Since equilibrium between ocean and ice shelf occurs at the slower ice shelf timescale, it is reasonable to expect that the time to equilibrium would be approximately halved when the shelf velocity is doubled.) Overall ocean circulation varies very little from the control experiment, so we will focus on the evolution of the ice shelf as shown in Figure 21. A total of  $5.0\%$  of the original



ice mass is lost during this experiment, with 2.2% lost in the first 50 years and a total of 3.5% lost after 100 years. Perhaps due to the greater ice shelf draft near the front (400 m versus 370 m), less marine ice is formed than in the control experiment (7.2 m versus 20.5 m). The initial shelf profile is convex, with a minimum slope of  $4.7 \times 10^{-4}$  near the grounding line and a maximum slope of  $9.8 \times 10^{-4}$  near the ice front. Within the first 50 years of simulation, this profile reverses concavity. By the end of the experiment, the maximum basal slope is  $1.5 \times 10^{-3}$ , which occurs near the grounding line, with flatter slopes between  $7.9 \times 10^{-4}$  and  $9.0 \times 10^{-4}$  nearer the ice front. The final ice shelf profile is shown in Figure 22. As in the control experiment, the flattening of the base along most of the length of the shelf results in a slower flow near the ice front, with the shelf velocity dropping from its initial value of 2.38 km/yr to 1.98 km/yr by the end of the simulation. However, because the steepening near the grounding line is more dramatic than in the control experiment, the velocity in this area increases slightly (Figure 23).

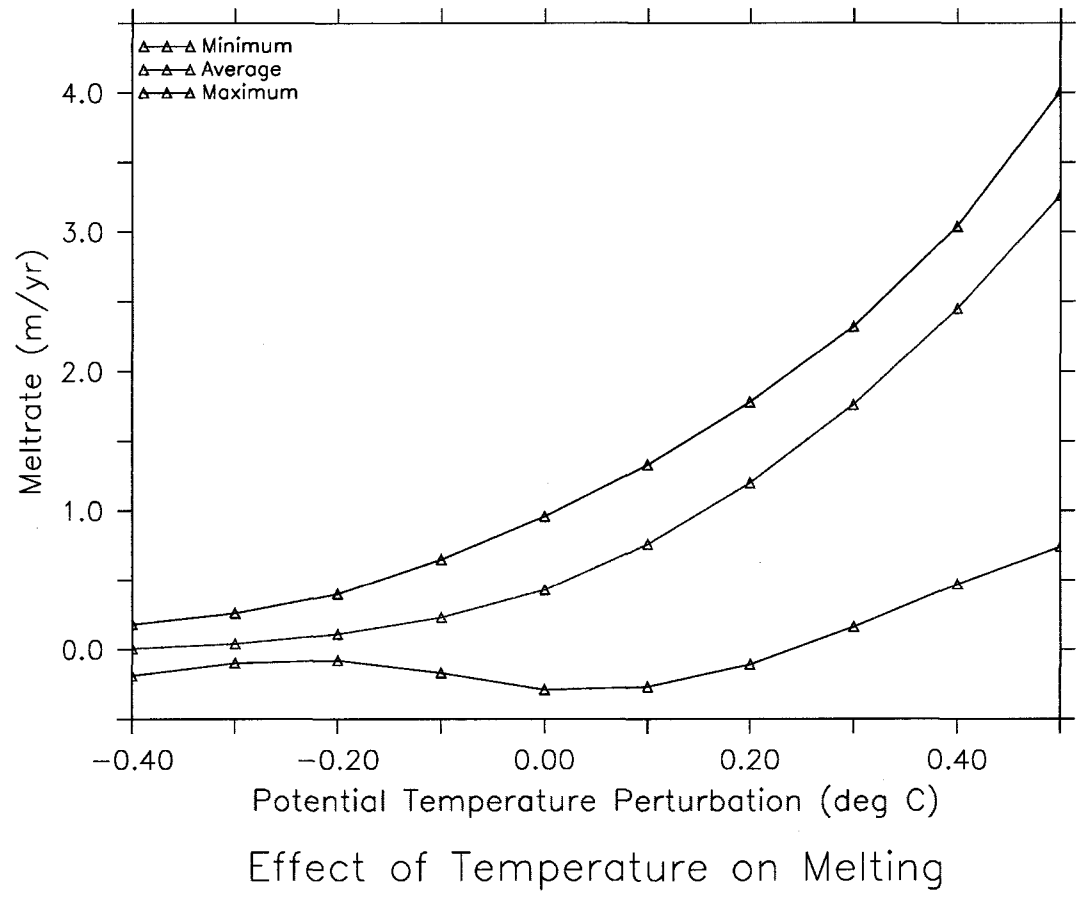


Figure 16: Variation in basal melting (after 10 years) due to temperature perturbation

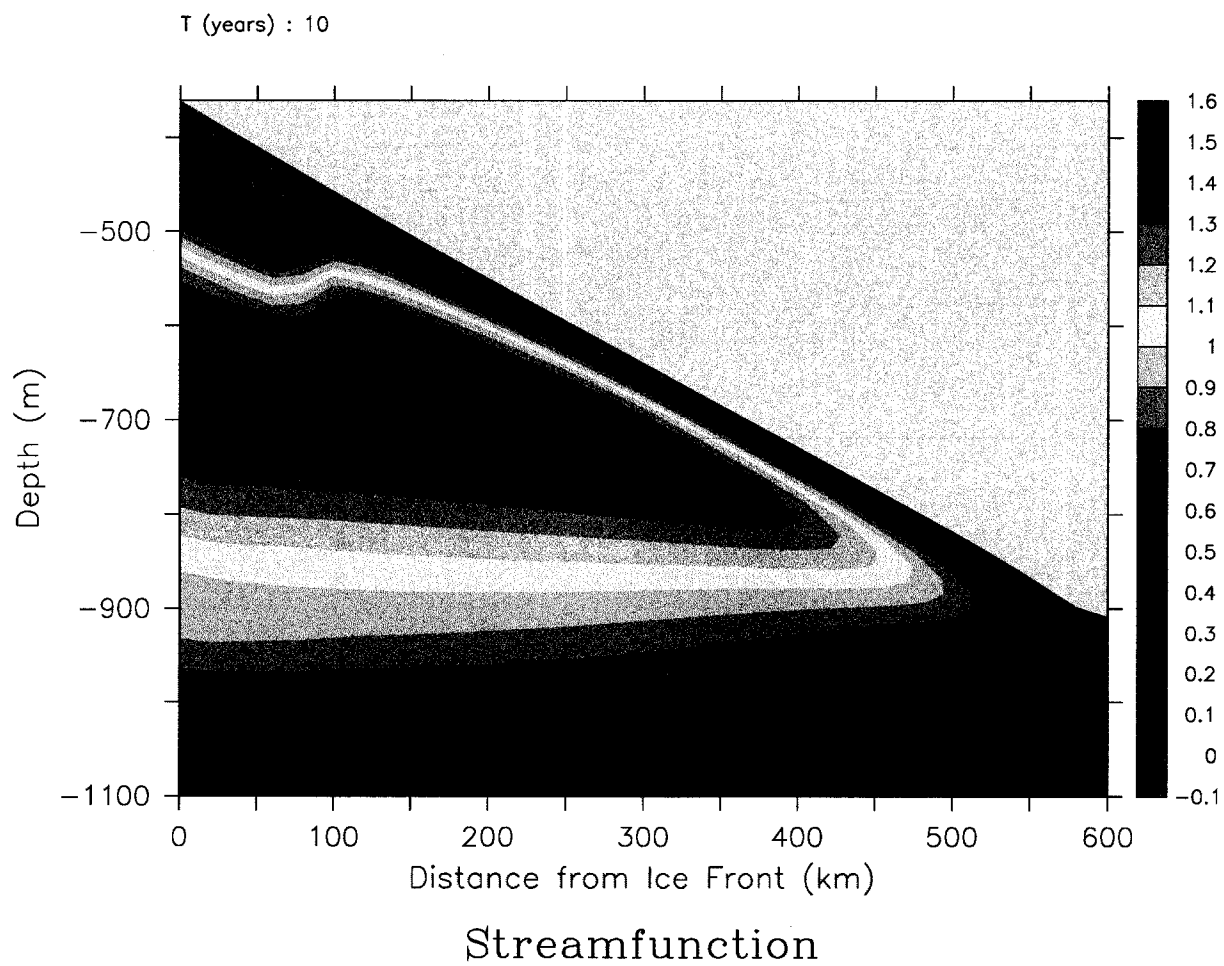


Figure 17: Streamfunction ( $\text{m}^2 \cdot \text{s}^{-1}$ ) after 10 years for  $-0.2^\circ\text{C}$  temperature perturbation

97

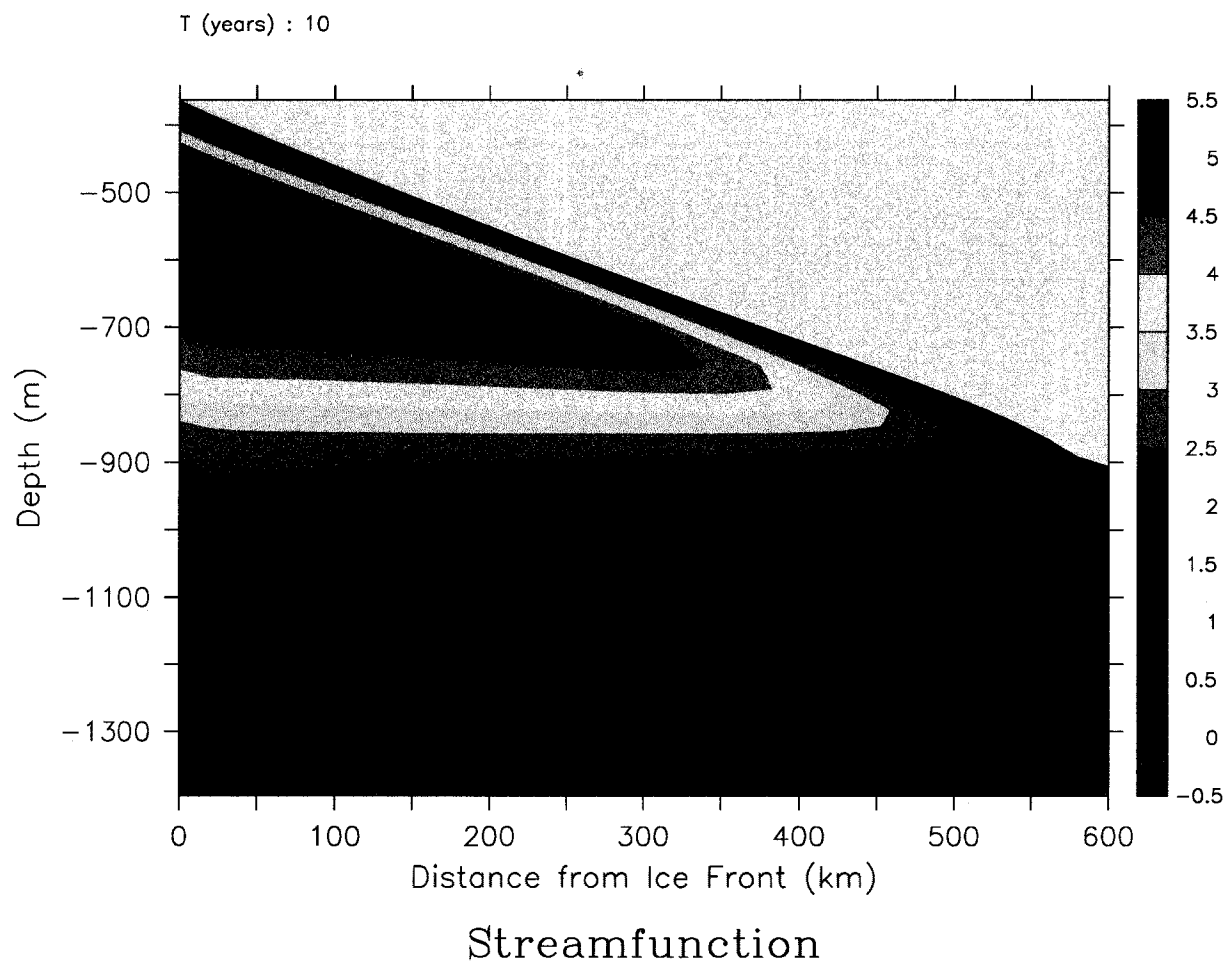


Figure 18: Streamfunction ( $\text{m}^2 \cdot \text{s}^{-1}$ ) after 10 years for sloping ocean floor

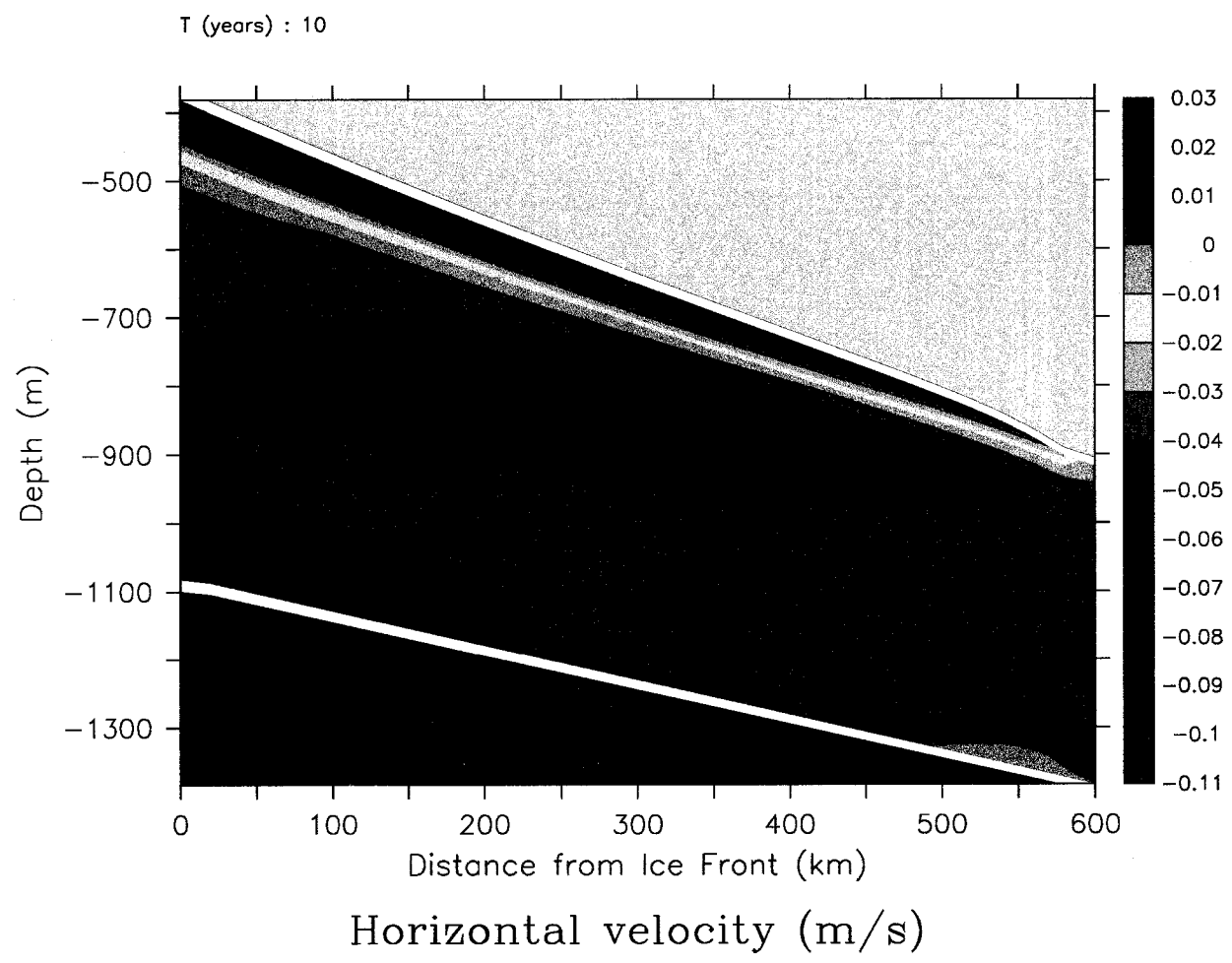


Figure 19: Horizontal velocity ( $\text{m} \cdot \text{s}^{-1}$ ) after 10 years for sloping ocean floor

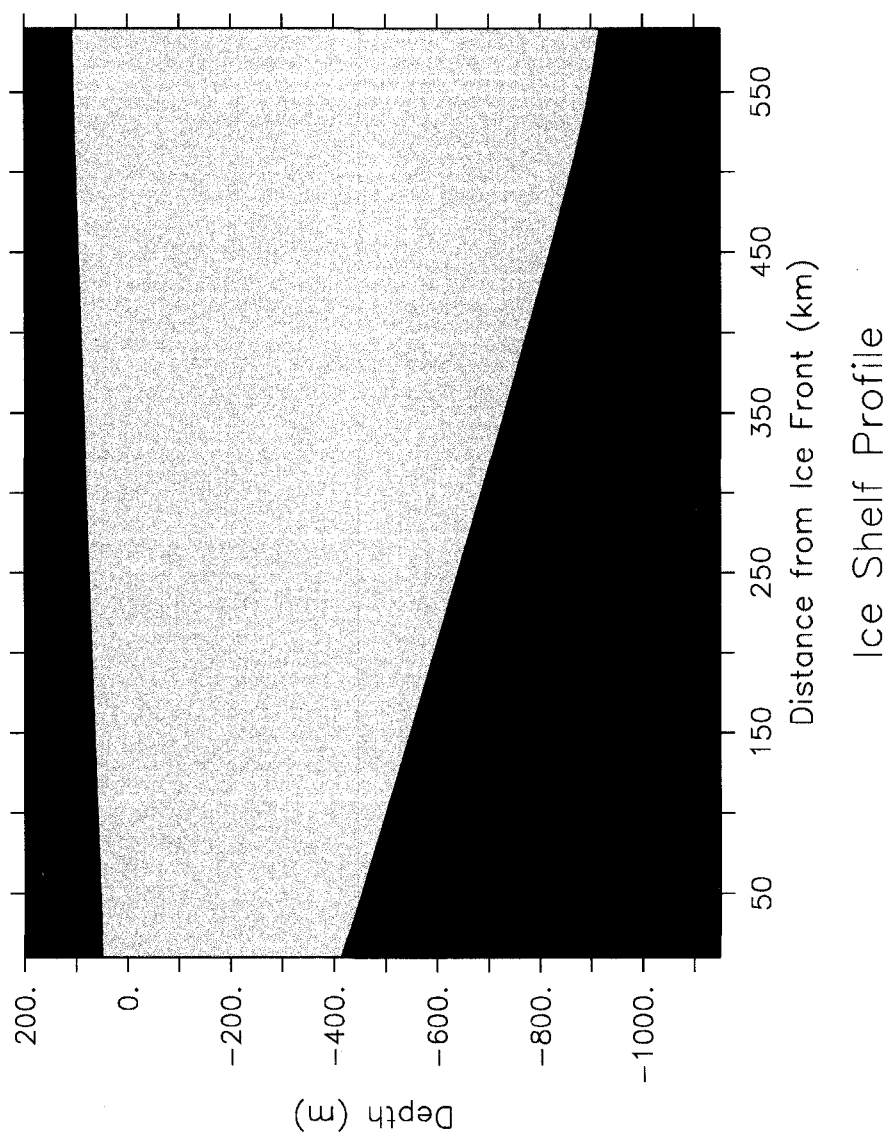


Figure 20: Initial ice shelf profile for faster ice stream

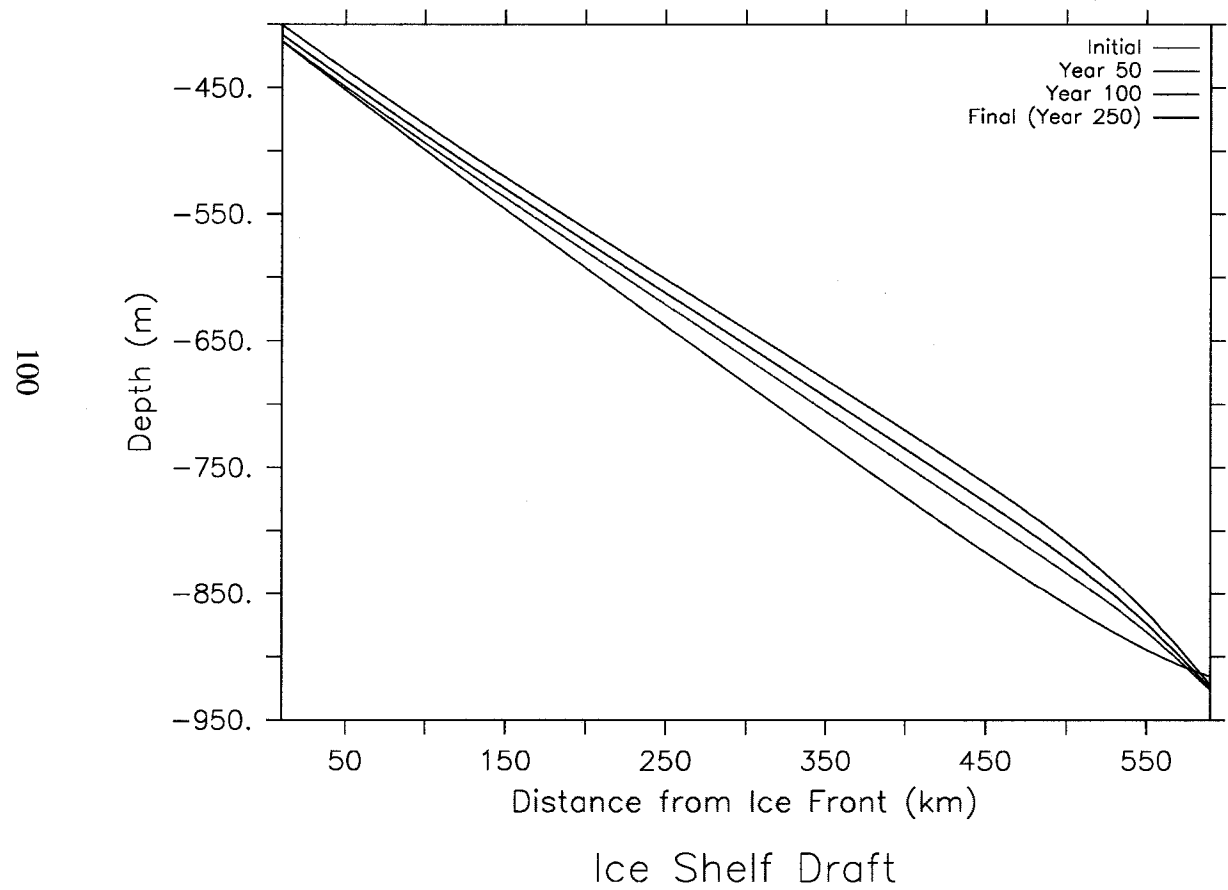


Figure 21: Evolution of ice shelf draft for faster ice stream

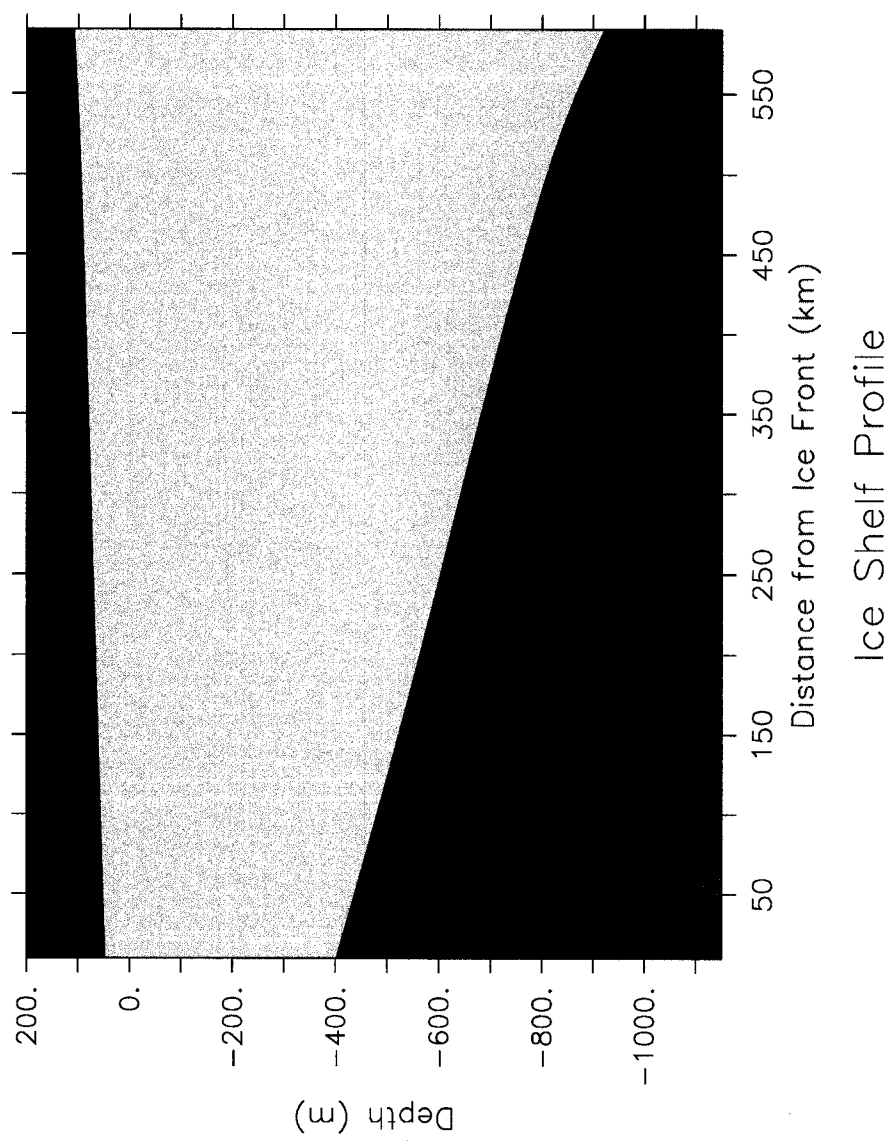


Figure 22: Final ice shelf profile for faster ice stream



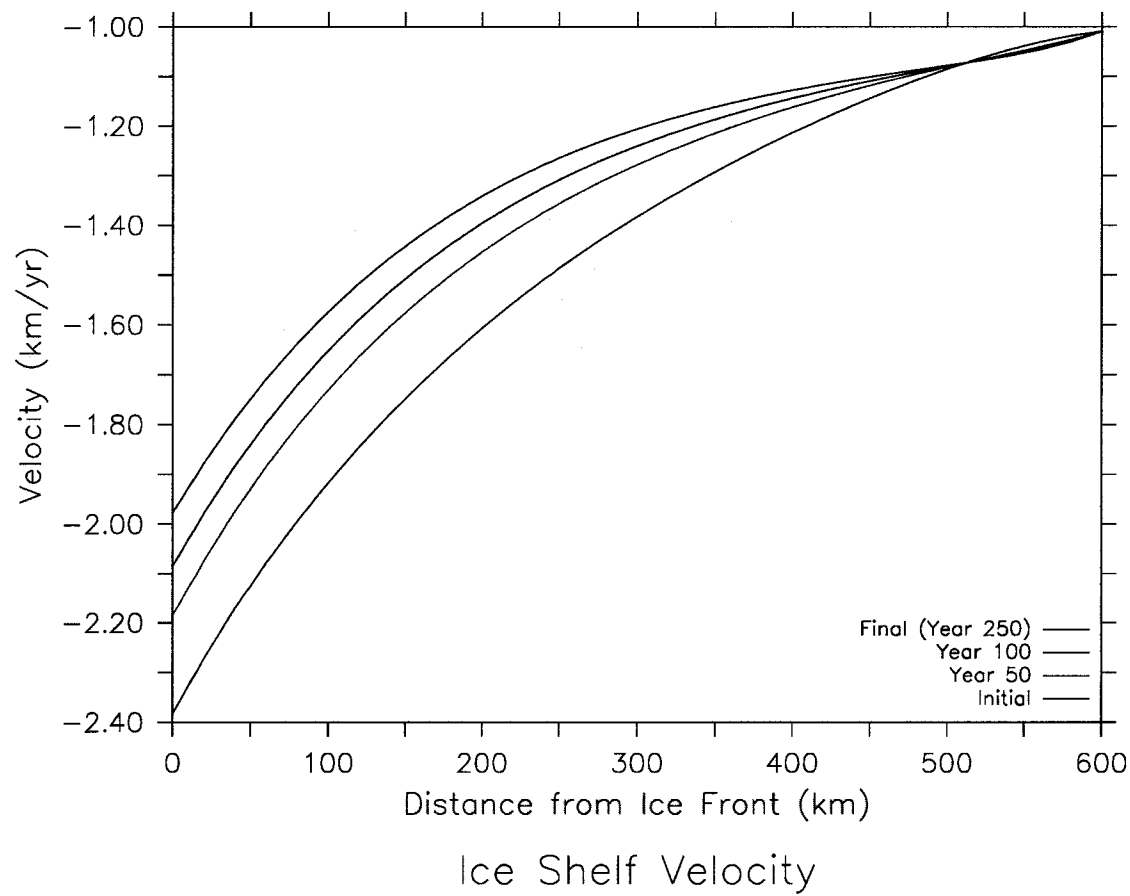


Figure 23: Evolution of ice shelf velocity for faster ice stream

## 5 Conclusions

The goal of this study has been the creation of a simplified model of ice shelf-ocean interaction suitable for investigating the equilibrium between a dynamic-thermodynamic ice shelf and the underlying ocean. This new model is distinct from earlier reduced models in its inclusion of ice shelf dynamics, and from full three-dimensional models in its simplicity and computational efficiency. The relative simplicity of the model physics and numerics allows for easier understanding of the physical processes at work in ice shelf-ocean interaction, while the efficiency of the model permits extensive sensitivity studies of this system.

The initial results produced by this model suggest that interaction with the ocean significantly affects the equilibrium mass balance and morphology of an ice shelf. For a relatively cold temperature regime ( $\theta \approx -1.9^\circ\text{C}$ ), slightly more than 10% of the ice mass is lost relative to the steady state of the ice shelf when ocean interaction is not considered. Large increases in basal slope near the grounding line are observed, accompanied by shifts in mixed layer velocity and basal melting as the ocean adjusts to the changing ice shelf profile. Sensitivity studies indicate that both basal melting and ocean circulation intensify considerably when ocean temperature is increased by  $0.5^\circ\text{C}$ , suggesting that these effects could be much stronger for ice shelves exposed to relatively warm water masses. Uncertainties in several physical parameters due to lack of observational data suggest that the quantitative results of this study should not be considered exact. However, the qualitative behavior of the model is unaffected by these uncertainties, indicating that the relevant physics is accurately simulated and that

the results thus provide some insight as to the processes at work in the ice shelf-ocean system.

These results, which show little variation in the pattern of overall ocean circulation over the course of the simulation, imply that the meltwater plume is the most important part of the domain for long-term studies of ice shelf evolution. Plume models, especially those which are (horizontally) two-dimensional, thus appear to show promise as the ocean component of reduced coupled models. However, since these models do not explicitly simulate the underlying ocean, entrainment of HSSW into the plume must be parameterized as a function of plume velocity [23], producing some uncertainty in the results. It is not clear, given the sparsity of observations, whether plume models are more or less accurate than vertical overturning models (such as the current model), which simulate the entire ocean but are themselves subject to some uncertainty in vertical mixing. The best reduced ocean model for use in studies of ice shelf-ocean interaction is the simplest model which can accurately simulate the ISW plume; which model this is remains an open question until further observations become available.

The relatively small variation in ocean circulation throughout the control experiment, along with the large difference in timescales between the ocean and ice shelf, suggests that future reduced coupled models would do well to adopt an asynchronous coupling strategy. The ocean component of this model tends to reach a nearly steady state in five to ten years, and to move away from this state only after significant change to the ice shelf profile occurs on a timescale of decades. It would appear that the efficiency of the present model could be im-

proved by running the ocean to steady state with a fixed ice shelf, then holding the basal melting constant while running the ice shelf for a much longer time. The ocean would then be re-interpolated based on the new shelf profile, and the process continued. This strategy was not adopted for the current model out of the desire to avoid making assumptions about the relevant timescales, since the efficiency of this model made a synchronous approach computationally feasible.

Besides asynchronous modeling, several future studies extending the current model are possible. Fresh water fluxes at the grounding line from streams flowing beneath the ice shelf are believed to enhance basal melting, and could easily be simulated with a minor modification to the boundary conditions. Another relatively straightforward modification would add time-dependent temperature and salinity profiles at the ice front, allowing simulation of seasonal variation and gradual climate change. Incorporating frazil ice into the ocean model would likely improve its predictions of marine ice formation, which is important in determining the equilibrium profile of ice shelves like the Amery [17], although this represents a more significant modification.

Application of this model to other ice shelves, particularly those undergoing strong basal melting, is also a major goal for future studies. Pine Island Glacier, which is estimated to melt in excess of 25 m/yr near the grounding line [14], presents a particular challenge. The steep basal slope, which may be an order of magnitude greater than that of the Filchner Ice Shelf, will require finer spatial resolution in order to avoid problems with hydrostatic inconsistency in calculating the horizontal density gradient (Section 3.1.3). Since the high melting is

likely to drive a particularly strong overturning circulation, a reduced time step may also be necessary to maintain stability, making for a much more expensive simulation than the control experiment. However, since the ice stream velocity is approximately 2.5 km/yr, and the shelf is only 80 km long, the results of Section 4.3.4 suggest that equilibrium should be reached relatively quickly, so the experiment should be feasible. This application is a high priority, since Pine Island glacier represents an important case study for climate change, presenting conditions under which a coupled ice shelf-ocean model would potentially be most useful.

## References

- [1] Arakawa, A., and V.R. Lamb, 1977: Computational design of the basic dynamical processes of the UCLA general circulation model. *Methods in Computational Physics*, **17**, 173-265.
- [2] Cox, M.D., 1984: A primitive equation, 3-dimensional model of the ocean. GFDL Ocean Group Technical Report No. 1.
- [3] Determann, J., and R. Gerdes, 1994: Melting and freezing beneath ice shelves: implications from a three-dimensional ocean-circulation model. *Ann. Glaciol.*, **20**, 413-419.
- [4] Durran, D.R., 1994: *Numerical Methods for Wave Equations in Geophysical Fluid Dynamics*. Springer-Verlag, New York, USA.
- [5] Durran, D.R., 1991: The third-order Adams-Bashforth method: An attractive alternative to leapfrog time differencing. *Mon. Wea. Rev.*, **119**, 702-720.
- [6] Eicken, H., H. Oerter, H. Miller, W. Graf, and J. Kipfstuhl, 1994: Textural characteristics and impurity content of meteoric and marine ice in the Ronne Ice Shelf, Antarctica. *J. Glaciol.*, **40**, 386-398.
- [7] Foldvik, A., T. Gammelsrød, S. Østerhus, E. Fahrbach, G. Rohardt, M. Schröder, K.W. Nicholls, L. Padman, and R.A. Woodgate, 2004: Ice shelf water overflow and bottom water formation in the southern Weddell Sea. *J. Geophys. Res.*, **109**, C02015, doi:10.1029/2003JC002008.

- [8] Foldvik, A., and T. Kvinge, 1974: Conditional instability of sea water at the freezing point. *Deep Sea Research*, **21**(3), 169-174.
- [9] Foldvik, A., and T. Kvinge, 1977: Thermohaline convection in the vicinity of an ice shelf. *Polar Oceans: Proceedings of the Polar Oceans Conference held at McGill University, Montreal, 1974*. Arctic Institute of North America, Calgary, Canada.
- [10] Fricker, H.A., S. Popov, I. Allison, and N. Young, 2001: Distribution of marine ice beneath the Amery Ice Shelf. *Geophys. Res. Lett.*, **28**(11), 2241-2244.
- [11] Grosfeld, K., H. Sandhager, and M.A. Lange, 2003: Ice shelf regions under climate change: Studies with a coupled ice shelf-ocean model approach. *CLIVAR Exchanges* 28.
- [12] Grosfeld, K., R. Gerdes, and J. Determann, 1997: Thermohaline circulation and interaction between ice shelf cavities and the adjacent open ocean. *J. Geophys. Res.*, 102, 15595-15610.
- [13] Haney, R.L., 1991: On the pressure gradient force over steep topography in sigma coordinate ocean models. *J. Phys. Oceanogr.*, **21**, 610-619.
- [14] Hellmer, H.H., S.S. Jacobs, and A. Jenkins, 1998: Ocean erosion of a floating Antarctic glacier in the Amundsen Sea. *Ocean, Ice, and Atmosphere: Interactions at the Antarctic Continental Margin*, *Antarct. Res. Ser.*, **75**, 83-99.

- [15] Hellmer, H.H., and D.J. Olbers, 1989: A two-dimensional model for the thermohaline circulation under an ice shelf. *Antarct. Sci.*, **1**(4), 325-336.
- [16] Hellmer, H.H., and D.J. Olbers, 1991: On the thermohaline circulation beneath the Filchner-Ronne Ice Shelves. *Antarct. Sci.*, **3**(4), 433-442.
- [17] Hellmer, H.H., and S.S. Jacobs, 1992: Ocean interactions with the base of Amery Ice Shelf, Antarctica. *J. Geophys. Res.*, **97**(C12), 20305-20317.
- [18] Hellmer, H.H., and S.S. Jacobs, 1995: Seasonal circulation under the eastern Ross Ice Shelf, Antarctica. *J. Geophys. Res.*, **100**(C6), 10873-10885.
- [19] Holland, D.M., 2002: Computing marine-ice thickness at an ice-shelf base. *J. Glaciol.*, **48**(160), 9-19.
- [20] Holland, D.M., S.S. Jacobs, and A. Jenkins, 2003: Modelling the ocean circulation beneath the Ross Ice Shelf. *Antarct. Sci.*, **15**(1), 13-23.
- [21] Holland, D.M., and A. Jenkins, 1999: Modeling thermodynamic ice-ocean interactions at the base of an ice shelf. *J. Phys. Oceanogr.*, **29**, 1787-1800.
- [22] Holland, D.M., and A. Jenkins, 2001: Adaptation of an isopycnic coordinate ocean model for the study of circulation beneath ice shelves. *Mon. Wea. Rev.*, **129**(8), 1905-1927.
- [23] Jenkins, A., 1991: A one-dimensional model of ice shelf-ocean interaction. *J. Geophys. Res.*, **96**(C11), 20671-20677.



- [24] Jenkins, A., and A. Bombosch, 1995: Modeling the effects of frazil ice crystals on the dynamics and thermodynamics of Ice Shelf Water plumes. *J. Geophys. Res.*, **100**, 6967-6981.
- [25] Jenkins, A., H.H. Hellmer, and D.M. Holland, 2001: The role of meltwater advection in the formulation of conservative boundary conditions at an ice-ocean interface. *J. Phys. Oceanogr.*, **31**, 285-296.
- [26] Lewis, E.L., and R.G. Perkin, 1986: Ice pumps and their rates. *J. Geophys. Res.*, **91**(C10), 11756-11762.
- [27] MacAyeal, D.R., 1984: Numerical simulations of the Ross Sea Tides. *J. Geophys. Res.*, **89**, 607-615.
- [28] MacAyeal, D.R., 1984: Thermohaline circulation below the Ross Ice Shelf: a consequence of tidally induced vertical mixing and basal melting. *J. Geophys. Res.*, **89**, 597-606.
- [29] MacAyeal, D.R., 1985: Tidal rectification below the Ross Ice Shelf, Antarctica. *Oceanology of the Antarctic Continental Shelf, Antarct. Res. Ser.*, **43**, 109-132.
- [30] McDougall, T.J., D.R. Jackett, D.G. Wright, and R. Feistel, 2003: Accurate and computationally efficient algorithms for potential temperature and density of seawater. *J. Atmos. Oceanic Technol.*, **20**, 730-740.
- [31] Mellor, G.L., 2004: User's guide for a three-dimensional, primitive equation, numerical ocean model.

- [32] Mellor, G.L., and A.F. Blumberg, 1985: Modeling vertical and horizontal diffusivities with the sigma coordinate system. *Mon. Wea. Rev.*, **113**, 1379-1383.
- [33] Mellor, G.L., T. Ezer, and L.-Y. Oey, 1994: The pressure gradient conundrum of sigma coordinate ocean models. *J. Atmos. Oceanic Technol.*, **11**, 1126-1134.
- [34] Millero, F.J., 1978: Annex 6: Freezing point of seawater. Eighth Report of the Joint Panel of Oceanographic Tables and Standards, UNESCO Tech. Paper Mar. Sci. 28, 29-31.
- [35] Nicholls, K.W. and K. Makinson, 1998: Ocean circulation beneath the western Ronne Ice Shelf, as derived from in situ measurements of water currents and properties. *Ocean, Ice, and Atmosphere: Interactions at the Antarctic Continental Margin, Antarct. Res. Ser.*, **75**, 301-318.
- [36] Nøst, O.A., and A. Foldvik, 1994: A model of ice shelf-ocean interaction with application to the Filchner-Ronne and Ross Ice Shelves. *J. Geophys. Res.*, **98**, 22553-22568.
- [37] Oerter, H., J. Kipfstuhl, J. Determann, H. Miller, D. Wagenbach, A. Minikin, and W. Graf, 1992: Evidence for basal marine ice in the Filchner-Ronne Ice Shelf. *Nature*, **358**, 399-401.
- [38] Orszag, S.A., and M. Israeli, 1974: Numerical simulation of viscous incompressible flows. *Annu. Rev. Fluid Mech.*, **6**, 281-318.

- [39] Pacanowski, R.C., and S.M. Griffies, 2000: MOM 3.0 Manual.
- [40] Paterson, W.S.B., 1994: *The Physics of Glaciers*. 3rd ed., Butterworth Heinemann, Oxford, UK.
- [41] Payne, A.J., P.R. Holland, A.P. Shepherd, I.C. Rutt, A. Jenkins, and I. Joughin, 2006: Numerical modelling of ocean-ice interactions under Pine Island Bay's ice shelf. Preprint?
- [42] Press, W.H., S.A. Teukolsky, W.T. Vetterling, and B.P. Flannery, 1992: *Numerical Recipes in Fortran 77 : The Art of Scientific Computing*. 2nd ed., Cambridge University Press, Cambridge, UK.
- [43] Rignot, E.J., 1998: Fast recession of a West Antarctic glacier. *Science*, **281**, 549-551.
- [44] Robin, G. de Q., 1979: Formation, flow, and disintegration of ice shelves. *J. Glaciol.*, **24**(90), 259-271.
- [45] Rohardt, G., 2002: Physical oceanography during cruise ANT-III/3 at CTD station PS06/292-2, PANGAEA, doi:10.1594/PANGAEA.67344
- [46] Sanderson, T.J.O., and C.S.M. Doake, 1979: Is vertical shear in an ice shelf negligible? *J. Glaciol.*, **22**(87), 285-292.
- [47] Scambos, T.A., J.A. Bohlander, C.A. Shuman, and P. Skvarca, 2004: Glacier acceleration and thinning after ice shelf collapse in the

Larsen B embayment, Antarctica. *Geophys. Res. Lett.*, **31**, L18402, doi:10.1029/2004GL020670.

- [48] Shchepetkin, A.F., and J.C. McWilliams, 2003: A method for computing horizontal pressure-gradient force in an ocean model with a nonaligned vertical coordinate. *J. Geophys. Res.*, **108**(C3), 3090, doi:10.1029/2001JC001047.
- [49] Smolarkiewicz, P.K., 1984: A fully multidimensional positive definite advection transport algorithm with small implicit diffusion. *J. Comput. Phys.*, **54**, 325-362.
- [50] Smolarkiewicz, P.K., and T.L. Clark, 1986: The multidimensional positive definite advection transport algorithm: further development and applications. *J. Comput. Phys.*, **67**, 396-438.
- [51] Smolarkiewicz, P.K., 1991: On forward-in-time differencing for fluids. *Mon. Wea. Rev.*, **119**, 2505-2510.
- [52] Smolarkiewicz, P.K., and L.G. Margolin, 1993: On forward-in-time differencing for fluids: Extension to a curvilinear framework. *Mon. Wea. Rev.*, **121**, 1847-1859.
- [53] Smolarkiewicz, P.K., and L.G. Margolin, 1998: MPDATA: A finite-difference solver for geophysical flows. *J. Comput. Phys.*, **140**, 459-480.

- [54] Song, Y.T., 1998: A general pressure gradient formulation for ocean models. Part I: Scheme design and diagnostic analysis. *Mon. Wea. Rev.*, **126**, 3213-3230.
- [55] Weis, M., R. Greve, and K. Hutter, 1999: Theory of shallow ice shelves. *Cont. Mech. Thermodyn.*, **11**, 15-50.
- [56] Williams, M.J.M., A. Jenkins, and J. Determann, 1998: Physical controls on ocean circulation beneath ice shelves revealed by numerical models. *Ocean, Ice, and Atmosphere: Interactions at the Antarctic Continental Margin, Antarct. Res. Ser.*, **75**, 285-299.